

Two-dimensional radiation inversion

The multichannel, multicamera bolometer system is used to perform tomographic inversions to obtain two-dimensional radiation profiles in the triangular shaped plane of W7-X. In contrast to looking at chord brightness profiles of each camera individually, tomography yields a geometrically entangled resolution of the line-integrated measurements of both systems together simultaneously. As previously elaborated on in section 2.3.2, the underlying mathematical problem is ill-posed, i.e. the number of free parameters, represented by the total number of pixels or voxels is far greater than the number of constraints, i.e. the line of sight intersections. Tomographic reconstructions are used to solve multidimensional geometric problems of inversion to find solutions for a system with such a finite number of information. Due to the nature of the measurement system and environment, the approach to this challenge is given by an iterative solution to the initial, in equation (2.32) introduced *Tikhonov regularisation* with more, to this particularly difficult problem advantageous algorithms. Let us first revisit the original posed set of equations to solve the regularised tomographic inversion problem with:

$$\begin{aligned} \tilde{\mathbf{T}}\vec{x} &= \hat{\vec{b}}, \\ \chi^2 &:= (\tilde{\mathbf{T}}\vec{x} - \hat{\vec{b}})^T (\tilde{\mathbf{T}}\vec{x} - \hat{\vec{b}}), \\ \min_{\mu} \left[\frac{1}{2} \chi^2 + \mu K \right] &\stackrel{!}{=} \min \Phi. \end{aligned} \tag{5.1}$$

→ (2D)
for later use
2D radiation
intensity distribution

Remember that $\vec{x} \in \mathbb{R}^m$ is the discretized emissivity on an established pixel grid, where $m = N_r \cdot N_\theta$ and $N_{r/\theta}$ the number of radial and poloidal intersections of that toroidal cross section, i.e. the two-dimensional radiation distribution in the triangular shaped bolometer plane. The geometry and transmission coefficients of the bolometer camera system are therefore given by the matrix $\tilde{\mathbf{T}} \in \mathbb{R}^{n \times m}$, with $n = N$ the number of absorbers or lines of sight. Finally, $\hat{\vec{b}} \in \mathbb{R}^n$ is the experimentally measured, or as shown in the previous chapter section 4.4.3 forward model integrated, chord brightness profile. In almost all cases, but particularly for this system, $\tilde{\mathbf{T}}$ is ill-conditioned and can not be simply inverted. Therefore, the minimization of the regularized problem in Φ for a given regularisation functional K and positive coupling regularisation factor μ between K and calculated solution \vec{x} is much more practical. We consider $T^{(i,j)} = \tilde{T}^{(i,j)} / \sigma^{(j)}$ and $\vec{b}^{(j)} = \hat{\vec{b}}^{(j)} / \sigma^{(j)}$ for measurement uncertainty weighting purposes of absorber j . As pointed out before, μ / K is used to impose *a priori* knowledge of the system or desired smoothness and features on solution \vec{x} . For $\mu \rightarrow 0$ the calculated radiation distribution is dominated by the characteristics of the measurement system, i.e. the LOS camera system geometry, while for $\mu \rightarrow \infty$ the opposite is the case and \vec{x} adheres to the given regularisation functional K .

A simple approach to a smoothing functional K is a second-order gradient minimizing regularisation using the finite-difference matrix expression for the Laplace¹ operator Δ .

$$\begin{aligned}
 K &= (\Delta \vec{x})^\top (\Delta \vec{x}) \\
 \mathbf{H} &= \Delta^\top \cdot \Delta \\
 \min \left[\frac{1}{2} \chi^2 + \vec{x}^\top \mathbf{H} \vec{x} \right]
 \end{aligned} \tag{5.2}$$

Minimizing this finds the (a) solution with the least curvature, i.e. the smoothest gradients, which in poloidal direction already is a good fit for the expected radiation distribution. This aspect will later play a more important role when extending the *Minimum Fisher regularisation* in section 5.1.1. One should note that equation (5.2) still has to be solved iteratively to find the best μ for a provided *best-fit* criteria for χ^2 . Such linear algorithms can and have been successfully extended and combined with many different methods, e.g. neural networks approaches[183–185].

¹Pierre-Simon (Marquis de) Laplace * Mar. 23, 1749 †Mar. 7, 1827

5.1. Minimum Fisher Regularisation

At Wendelstein 7-X, the ~~multicamera~~^{2-camera}, multichannel bolometer diagnostic system performs tomography using the *Minimum Fisher regularisation* and variations thereof for constructing a regularisation functional. This method has first been tested and established by Anton et al.[186]; and was used successfully with this system by Zhang et al[106]. The *Fisher^I information* (sometimes just *information*) of a probability density distribution $g(\vec{r})$ regarding the condition of \vec{r} is given by:

$$I_F = \int \frac{1}{g(\vec{r})} \left(\frac{\partial(g(\vec{r}))}{\partial \vec{r}} \right)^2 d\vec{r} \quad (5.3)$$

However, it's difficult to resolve the W7-X mag. island radii

The likelihood of measuring a particular value of physical quantity in \vec{r} would be described by $g(\vec{r})$. Therefore, I_F describes the amount of information such a probability distribution contains about its characteristic in \vec{r} . Assuming a distinctly peaked likelihood profile of $g(\vec{r})$, one can easily see that this method finds the quasi correct \vec{r} for this emissivity or yields the largest information at that specific \vec{r} [187]. One should note that the variance of the distribution $g(\vec{r})$, σ_g is bound by the inverse of the Fisher information or that its accuracy is limited by I_F , which is given by the *Cramér–Rao^{II} bound*:

$$\sigma_g \geq \frac{1}{I_F} .$$

In other words: the solution of the Minimum Fisher regularisation (*MFR*) with the smallest information has maximum variance and is the smoothest. Furthermore, MFR has shown a good stability and robustness towards noisy data and is more suited for similarly smooth distributions, i.e. not peaked as described above[188, 189]. *This is the reason why it can not resolve the distinctly poloidally varied emissivity in the W7-X SOL.*

^ISir Ronald Aylmer Fisher, FRS * Feb. 17, 1890, †July 29, 1962

^{II}Calyampudi Radhakrishna Rao, FRS * Sep. 10, 1920; Harald Cramér * Sep. 25, 1893, †Oct. 5, 1985

modified to a weighted first order derivative functional by introducing a diagonal matrix \mathbf{W} with $W^{(i,i)} = W^{(i)}\delta_{i,j} > 0$. In the n th iterative step of the algorithm, with $\nabla_{x/y}$ the corresponding discrete vector differential operator in one dimension, $\mathbf{H}^{(n)}$ becomes:

$$\mathbf{H} \rightarrow \mathbf{H}^{(n)} = \nabla_x^\top \mathbf{W}^{(n)} \nabla_x + \nabla_y^\top \mathbf{W}^{(n)} \nabla_y . \quad (5.4)$$

~~Looking back at section 5.1~~ One can also assume that $dI_F = (g'(\vec{r}))^2/g(\vec{r}) = (\nabla g(\vec{r}))^2/g(\vec{r})$, corresponding to the originally posed first order linear regularisation with a factor of $1/g$. Therefore, the functional operator \mathbf{H} for finding g with the lowest Fisher information becomes:

$$\begin{aligned} n = 0: \quad \mathbf{W}^{(0)} &= \mathbf{1}, \rightarrow \mathbf{H}^{(0)} = \Delta^\top \cdot \Delta , \\ n \geq 1: \quad \mathbf{W}_{i,j}^{(n)} &= \begin{cases} \left(1/g_i^{(n-1)}\right) \delta_{i,j}, & g_i^{(n-1)} > 0 \\ W_{\max} \delta_{i,j}, & g_i^{(n-1)} \leq 0 \end{cases} . \end{aligned} \quad (5.5)$$

For $n = 0$, singularity is avoided by letting \mathbf{W} be the unit diagonal matrix $\mathbf{1}$ and hence \mathbf{H} become the second order linear regularisation functional. At and beyond $n \geq 1$, the inverse of in the previous step calculated distribution $g_i^{(n-1)}$ yields particular smoothness for regions of small values by adding statistical weight to their corresponding second order gradients, while for larger numbers singular local structures can be amplified. For negative $g_i^{(n-1)}$, the weights are limited by an upper limit W_{\max} that is chosen beforehand on experience with the underlying reconstruction problem. Iteration of n finds the solution to the initial problem in equation (5.1) for \vec{x} by substituting $K \rightarrow \mathbf{H}^{(n)}$ until a minimum desired χ^2 is found. Let us derive a discrete and iterative set of equations and identities that can be used for a data set \vec{b} , provided by the bolometer camera system to calculate the two-dimensional radiation distribution \vec{x} with the minimum Fisher information I_F :

$$\begin{aligned} x &\rightarrow r, i \quad y \rightarrow \vartheta, j \\ \nabla_x &\rightarrow \nabla_r = \frac{1}{\Delta r} (\mathbf{D}_{\text{dia}}^{(n_\vartheta)} - \mathbf{D}_{\text{dia}}^{(0)}) \\ \nabla_y &\rightarrow \widetilde{\nabla}_\vartheta = \frac{1}{\Delta r \Delta \vartheta} (\mathbf{D}_{\text{dia}}^{(1)} - \mathbf{D}_{\text{dia}}^{(0)}) \\ &\rightarrow \mathbf{H}^{(0)} = \nabla_r^\top \mathbf{1}^{n_r \times n_\vartheta} \nabla_r + \widetilde{\nabla}_\vartheta^\top \mathbf{1}^{n_r \times n_\vartheta} \widetilde{\nabla}_\vartheta \end{aligned} \quad (5.6)$$

5.1. Minimum Fisher Regularisation

The above dimensions shall correspond to the commonly used notations for the cylindrical coordinate system, i.e. $\vec{r} \rightarrow (r, \vartheta)$ and their pixel and matrix indices (i, j) . The discrete vector differential in radial direction ∇_r is written as a combination of two diagonal matrices, where $\mathbf{D}_{\text{dia}}^{(k)} \in \mathbb{R}^{n_r \times n_\vartheta}$ corresponds to

$$(\mathbf{D}_{\text{dia}}^{(k)})_{q,p} = \begin{cases} \delta_{q,p-k}, & k \geq 0 \\ \delta_{q-k,p}, & k < 0 \end{cases},$$

which for $k = 0$ gives the unit matrix $\mathbf{1}^{n_r \times n_\vartheta}$. A corresponding poloidal differential operator ∇_ϑ is slightly modified by dividing with the radial bin $1/\Delta r$ to further mitigate noise along the flux surfaces in accordance to Fisher information in section 5.1. Using equation (5.6) and equation (5.1) yields an expression for the calculated radiation distribution in the $(n + 1)$ -th step:

$$\vec{x}^{(n+1)} = (\mathbf{T}^\top \mathbf{T} + \mu \mathbf{H}^{(n)})^{-1} \mathbf{T}^\top \vec{b}. \quad (5.7)$$

Computationally, the inversion $(\cdot)^{-1}$ is the most costly operation of this algorithm, though using mathematically optimized and performant applications such as *SuperLU*¹[190] makes this feasible. Iterations in n are performed until:

$$\begin{aligned} (\chi^2)^{(n)} &= (\mathbf{T}\vec{x} - \vec{b})^\top (\mathbf{T}\vec{x} - \vec{b}) \leq \chi_{\min}^2, \\ \|\vec{x}^{(n)} - \vec{x}^{(n-1)}\| &\leq \sigma_{\min}, \end{aligned} \quad (5.8)$$

where χ_{\min}^2 and σ_{\min} are threshold values for terminating the iteration process. The smaller both of these values are set to, the longer the calculation takes and theoretically the more accurate the solution in \vec{x} is according to the above, however the quality of the resulting profile is, from experience, more tied to the preparation of the input data, its noise and error level and the construction of the inversion domain. This circumstance will later be thoroughly explored when benchmarking the algorithm and setup with surrogate input radiation profiles and phantom image reconstructions in section 5.3. Finally, looking back at the initial proposition of minimizing

¹general purpose library for the direct solution of large, sparse, nonsymmetric systems of linear equations (*LU factorization of matrix A in a lower triangular L and an upper triangular U, A=LU*)

the Fisher information of the solution \vec{x} with an adequate regularisation in equation (5.1), one easily finds that

$$dI_F \sim \frac{(g')^2}{g} \quad \leftrightarrow \quad \vec{x}^\top \mathbf{H} \vec{x} \propto \frac{1}{g} (\nabla g)^2$$

when identifying the probability distribution $g(\vec{r})$ with the sought after emissivity profile \vec{x} and remembering the weighting in \mathbf{H} through \mathbf{W} .

The MFR can and was used successfully with the bolometer camera system at W7-X. However, different improvements perhaps have to be made to the regularisation functional weighting. Due to the nature of the diagnostic setup, the influence and behaviour of the measurement environment, i.e. the entirety of the plasma device and construction thereof, the input \mathbf{T} is rather prone to errors. Particularly the resulting tomogram in \vec{x} is very sensitive to deviations between the assumed and actual line of sight geometry, which in fact is not reflected by a larger χ^2 or σ_{\min} . Thorough evaluation of the sensitivity of both parameter coefficient matrix \mathbf{T} and resulting reconstruction to variations in the camera geometry will be performed in section 5.2. In addition to that, further exploiting *a priori* knowledge about plasma radiation distributions, especially incorporating such into equation (5.5) and deriving from that will be beneficial to the overall quality of the bolometer tomography.

check.
• $g(r)$ is the
emissivity sought!

5.1.1. Radially Dependent Anisotropy

Modifications to $\mathbf{H}^{(n)}$ on the basis of *radial radiation distribution anisotropy* will be made to improve the performance of the MFR in regard to extracting emissivity concentrations around X-points and magnetic islands from the bolometer measurements in the tomogram. The previous chapter in particular established their importance to the scientific challenges posed by the real time feedback experiments and the occurrence of (partial) radiation detachment. Let us write a discrete anisotropy factor $k_{\text{ani}}^{(i)}$ that applies varying weight to the poloidal differential operator $\widetilde{\nabla}_\vartheta$:

$$k_{\text{ani}}^{(i)} = \begin{cases} \left[\left(\tan^{-1} \left(\frac{10}{N_S} (1 - (i - N_T)) \right) + \frac{\pi}{2} \right) \times \right. \\ \left. \frac{2}{\pi} \left(\frac{k_{\text{core}}}{2} + k_{\text{edge}} \right) \right] - 1 & , k_{\text{core}} > k_{\text{edge}} \\ \left[\tan^{-1} \left(\frac{10}{N_S} (i - N_T) \right) + \frac{\pi}{2} \right] \times \\ \frac{1}{\pi} (k_{\text{edge}} - k_{\text{core}}) + k_{\text{core}} & , \text{else} \end{cases} . \quad (5.9)$$

5.1. Minimum Fisher Regularisation

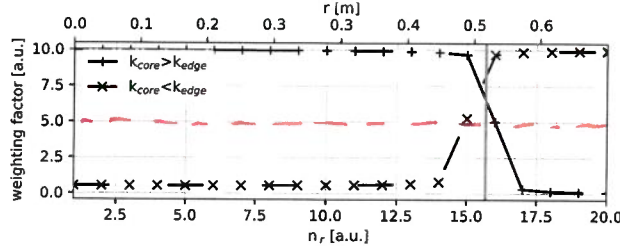


Figure 5.1.: Comparison between two radial anisotropy profiles k_{ani} for $k_{\text{core}} > k_{\text{edge}}$ and $k_{\text{core}} < k_{\text{edge}}$ each. The bottom abscissa notes the radial bin number, i.e. index and the top the corresponding radius in the $1.3V_P$ inflated cross-section. A grey line indicates the separatrix location r_a . Both lines are calculated using section 5.1.1 with $k_{\text{edge}} = 0.5$, $k_{\text{edge}} = 10$ and vice versa, $N_T = 15$ and $N_S = 2$ with a domain size of $n_r = 20$.

e.g. (5.9)

This representation applies for both favouring poloidal anisotropy inside and outside a threshold *target* radial bin $N_T \in [0, n_r]$. A parameter $N_S \in [1, n_r - 1]$ describes the width of the transition from smooth to anisotropic weighting and vice versa, while the values of $k_{\text{core}}, k_{\text{edge}} \geq 0$ represent the respective desired weight in those areas. Two examples for a radial representation of $k_{\text{ani}}^{(i)}$ can be found in figure 5.1, where each is derived for the same core and edge factors, as well as threshold and width parameters. The profiles are, if not within one or two bins of $N_T \pm N_S/2$, generally flat and can be assumed constant. Only around the threshold k_{ani} yields, depending on the width N_S , a more or less smooth transition between k_{core} and k_{edge} . For very small $N_S \leq 2$, a linear progression between core and edge anisotropy profile is expected.

The regularisation operator and functional can now be written as follows:

$$\begin{aligned} \mathbf{K}_{\text{ani}} &= \left(\frac{1}{k_{\text{ani}}^{(i)}} \delta_{i,j} \right)^{(i,j)} \hat{=} \frac{1}{k_{\text{ani}}} \mathbf{D}_{\text{dia}}^{(0)}, \\ \hat{\nabla}_\vartheta = \mathbf{K}_{\text{ani}} \widetilde{\nabla}_\vartheta &= \frac{1}{\Delta r \Delta \vartheta} \mathbf{K}_{\text{ani}} (\mathbf{D}_{\text{dia}}^{(1)} - \mathbf{D}_{\text{dia}}^{(0)}) , \\ \rightarrow \mathbf{H}_{\text{ani}}^{(n)} &= \nabla_r^\top \mathbf{W}^{(n)} \nabla_r + \hat{\nabla}_\vartheta^\top \mathbf{W}^{(n)} \hat{\nabla}_\vartheta . \end{aligned} \quad (5.10)$$

The resulting $\mathbf{H}_{\text{ani}}^{(n)}$ differs only in an additional weight to the poloidal differential from the underlying MFR algorithm. Note that the radial operator

∇_r is not changed, since deliberately enforcing individual poloidal emissivity hotspots would inevitably reduce the robustness of the calculated results and question the credibility of the anisotropy method. It is assumed that, at least in the plasma core - read: not exclusively inside the separatrix - radiation is distributed smoothly along magnetic field lines. This way, the tomography algorithm is only allowed and not constrained to find localized structures in the radiation distribution for a given set of (k_{core} , k_{edge} , N_T , N_S). This approach was also applied, particularly at W7-X by Zhang et al.[168], with the focus on a novel regularisation method that will be introduced below and used for comparison later. One should note that also Fuchs et al.[191] previously proposed a local anisotropy weighting, where there is a second set of weights introduced:

$$I_F = \int \frac{(k_{\text{ani}}^r \partial^r g(\vec{r}))^2 + (k_{\text{ani}}^\vartheta \partial^\vartheta g(\vec{r}))^2}{g(\vec{r})} d\vec{r},$$

of which the in equation (5.10) defined equations are an extension for $k_{\text{ani}}^r = 1$. One could argue that the radial variation of $k_{\text{ani}}^{(i)}$ in section 5.1.1 yields the same effect. However, this will not be further explored in this work.

5.1.2. Relative Gradient Smoothing

As noted above, Zhang et al.[106, 168] have proposed and applied another tailored reconstruction algorithm, ~~also based on the already proven[186] Minimum Fisher regularisation~~, using a novel functional with relative gradient smoothing (RGS) of the iterated profile. It has been already successfully validated using simulation results by three-dimensional simulation model results for phantom radiation distributions from EMC3-EIRENE[168]. Note though that this was done for pure hydrogen plasma with dominating oxygen impurities. The idea is to modify the expression around the Fisher information I_F after which the regularizing expression \mathbf{K} is modelled.

$$\mathbf{K} \rightarrow \vec{x}^\top \mathbf{H}_{\text{RGS}} \vec{x} \propto \left(\frac{\nabla g}{g} \right)^2 \quad (5.11)$$

The regularizing weight in \mathbf{K} becomes the inverse square of the distribution ~~$1/g^2$~~ , which corresponds to the sought ~~after~~ emission profile. The RGS

8

5.2. Camera Geometry Sensitivity Towards Line of Sight Perturbations

functional matrix \mathbf{H}_{RGS} , with respect to equation (5.6) and following, now is:

$$\begin{aligned} n = 0: \quad \mathbf{W}_{\text{RGS}}^{(0)} &= , \quad ? \\ n \geq 1: \quad \mathbf{W}_{\text{RGS}}^{(n)} &= \left(1/g_i^{(n)}\right)^2 , \quad (5.12) \\ \mathbf{H}_{\text{RGS}}^{(n)} &= \nabla_r^\top \mathbf{W}_{\text{RGS}}^{(n)} \nabla_r + \widetilde{\nabla}_\vartheta^\top \mathbf{W}_{\text{RGS}}^{(n)} \widetilde{\nabla}_\vartheta . \end{aligned}$$

This concludes the introduction of deliberately tailored tomographic reconstruction methods for the purpose of finding the two-dimensional emissivity distribution using the multicamera bolometer diagnostic at Wendelstein 7-X. Their respective application will be carried out later, after their sensitivity to the underlying geometry (perturbations) are thoroughly evaluated and potential errors or artefacts can be adequately assessed. Additional algorithms and comparisons thereof will not be highlighted here but have been in previous works[85, 186, 192].

5.2. Camera Geometry Sensitivity Towards Line of Sight Perturbations

One of ~~if not~~ the most important aspects of a tomographic inversion, with the number of absorbers $n_l \ll n_r n_\vartheta$ the number of pixels or voxels, is the accuracy and robustness of the underlying geometry ~~coefficient input~~ matrix $\mathbf{T} \in \mathbb{R}^{n_r \times n_\vartheta}$. Therefore, ~~finding~~ the local sensitivity of each LOS for a given inversion domain, i.e. size of the plasma V_p and number of radial and poloidal intersections $n_r \times n_\vartheta$, and their thorough validation through ~~comparison, establishing limits and phantom image reconstruction shall be the first step towards sensible two-dimensional emission distributions from bolometric measurement data.~~ is first studied.

In section 2.3.2 the idea of finding the individual geometric contribution of the cameras absorbers to \mathbf{T} was schematically outlined and will now be revisited and pedantically exercised in order to build an adequate foundation for the following tomography. First one has to remind themselves that both the absorber-pinhole arrangement and the construction of the bolometer cameras are ~~far from two dimensional and each yield a significant toroidal extension and are only projected onto a singular plane at $\varphi_{\text{tor}} = 108^\circ$ for~~ with a

$$(\varphi_{\text{tor}} = 105^\circ - 111^\circ)$$

due to the
HBC is tilted around its port axis
in order to adjust its LOS arrangement
distributing on the same
plane as that of the VBC.

Volume

sake of comprehensibility. It should be noted that the diagnostics geometry has already been presented in detail in section 2.2.3, where it was found that both VBC/r and HBC are tilted in direction of the magnetic axis by $\sim 5^\circ$. In equation (2.1) and equation (2.27) the idea of infinitesimal absorber and aperture subdivisions as well as differential etendues was introduced. However, in practice this challenge can not be met with analytical means and has to be solved discretely. Therefore, both pinhole and detector are divided into n_A and n_M smaller fractions, respectively. Let us assume an ~~area~~ for tomographic inversion of V_p divided into $N_\theta \cdot N_\varphi$ voxels, i.e. ~~1.3 V_{LCFS}~~ into $30 \times 120 \times 10$ partial volumes. Let $T_M^{(i,j,k)}$ be the local emissivity of absorber M to radiation in voxel $v^{(i,j,k)}$. With $L_{p,q}^{(i,j,k)}$ the LOS section length from differential absorber $dA_M^{(p)}$ through differential aperture $dA_A^{(q)}$ (see equation (2.26)) inside voxel $v^{(i,j,k)}$, the geometrical contribution to pixel $p^{(i,j)}$ can be written as:

$$T_M^{(i,j)} = \sum_{k=1}^{N_\varphi} T_M^{(i,j,k)} = \sum_{k=1}^{N_\varphi} \left(\int_M L_M^{(i,j,k)} d\widetilde{K}_M \right) \\ = \sum_{k=1}^{N_\varphi} \sum_{p,q}^{n_M, n_A} L_{p,q}^{(i,j,k)} \left(\frac{\cos(\alpha) \cos(\beta)}{2\pi d^2} \right)^{(p,q)} dA_M^{(p)} dA_A^{(q)}. \quad (5.13)$$

The superscript (p, q) on the fraction is used for simplicity and denotes that the incident angles α and β between LOS and face normals, as indicated in figure 2.7, as well as the distance d between the centers of $dA_M^{(p)}$ and $dA_A^{(q)}$ have to be calculated for each of the fractional absorber and aperture. The resulting etendue $T_M^{(i,j)}$ for pixel $p^{(i,j)}$ is in units of $[m^3]$ and corresponds to the partial volume of a LOS cone created by projection of absorber M through its respective pinhole. (T_M is not the volume of a LOS...)

? Surface

5.2.1. Absorber and Aperture Segmentation

The first challenge is to find and verify the etendues for all bolometer detectors. Two common segmentation methods for dividing the absorbers and apertures into $N \in \{2, 4, 8\}$ parts are presented in figure 5.2. A comparison shows the varying location of the face (area) center and size of the individual subdivisions for an exemplary object, i.e. pinhole or detector in a stylised perspective. On the left, a rectangular interpolation is shown next

* Let $T_M^{(i,j,k)}$ be the contribution of the local emissivity in voxel $v^{(i,j,k)}$ to the absorber M .

5.2. Camera Geometry Sensitivity Towards Line of Sight Perturbations

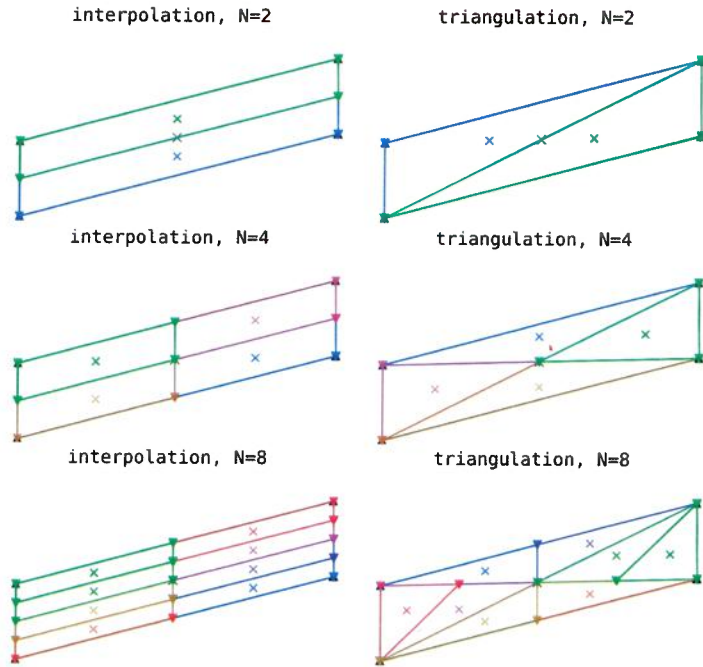


Figure 5.2.: Example for variations of subdividing the individual detectors and apertures with increasing number of compartments. Shown on the left is a method of rectangular splitting, on the right using a simple triangulation procedure for $N \in \{2, 4, 8\}$ the number of compartments. Each individual subcompartment is coloured differently (except for $N=8$ case).

to a common *Delaunay*^I triangulation on the right. Resulting subdivisions of the interpolation are constructed by dividing the longer and shorter if applicable sides of the respective face alternatingly m times in that order, which yields $N = 2^m$, $m \in \mathbb{N}$ parts. The triangulation is done using built-in functions for such Delaunay algorithms, e.g. Python's *SciPy*^{II} toolkit, limited to the same amount of segmentations as on the left for sake of comparability. Simply put, this method finds the set of triangles for a given set of discrete points \mathbf{P} inside its corresponding *convex hull*^{III} where no circumcircle of any triangle contains another point of \mathbf{P} , while a maximum of all individual

^IBoris Nikolajewitsch Delone * Mar. 15, 1890 †Jul. 17, 1980

^{II}a collection of mathematical algorithms and functions built on the NumPy extension

^{III}or convex envelope of a shape is the smallest convex set that contains it entirely

minimum angles of those triangles is achieved. The presented rectangular interpolation finds N parts of same size and shape for a given splitting of m times. However, the segmented face centres are spread rather unevenly with respect to the full absorber or pinhole, which similarly affects the set of (α, β, d) . For a triangulation of $N \geq 4$, which is a common setting, those are spread more uniformly, while $dA_X^{(i)}$ is not necessarily constant. A homogeneous distribution though is expected to yield a more accurate result due to the previously discussed locally varying transmission between aperture and pinhole in figure 2.8 and equation (2.1). equation (5.13) only computes the etendue for each fractional detector and pinhole combination once based on the individual differential area center, hence the accuracy of \mathbf{T} is assumed to benefit from a diversified segmentation, which in fact will be verified below. Based off of those splitting methods, comparisons in LOS geometry, etendues, volumes and finally sensitivity matrices will be performed.

In figure 5.3 a visual comparison between different segmentation resolutions and their three-dimensional coverage is shown for a typical $1.3V_P$ inflated equilibrium flux surface domain with toroidal expansion. The left image (a) shows the impact of dividing both pinhole and detector into two and eight parts respectively, while projecting the different lines constructed through the individual center and corner points onto the opposite side of the torus. They form a trapezoidal polyeder whose convex hull is illustrated as a cone using different colours. Both of the red boxes are achieved by finding the full extension of the LOS from the noted absorbers and corresponding aperture, i.e. tracing each corner of the detector face through any from the pinhole onto the enclosing plane and finding their convex hull, which takes also the lowest transmissible areas or geometry of the etendue into account - see figure 2.8. An infinitesimal splitting finds the full transmission for this construct, while one has to keep in mind that this theoretically takes $\geq 2N^2 \cdot n_\varphi n_r n_\vartheta$ iterations to find $L_{p,q}^{(i,j,k)}$ the intersection of LOS and voxel without prior knowledge about its geometry. For $N \rightarrow 10^3$ this alone requires 3.6×10^9 operations, which justifies the reduction of number of segments to eight each in this case. One immediately finds that splitting both absorber and aperture into eight segments each (green) yields a significantly improved coverage of the full LOS cone compared to $N = 2$ (blue). The latter has a spatial discrepancy to the enclosing projection at the opposite of the torus of $> d\varphi d\vartheta r_a$, while for $N = 8$ this is reduced to $< 1/2 d\varphi d\vartheta r_a$. Since the depicted channels are

5.2. Camera Geometry Sensitivity Towards Line of Sight Perturbations

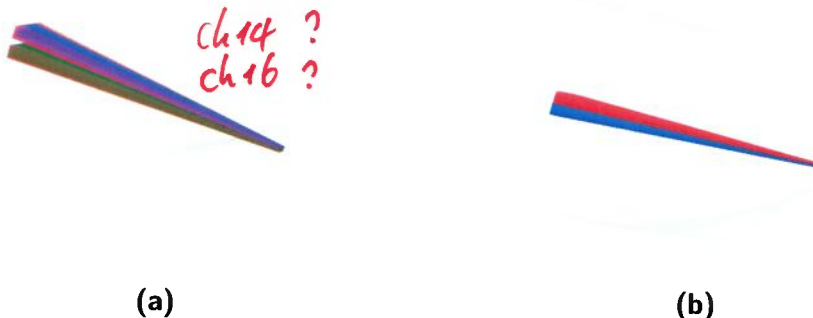


Figure 5.3.: (a) Comparison for example LOS cones for channel 14 and 16 of the HBC with rectangular splitting at (blue) $N = 2$ and (green) $N = 8$ for both the detector and pinhole. Shown in both cases is the *full* LOS cone in red, created by projecting detector corners through respective opposite side corners of the pinhole, and the sum of the individual N^2 cones from the center of the detector elements through the corners of the pinhole rectangles in a different colour. **(b)** Line of sight cones from $N = 8$ split detectors and pinholes of neighbouring channels 15 and 16 of the HBC in red and blue. In both images, all of it is enclosed by a grey mesh, representing the previously introduced $1.3V_P$ hull of the extrapolated magnetic flux surfaces, wherein the LOS cones are defined and their volume calculated.

14 and 16, which are positioned almost perfectly symmetrical around the center detector and camera axis, it is assumed that this visual approach and conclusion are adequately supported. The left figure 5.3:(b) shows neighbouring LOS cones of channel 15 and 16 for $N = 8$. No gap is found between them, while they also do not cover the same volume twice or overlap at any point. In fact, in figure 2.22 one can already see that the poloidal LOS coverage in the plane of the bolometer, for a set of $n_r = 30$ and $n_\theta = 150$ at $N = 8$, particularly from the HBC is very good and features no local voids or irregularities. Only the fan of the first five VBCI detectors towards the outboard side over the magnetic axis, indicates a one pixel wide gap from $0.75r_a$ to the boundary of the mesh. However, this area is entirely viewed by the horizontal camera. One remembers that the systems spatial resolution at the magnetic axis is 5 cm, which is in agreement with this assessment of the LOS cones.

* These are soft-x ray channels covered w. 12 μm Be-foils.

241

Not for the tomography purpose. Delete this part.

5.2. Camera Geometry Sensitivity Towards Line of Sight Perturbations

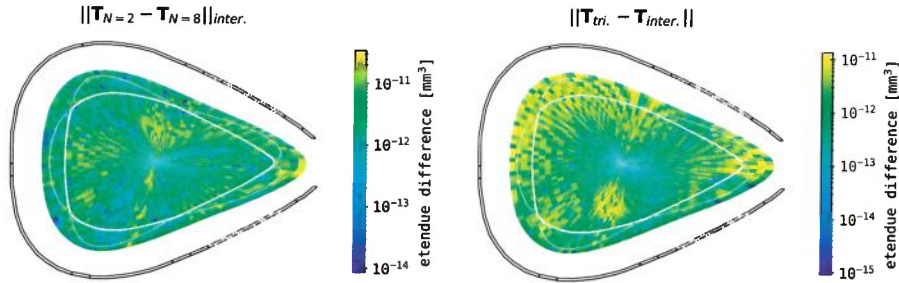


Figure 5.5.: Comparison between the total etendue or local sensitivity of the LOS system of the bolometer for different interpolation resolutions and methods. For both, the absolute logarithmic value of the difference between the sensitivities is plotted on the respective mesh grid that has been used to calculate the etendues. A Poincaré plot for the associated magnetic field is superimposed, showing the last closed flux surface and enclosing magnetic islands at that toroidal location. This is enclosed by a cut through the first machine wall. The left image shows the difference between $N = 2$ and $N = 8$ rectangular interpolations, while the right similarly displays the contrast between the prior and triangulations of the same resolution.

Are you sure?
This seems to be
the outer vessel.

Where ?

of the camera constructions impact on \mathbf{T} will be done further below.

Finally, figure 5.5 shows the variation between individual pixel distributions of \mathbf{T} for different refinements and segmentation methods for the same grid mesh as introduced for figure 2.22 of all bolometer camera arrays combined. The left figure presents the absolute difference on a logarithmic scale between $N = 2$ and $N = 8$ for a rectangular subdivision across the inversion domain. Centred around the magnetic axis, structures of higher and lower absolute deviations alternate in poloidal direction and extend as far as the boundary. In certain areas, e.g. the top and outboard side, those rays are interrupted by areas of randomly distributed values which also feature $\Delta K_M \sim 0$. The most prominent parts in this plot are the areas of higher discrepancy in the center towards the inboard island and along the edge of the VBCI array, from the lower side across the magnetic axis towards the top of the triangular plane, as well as the intersecting darker lines. With respect to the integrated etendue and LOS volume per channel with an order of magnitude of $\sim 10^{-10} - 10^{-14} \text{ mm}^3$, a variance of $0.5 \times 10^{-10} - 10^{-14} \text{ mm}^3$ is of no

importance to the initial challenge of tomographic reconstruction of bolometer measurements. Looking back at the central MFR iterative expression for the radiation profile $x^{(n)}$ in equation (5.7), a variation of 10^{-11} mm^3 in \mathbf{T} becomes negligible when evaluating the inversion since the condition of this expression is no longer only dominated by the geometry matrix. Particularly, assuming the variation or perturbation to \mathbf{T} , $\Delta\mathbf{T}$ be structured and not infinitesimal, which is very much true for this example, Ghaoui et al.[193] find that the error in the inversion is limited by the product of condition and euclidean norm $\kappa(\Delta\mathbf{T}) \cdot (\|\Delta\mathbf{T}\| / \|\mathbf{T}\|)$. Since $\kappa(\Delta\mathbf{T})$ is in fact potentially large but its norm significantly smaller, this upper limit underlines that such a difference in local sensitivity, i.e. variations in N correspond to perturbations of appropriate dimension and do not catastrophically change the results in $x^{(n)}$. Looking at the right plot in figure 5.5, which shows the difference between triangulation and rectangular subdivision at $N = 8$, one finds a very similarly looking and scaled image. However, the previously noted structures along the VBCI are far more extended and wrap along the separatrix towards the inboard side and enclose the areas of lower variations. Variations in colour can be attributed to its changed range of $10^{-11} \text{ e} - 15$. The same arguments as above towards the impact of changing between those segmentation methods on the reconstruction apply here as well.

So far it has been established that the segmentation of aperture and absorber and therefore finding a discrete, pixel or voxel based representation of the geometry ~~coefficient~~ matrix \mathbf{T} containing the etendues of all individual bolometer camera channels is adequately achieved by either triangulation or rectangular splitting with a resulting number of subdivisions $N > 4$, given a common setting of reconstruction grid expansion and refinement (i.e. $1.3 \times 150 \times 20 \times 10$, see above). From here on, we will assume that any ~~any~~ given etendue, LOS volume or results derived therefrom are computed using a detector and pinhole triangulation with $N = 8$.

5.2.2. Line-of-Sight Geometry Perturbations

In the following paragraphs, a variation of perturbations to the presented geometry in section 2.2.3 and its effect on the ~~corresponding~~ parameter ~~coefficient~~ matrix \mathbf{T} in figure 2.22 will be discussed. This is done to test the robustness of the outlined approach to deviations in the designed construc-

5.2. Camera Geometry Sensitivity Towards Line of Sight Perturbations

tion and investigate upon the minor asymmetry in the forward calculated chord brightness profile from the ~~otherwise ideally symmetrical STRAHL~~ 13 radiation distribution.

Centered Aperture and Camera Array

In a complex and large machine that experiences strong thermal effects during preparation and experiments such as Wendelstein 7-X, changes in the actual geometry of the diagnostic in comparison to the initially proposed design are not uncommon and in fact expected. Furthermore, this potential displacement is not constant either and can vary over multiple experimental campaigns. Hence, an ~~automated, robotic, high precision location measurement~~ of all pinholes for HBC and VBCI/r was conducted before the very first plasma and after the last experimental campaign OP1.2b. The provided benchmark data revealed that the HBC camera aperture, i.e. its *barycentre*, is displaced off the ~~center of the machines vertical axis, which ideally is aligned also with the magnetic axis~~, by a few millimetres at $\vec{r} = \{-1.99 \text{ m}, 6.152 \text{ m}, 1.735 \text{ mm}\}$. The LOS geometry of the HBC is assumed to be symmetrical and cover the plasma area evenly, thus potentially introducing a significant perturbation by this shift to the inversion. Hence, a first test of the ~~robustness~~ of T is conducted by finding a hypothetical, ~~centred at $z = 0$ horizontal camera that otherwise has the same geometry as the original HBC~~ mid plane of W7-X ($z=0$) with $z=-1.735 \text{ mm}$. ~~Comparing ideal and actual~~ Comparing ~~with the actual~~ T-variation profiles are compiled accordingly.

A comparison between the ~~original and shifted~~ ideal and actual geometry with respect to the viewed plasma volume, as well as its impact on the local sensitivity in the triangular plane is shown in figure 5.5. The left set of red LOS rays is produced by tracing from the center of the detector through the center of the respective aperture. In this case, the new pinhole is constructed by shifting its center to $z = 0$ and tilting it so that its face normal points towards $\{0, 0, 0\}$. A resulting rotation and transposition between this and the original aperture is similarly applied to each detector of the horizontal camera array. The minor ~~differences~~ between the black and red LOS are, as expected, constant across the fan. Variations in etendue between the shifted and as-designed HBC on the right are roughly of same order of magnitude as the previous comparisons for selected segmentation methods in figure 5.5. However, its distribution is aligned with the orientation and geometry of the

(not true)

mid plane of
W7-X ($z=0$)
with $z=-1.735$
mm.

difficult to see
the differences
using an inset
to enlarge a
part?)

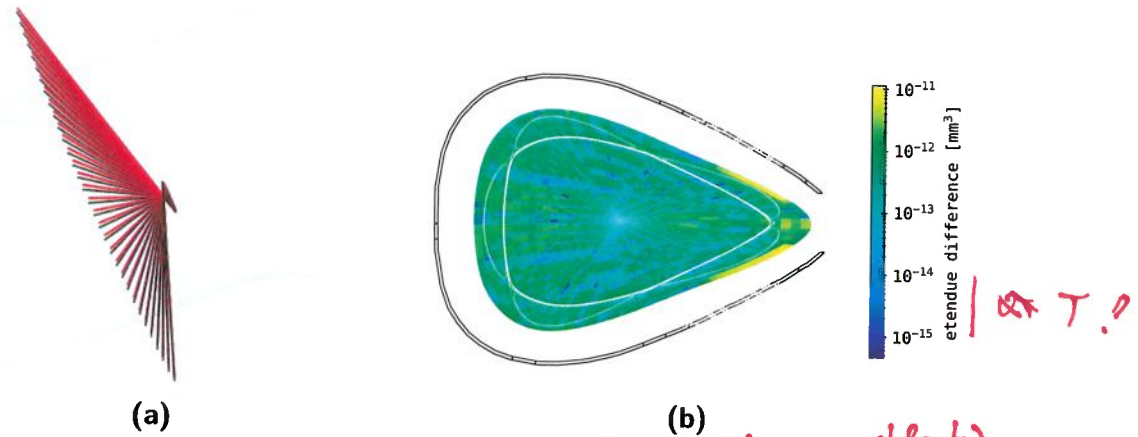


Figure 5.6.: (a) Comparison of center LOS of the ~~original~~ ^{idea} HBC geometry and an adjusted ~~geometry~~ ^(red) geometry, where the pinhole and respective camera array have been centred around $z = 0$, the vertical dimension of the W7-X coordinate system. **(b)** Impact of the geometry changes in (a) to the collective ~~etendues~~ ^{etendue} of the horizontal bolometer camera, calculated and portrayed as in figure 5.5.

!!
etendue $\neq T$
(see D.Zhang, NF, 2021)

~~for adjuste
one!~~

fan and features up-down symmetric, alternating structures in level of perturbation. They are approximately three LOS wide and each is intersected by single-pixel thick lines of lower ΔT in horizontal direction. In-between those bundles are individual LOS that have similarly reduced values, which again are bounded by single pixels of comparable variation. This is repeated in both directions towards the boundary of the evaluation domain, i.e. the edge of $1.3V_p$. Less prominent are underlying areas of slightly higher and lower variance, alternating in poloidal direction, with greater ΔT in front of the pinhole and on the opposite, inboard side. The largest discrepancy between the original and hypothetical camera geometry coefficients can be found on both sides, closest to the aperture, along the edge of the reconstruction area and inboard magnetic islands.

Based off of the results in figure 5.6 and the approach presented in equation (4.19) and following, one can easily now evaluate the impact of said displacement to the chord brightness profiles measured by the horizontal bolometer. Using the same STRAHL results that have been discussed in section 4.4, i.e. poloidally symmetrical radiation distributions and the new geometry coefficients T for a ~~centred and upright~~ HBC pinhole, this is

an ideal and actual

5.2. Camera Geometry Sensitivity Towards Line of Sight Perturbations

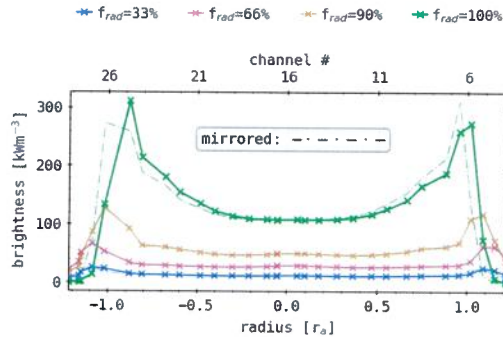


Figure 5.7.: Forward integrated chord brightness for the HBC at different f_{rad} for previously presented STRAHL results in figure 4.51 using the ~~adjusted, hypothetical~~ camera geometry from figure 5.6.
actual and ideal , respectively

~~compared~~

achieved in figure 5.7. As before, this image features a semi-transparent mirror image of the corresponding other half of the profile superimposed on each side for all radiation fraction levels. It has already been established that the original geometry yields asymmetric results, which is also very clearly true for this hypothetical camera arrangement. In fact, in direct comparison to the initial $\sim 2\text{--}5 \text{ kW/m}^3$ difference between the measured brightness along the separatrix before, the variation around $\pm r_a$ is significantly increased. For all f_{rad} , the profile is not only different at its peak around the LCFS but also at the center. At 100% radiation fraction, the brightness is shifted towards $r = 0$ and about 30 kW/m^3 higher on the lower side than on the top, i.e. $+1.0r_a$. This shift and increase can be found for all lower f_{rad} , however at a correspondingly smaller level. In contrast to figure 4.51, the two local maxima around the separatrix differ also qualitatively, where the lower side peak is very sharp, and the other is more akin to the previous shape. The portrayed changes to the camera geometry have shown to yield no more symmetric forward modelling results than the corresponding original LOS. This particular hypothetical generally yields a greater level of discrepancy between each channel and its respective counterpart than is the case for an unperturbed HBC. Therefore, the initial asymmetry in chord brightness can not be attributed to this deviation and not be corrected by its resulting transformation. However, this perturbation to the etendue ~~coefficients~~ in \mathbf{T} has produced large changes in the brightness profiles and thereby underlined

✓ the importance of camera geometry towards the experimental measurements
and the tomographic reconstruction's adequacy.

for performing

Unilateral Camera Array Mirroring *(this part is not necessary.)*

A second variation to the horizontal camera is constructed by applying a rotation and transposition to one half of the array, i.e. channels 16 through 32 that adjusts their geometry to be in one plane with the remaining detectors and a mirror image of their counterpart. This hypothetical *mirror* (plane) would be one that is spanned by the normal of the LOS fan and the direction of channel no.15. The transformation is constructed so that the new location and orientation of absorber no.32 is equal to that of no.1, rotated by the opening angle of the camera 53° . Similarly, channel no.31 becomes the mirror opposite of no.2, rotated by $53^\circ - \angle(L\vec{O}S(1), L\vec{O}S(2))$ and so on. Resulting deviations to the original geometry are so small that a three-dimensional representation like in figure 5.6 yields no visible distinction between the two. Hence, figure 5.8 shows the etendue variation and the forward model integrated chord brightness profiles, again as in figure 4.51 for increasing levels of f_{rad} for this proposed adjustment to \mathbf{T} . The change in local sensitivity is, as instructed above, limited to the upper half of the camera array, while it is two orders of magnitude lower than before at $< 10^{-13} \text{ mm}^{-3}$. No particular features akin to the structure of the LOS fan can be found here, while there is again a more prominent area of increased ΔT closer to the aperture and inboard magnetic island.

$\frac{\Delta T}{T} = ?$
Should be presented!

The chord brightness profiles for varying f_{rad} on the right of figure 5.8 are constructed the same way as before. With respect to the initial results, a decrease in variance between left and right half of the plot can be noted when inspecting the corresponding mirrored, semi-transparent lines. However, this minuscule deviation in the range of 0.5 – 1% is found in profiles produced from both intrinsically symmetrical camera geometry and radiation distributions. All possible sources of asymmetry besides the toroidal extension of the array have been eliminated in order to produce this plot. Therefore, one has to conclude that at least some level of asymmetry in previously and hereafter measured or forward integrated HBC profiles is due to the tilt of the LOS fan of 68.75° . Furthermore, the difference between this chord brightness profile and the initial results using the original geometry from figure 4.51 hence is dominated by the variation among the individual

5.2. Camera Geometry Sensitivity Towards Line of Sight Perturbations

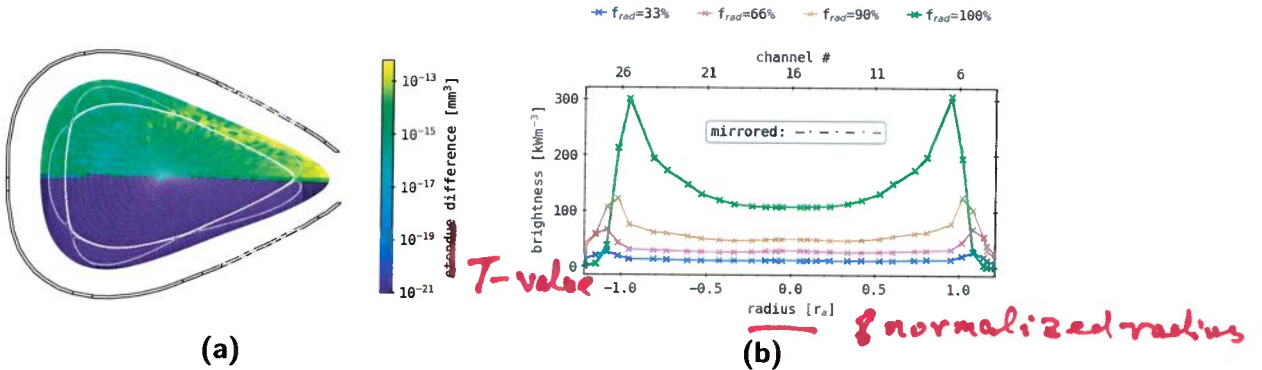


Figure 5.8.: (a) Impact of geometry changes on the ~~collective etendues~~ of the horizontal camera, where one half (*upper*) of the camera array has been rotated so that all channels lie in one plane and each is the exact mirror opposite - the *mirror* being a plane defined by the camera aperture normal, perpendicular to the LOS fan - of one from the other half. **(b)** Forward ~~integrated~~ chord brightness for the HBC at different f_{rad} for previously presented STRAHL results in figure 4.51 using the hypothetical camera geometry from (a). *geometry matrix calculated*

horizontal camera LOS.

The evaluation of this perturbation in T is concluded by underlining the fact that a change of this magnitude, i.e. 10^{-2} times smaller than the variability of different segmentation methods, yields almost no variation in forward calculation.

Upright and Virtual Horizontal Bolometer Camera

An obvious continuation of the previous geometric variation is to not only correct the intrinsic rotation within the as-designed HBCm camera array, but to extend the transposition of figure 5.6 to $z = 0$ with a rotation of the entire LOS fan into an upright orientation. The resulting artificial projections in red are shown in figure 5.9 in comparison next to the original horizontal camera in black. In addition to the shift of aperture and detector assembly to be centred around the horizontal axis of the machine, both are rotated individually into an equally perpendicular position to the latter. The new, centred fan, constructed by adjusting each absorber-pinhole trace into one plane - see the previous geometric perturbation above - , is rotated

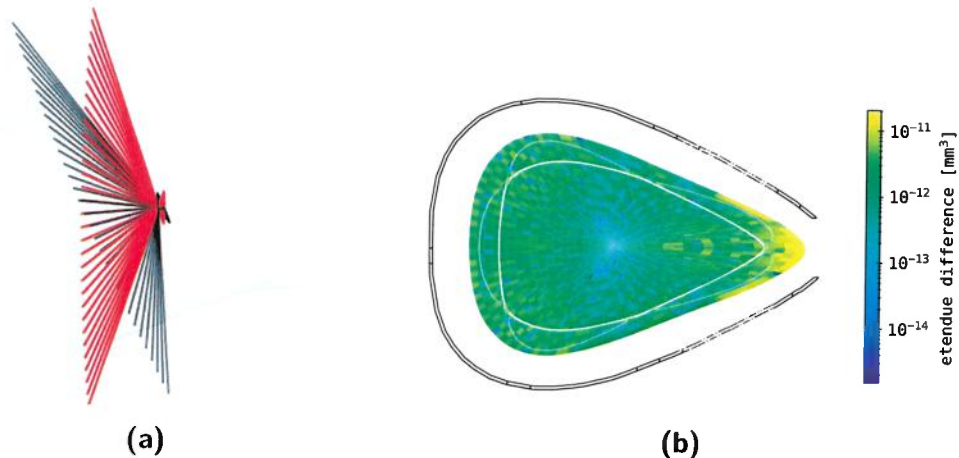


Figure 5.9.: (a) Comparison of the (black) original HBC LOS fan and (red) changed geometry, where the entire camera array has been rotated so that all channels lie in one plane that is vertically upright and centred around $z = 0$, the vertical dimension of the W7-X coordinate system. **(b)** Impact of the geometry changes in (a) to the collective etendues of the horizontal camera.

Wrong! $x=0$
 $y=0$
W7-x center.

so that their two-dimensional projections in (x, y) are pointing towards $\{0, 0\}$. The aperture is also rotated into a position where its longer side, i.e. in direction of the detector array, is now also upright. Effectively, only a small transposition and rotation around the axis between pinhole center and device origin have been done and the size of the absorbers themselves, their nearest neighbour distance and respective position within the camera were not altered.

The right plot in figure 5.9 yields a level of perturbation similar to earlier at up to 10^{-11} mm^{-3} , with similar structures and distribution as in figure 5.5. Areas of lower error and variation around the magnetic axis between the upper and lower, center X-points are enveloped by largely homogenous deviation around $0.5 \times 10^{-12} \text{ mm}^{-3}$. Within both are individual pixels where the etendue difference is orders of magnitude smaller, distributed however with no recognizable pattern. The largest change in local sensitivity can be found, again, right in front of the aperture at the tip of the triangular plane and around the outboard magnetic islands.

Consistent with the earlier geometric evaluations, the forward model integ-

5.2. Camera Geometry Sensitivity Towards Line of Sight Perturbations

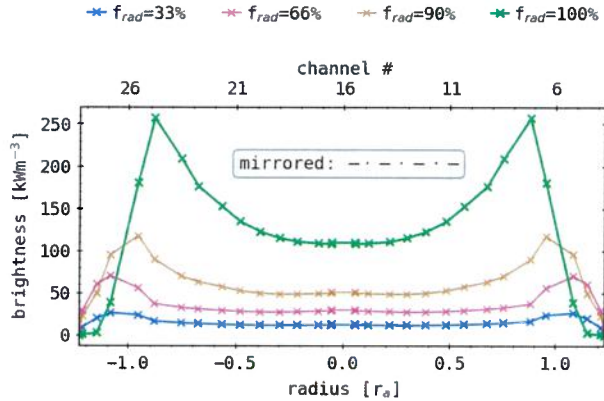


Figure 5.10.: Forward integrated chord brightness for the HBC at different f_{rad} for previously presented STRAHL results in figure 4.51, using the theoretical camera geometry of figure 5.9.

rated chord brightness for the STRAHL profiles from section 4.4 for varying levels of f_{rad} is calculated and presented in figure 5.11. This plot is perfectly symmetric across all radiation fractions around $r = 0$, underlined by no visible, semi-transparent mirror lines on either side. With respect to the initial results, the peak brightness for $f_{\text{rad}} = 1$ is increased to 260 kW/m^3 and significantly more localized. Furthermore, all lower levels of radiation and their maxima in particular are shifted towards the separatrix and further inside. Otherwise, the shown profiles are qualitatively very similar to the ones before.

An obvious continuation of the above geometric adjustment is to construct a pseudo artificial horizontal camera array that has absolutely no variations among its absorbers and their LOS. The attribute *pseudo* refers to this geometries' detector construction that is created by averaging size, shape and distance in-between the original HBCm absorbers that is therefore repeated 32 times to create this hypothetical device. This new, upright, centred, machine coordinate origin oriented camera with equidistant, equally sized detectors viewing the plasma through a parallel, centred aperture is also used to forward integrate the previous STRAHL results and find their respective chord brightness profiles. A plot for the varying radiation fraction levels $f_{\text{rad}} = 0.33, \dots, 1.0$ is accompanied by a two-dimensional deviation map in the triangular plane between this new geometries and the actual

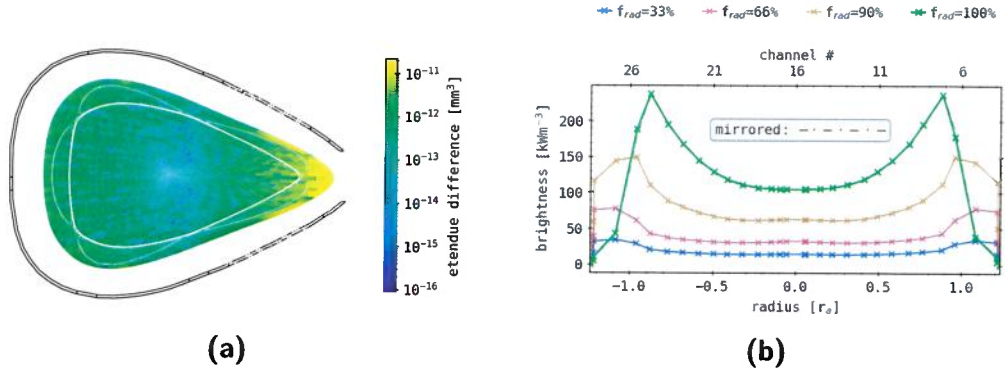


Figure 5.11.: (a) Impact on the collective etendues of the horizontal camera, where the entire array has been replaced by an artificial, symmetrical, vertically upright LOS fan with equidistant channels around $z = 0$, the vertical dimension of the W7-X coordinate system. The LOS geometry is similar to the one presented in figure 5.9. **(b)** Forward integrated chord brightness at different f_{rad} for previously presented STRAHL results in figure 4.51, using the camera geometry of (a).

local sensitivity in figure 5.11.

With respect to the previous analysis of perturbations in etendue in figure 5.9, this image presents similar magnitudes $\sim 10^{-11}\text{--}10^{-16} \text{ mm}^{-3}$ and comparable local maxima at the outboard side, closest to the pinhole of the artificial camera. Individual pixel artefacts can also be found here, though the poloidal structuring from before is far weaker and the characteristic of separate LOS can be noticed, originating at the aperture beyond the tip of the triangular domain. The also perfectly symmetric chord brightness profile on the right for $f_{\text{rad}} = 1$ is very akin to the one before, though with a slightly reduced maximum of 240 kW/m^3 . At lower radiation fractions, the intensity of the local extremes are significantly increased by up to 50% while also being further outside or even remaining beyond the separatrix. The overall shape however is still very similar.

A planar correction and rotation of the original HBCm geometry provided fully symmetrical forward model integrated measurements without significant qualitative discrepancies to those produced by the underlying camera. The change in local sensitivity between that and this particular hypothetical array is of same order of magnitude as the differences created by varying

5.2. Camera Geometry Sensitivity Towards Line of Sight Perturbations

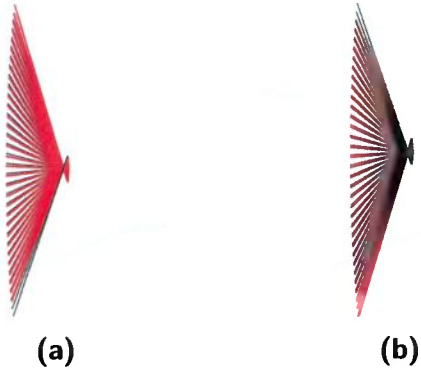


Figure 5.12.: (a), (b) Comparison of the (black) vertically upright and $z = 0$ centred (hypothetical) HBC LOS fan - see figure 5.9 - and (red) a (a) -2° (upward) and (b) $+2^\circ$ (downward) respectively tilted geometry, where the array has been rotated around the normal of the LOS plane.

detector and pinhole segmentation methods. A fully artificial horizontal camera that is achieved without any perturbation in orientation or detector construction also yields similarly symmetrical forward chord brightness profiles from STRAHL results for comparable etendue variations. On one hand, such small changes in T have the potential to significantly change the measurements and hence any thereon based reconstructions, while on the other the as-designed local sensitivity of the horizontal bolometer camera is proven to be very close to a theoretical, ideal geometry.

Aperture Displacement

As it was already mentioned above, the entire machine and therefore also the integrated bolometer multicamera system is subject to large scale thermal drifts and mechanical stresses, i.e. cooling, vacuum pumping and the high temperature experiments themselves, which inevitably impact their geometry. Before the very first plasma and after the last experiment in operation phase OP1.2b, during which the measurement results presented in this work were produced, such an automated, high precision measurement of the position of all HBC and VBCI/r pinholes was conducted. There it was found that, with respect to the original design and first position measurement before the first discharge at W7-X, the system showed a displacement of 0.5–1.5 mm for the individual corners of the apertures. This particular shift yields a

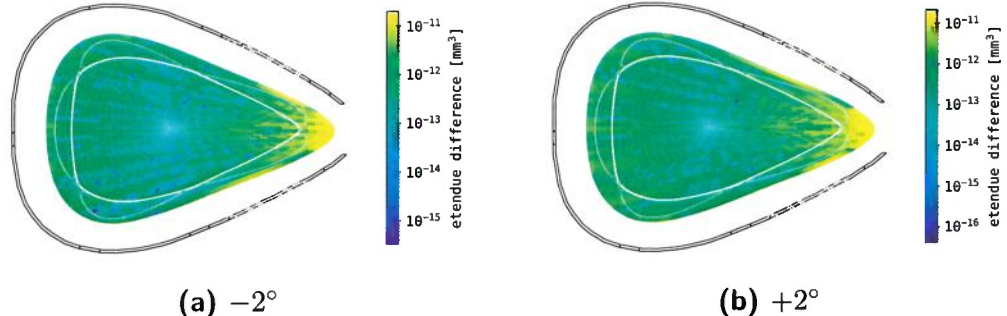


Figure 5.13.: (a), (b) Impact on the collective etendues of the horizontal bolometer camera for the theoretical geometries shown in figure 5.12, likewise respectively for (a) -2° and (b) $+2^\circ$ tilts.

downward - towards the lower side within the plane of the bolometer LOS fan - tilt of the camera of 2° . The absorber array is, due to the design of the bolometer, presumed to share the same displacement, though no equivalent estimation for their shift is available. Since there exist no additional information regarding the bolometer LOS perturbation, this deviation is assumed to neither be constant during an experimental campaign nor across the past operation and construction phases. A variation to the camera geometry of this order of magnitude was already performed when examining the local sensitivity of a vertically centred and aligned detector array. This most recent positional benchmark is of course taken into account for all prior and following calculations, however evaluating potential additional shifts during or in-between campaigns is crucial towards assessing the plausibility of experimental data reconstructions. Hence, a randomized transposition in the range of 0.5–1.5 mm is applied to the fully symmetrical, artificial LOS geometry that was achieved in the previous section. Two limiting cases, where this perturbation method yields $\pm 2^\circ$ tilt, i.e. in upward or downward direction of the fan, were chosen to gauge the impact of this error to the local sensitivity. For sake of comprehensibility, this will again only be examined in detail here for the HBCm, while the effect of disassociated forward integration and reconstruction camera geometries for phantom tomograms will be investigated upon later. The two upright and tilted LOS fans, based on the results in figure 5.9, are shown in figure 5.12 in a similar way as before. The respective variation in local sensitivity for the above set of hypothetical

5.2. Camera Geometry Sensitivity Towards Line of Sight Perturbations

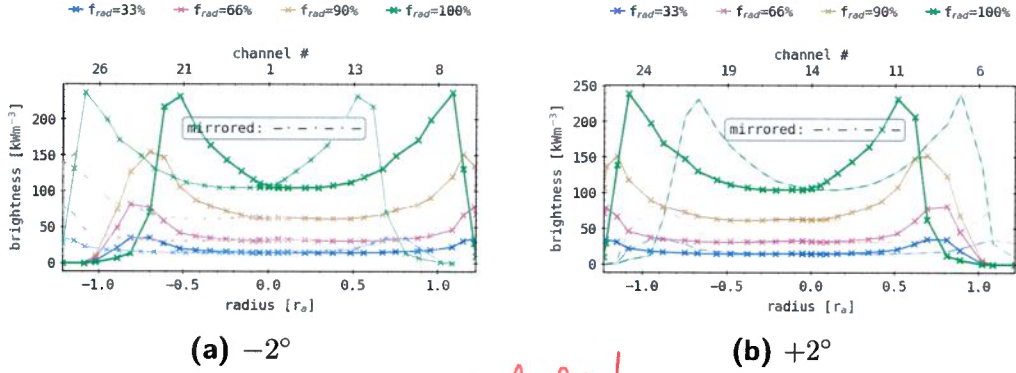


Figure 5.14.: (a), (b) Forward integrated chord brightness at different f_{rad} for previously presented STRAHL results in figure 4.51, using the theoretical geometries of figure 5.12, likewise for (a) -2° and (b) $+2^\circ$ tilts.

calculated

geometries can be found in figure 5.14. Compared to the previous differences in etendue in figure 5.11, similar structures of same order of magnitude are featured in this plot for both sets of lines-of-sight. At a misalignment angle of $+2^\circ$, the distribution appears slightly smoother, with smaller and less pronounced areas of decreased discrepancy, while the absolute range is insignificantly extended to $10^{-11}\text{--}10^{-16} \text{ mm}^{-3}$. Individual channels and their variation can be noted in the pixelated plot, though no particular features that underline the, from this perspective poloidal nature of the perturbation are noticeable. Again, the largest differences appear in front of the aperture and along the separatrix and domain boundary on the top and bottom. On the left, for a tilt of -2° , the same holds generally true, while the spectrum in etendue is slightly smaller at $10^{-11}\text{--}10^{-15} \text{ mm}^{-3}$ and a stronger, more contrasting local minimum is found around the magnetic axis and towards the middle upper and lower X-points. Singular and separate pixels of significantly decreased variance appear more frequently and with lower values here than on the right, while the maximum is again at the tip of the triangular plane. One should note that, despite the tilt in poloidal direction, there appears no gap in coverage of the reconstruction domain, i.e. the area of $1.3V_p$ by the newly constructed cameras.

Similar to the previous analysis, both of the presented LOS geometries and their corresponding parameter coefficients are used to forward model integ-

rate the chord brightness from STRAHL results in section 4.4. However, in order to assess the impact of this specific misalignment to a measurement that is performed under the assumption of a different geometry, one has to consider the results using the ideally upright, centred and symmetrical LOS fan of figure 5.9 in this case. The profiles in figure 5.14 are calculated with the new coefficients, while being presented using the information of the symmetric geometry - the abscissa of individual LOS radii is given by the prior geometries traces through the mesh, see equation (2.28). Both $\pm 2^\circ$ show significant lateral shifts towards (a) upper and (b) lower side of the separatrix, i.e. $\pm r_a$. While the relative position and height of the individual lines and local extremes for all levels of f_{rad} stay the same, the (a) left and (b) right part of the profiles are compressed, while the rest is shifted in the opposite direction. The relocated local maxima for $f_{\text{rad}} = 1$ have been moved from $\pm 0.9r_a$ to $\pm 0.5r_a$ - the other plots show a similar behaviour, underlined by the semi-transparent, mirrored lines in both images for all radiation fractions.

These results clearly show the importance of congruent measurement or forward calculation and reconstruction camera geometries. In this scenario - arguably the worst case -, an intrinsically and fully symmetrical emissivity distribution yields highly asymmetrical and radially transposed chord brightness profiles. An inversion performed under this premise, which will be explored in more detail in section 5.3, is badly pre-conditioned since the regularisation functional, see section 5.1, that does and can not account for this order of magnitude discrepancy. Later it will be found that tomography for misalignment geometries will not be able to find plausible radiation distributions, produce misleading results or even artefacts. It is of significance however to understand such effects and their impact for later experimental data reconstructions where no in-situ information on the actual LOS geometry or perturbation thereof is available.

5.2.3. Additional Artificial Camera Arrays

Upon investigation of possible LOS and camera geometry perturbations and their impact on the local sensitivity a forward model line-integrated measurements, the question of benefiting the tomographic inversions with additional, hypothetical and tailored detector arrays arose. This is largely motivated by the observed discrepancies during reconstructions of experi-

5.2. Camera Geometry Sensitivity Towards Line of Sight Perturbations

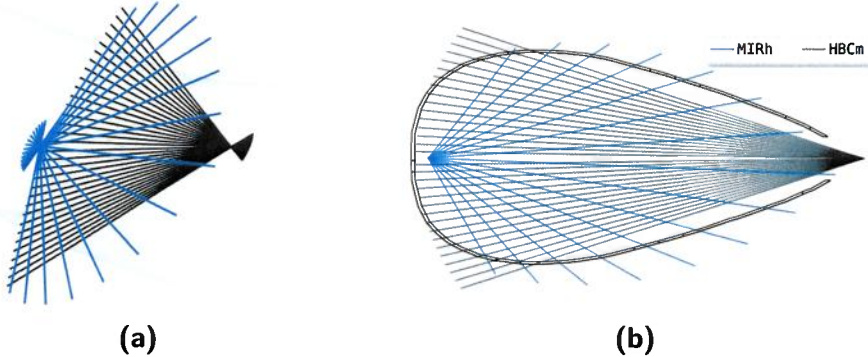


Figure 5.15.: (a) Comparison of the (black) horizontal bolometer camera LOS geometry and an artificial, *new* camera ("MIRh", blue) that is arranged opposite of the prior, spanning 15 new channels that cover the full torus cross-section homogeneously. **(b)** Same geometry comparison in projection of the toroidal plane of the bolometer camera assembly, i.e. $\varphi_{\text{tor}} = 108^\circ$.

mental data, which will be performed later in this chapter. While trying to find plausible radiation distributions that are in agreement with other diagnostics and intrinsically coherent, i.e. a temporal sequence of tomographic images shows comprehensible results, more cameras in particular locations were presumed to greatly improve upon their quality. Therefore, two sets of absorbers located opposite of the existing cameras were designed. One on the inboard side viewing the inside magnetic islands and X-points and one at the top of the triangular plane, viewing along the separatrix towards the outboard side and also the inboard island, both limited to fifteen LOS each.

Horizontally Mirrored Camera

The first new, artificial camera is presented in figure 5.15 alongside the original HBCm in both three- and two-dimensional perspective in a similar way as the previous LOS plots. This new geometry will be called **MIRh** - abbreviation/simplification of *MIRRored (horizontal) (bolometer camera)*. The array is centred around $z = 0$ and designed to cover the poloidal cross-section evenly while also having individual pseudo detectors viewing regions of particular significance, i.e. magnetic islands and X-points. It is also tilted in toroidal direction - 68.75° , therefore with a toroidal reach of $\sim 5^\circ$ - and

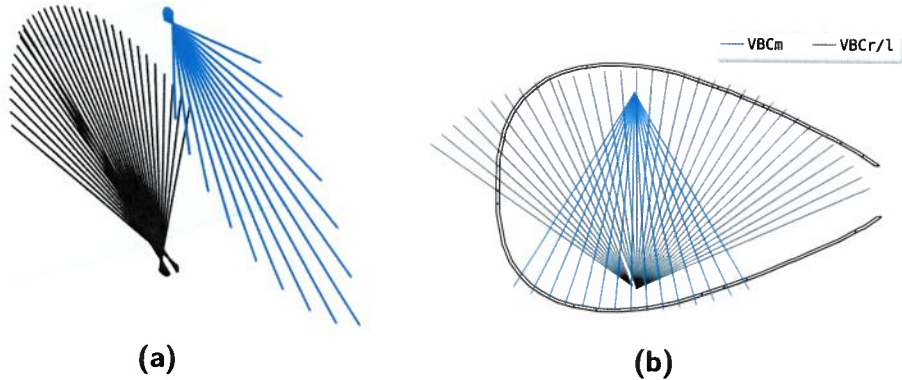


Figure 5.16.: (a) Both vertical camera arrays (black) next to a similarly *new*, artificial LOS fan of 15 channels ("VBCm", blue), which is created also opposite the VBCr aperture and covers. **(b)** Same geometry comparison in projection of the toroidal plane of the bolometer camera assembly, i.e. $\varphi_{\text{tor}} = 108^\circ$.

oriented antiparallel to its respective counterpart. Absorber size and shape within this camera are all the same and based on the respective HBCm average, while its aperture is equal to that of the latter. In contrast to the original horizontal camera, the MIRh pinhole is located much closer to the plasma and inside the enclosing first wall of the device, though the hypothetical construction puts the entire detector assembly outside said boundary, in some way being consistent with the space constraints at W7-X and the position of the VBCl/r.

Vertically Mirrored Camera

The second artificial camera is presented in a similar manner in figure 5.16 and, analogous with the prior, called *VBCm* - abbreviation for *Vertical Bolometer Camera (mirrored)*. In toroidal coordinates, this design is radially centred around the same position as the VBCr aperture center, which is reflected by its orientation in (b). The same detector dimensions with a constant spread, similar to that of the original vertical cameras, were chosen like in the previous design, though the LOS do not cover the entire, enlarged triangular plane. Their construction is solely focused on viewing the op-

5.2. Camera Geometry Sensitivity Towards Line of Sight Perturbations

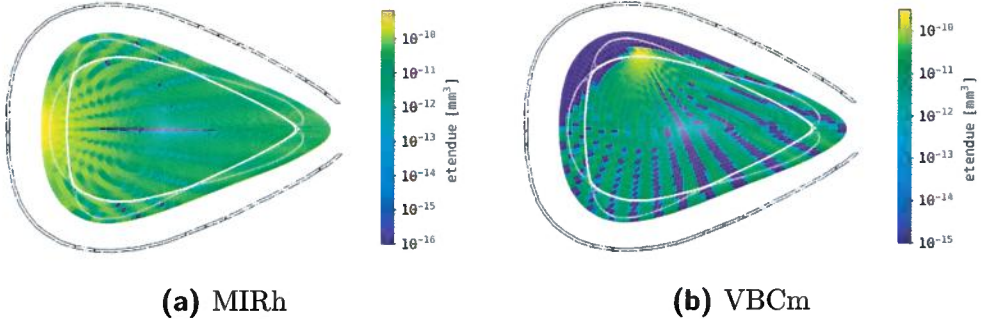


Figure 5.17.: (a), (b) Impact on the collective etendues of the entire bolometer camera system from the addition of the previously introduced *new*, artificial cameras from figure 5.16. On the (a) left, the local sensitivity of a hypothetical, horizontal camera (MIRh) is shown, while on the (b) right the same for a theoretical, vertical array can be found.

posite side X-points and magnetic islands, including those on the outboard and inboard side using multiple absorbers each. As mentioned before, its position relative to the separatrix and first wall of the device is analogous to that of the VBCI/r, i.e. the aperture is very close to the LCFS and the detector array beyond the limiting surfaces.

Figure 5.17 shows the resulting etendues of the new, artificial camera arrays on their own without any other LOS in the same way as before. In (a), the MIRh almost entirely covers the whole cross-section, except for a few singular pixels that have no etendue attributed to them in-between the individual LOS and a 1-2 pixel wide row inside the separatrix, around the magnetic axis of $\sim r_a$ length. Obviously, the maximum local sensitivity of $5 \times 10^{-10} / \text{cm}^3$ is found closest to the aperture on the inboard side, from which the etendue evenly decreases with increasing distance from the pinhole to 10^{-11} – $10^{-10} 1/\text{cm}^3$. Separation between the absorbers' coverage is larger closer to the edge of the LOS fan and to the edge of the inflated triangular domain. Profile and shape of the distinguishable LOS show that each characteristic feature of interest in this schematically indicated magnetic configuration is viewed by at least one detector each.

The right side image (**b**) similarly presents the etendues of the VBCm, clearly revealing the much stronger separation of the individual absorbers local sens-

itivity, even closer to the aperture. From its maximum of $2 \times 10^{-10}/\text{cm}^3$, an even reduction towards the pinhole opposite side of the domain along the LOS to 5×10^{-12} – $10^{-10}\text{ }1/\text{cm}^3$ is contrasted by gaps in coverage that are single - edge channels - to multiple pixels wide - center of the fan. Especially in-between the LOS that view around the magnetic axis, gaps are largest and extend the furthest towards the cameras' aperture. The much more spread construction of this artificial camera, combined with the smaller pinhole-detector distance compared to the HBCm, which is akin to that of the VBCl/r, yields a less wide LOS cone, as underlined by their presented separation. Furthermore, the close position of the array to the LCFS is highlighted by the void around and outside the separatrix and magnetic island on the upper inboard side where the maximum is located.

The designed two supplementary, artificial cameras *MIRh* and *VBCm* are constructed as similar as possible as the built, in-place counterparts. Hence, their etendues show no peculiarities, which was the goal for an improved global sensitivity and conclusive tomographic reconstruction. Application of said absorber arrays will be done further below during evaluation of various, complex phantom radiation distributions. The goal is to attain a perspective for a hypothetical extension of the multicamera bolometer system.

The evaluation of the bolometer LOS geometry in a context of tomographic inversion is thereby concluded for now. Comparison of different discrete segmentation methods and their impact on the three-dimensional, local sensitivity in a voxel grid based plasma tube has concluded that rectangular and triangulated approaches are equally valid and applicable for their respective task. Their corresponding fineness or resolution was also found to be sufficient above four individual parts of both detector and aperture, which yields a great reduction in computational tasks, though a general setting of $N = 8$ triangulated sub-detectors and -apertures has been established. Robustness of the crucial to a successful reconstruction, central geometric parameter matrix \mathbf{T} and perturbation thereof were examined thoroughly with the following hypothetical camera geometries. A variety of independent and combined changes to the original construction and their respective impact on the two-dimensional, local sensitivity distribution for tomography have been presented. This included chord brightness forward model integrations from fully symmetrical STRAHL radiation profiles using said results. Throughout this it was found that the orientation of the cameras

in the device introduces an intrinsic asymmetry to the LOS fans yield and hence their measurements. Beyond that, their individual deviation in local sensitivity generally is of order of magnitude found while comparing segmentation methods and is therefore assumed to be of lesser relevance. However, high precision measurements provided large discrepancies to the designed in-device aperture positions and the conclusive application to the previous models showed significant impact on the forward calculations. Therefore, one has to assume some level of additional, unknown, non-negligible error in \mathbf{T} , or more specifically to the regularisation functional \mathbf{K} when performing tomographic reconstructions. Finally, two entirely new cameras have been introduced, which now be used to improve the reconstruction of complex phantom radiation profiles and eventually gauge the efficacy of potential extensions to the existing multicamera system.

5.3. Phantom Radiation Profiles *Simulations*

~~Below~~ Tomographic reconstructions, particularly with badly conditioned ~~the number of LOS intersections~~ is significantly smaller than the number of free parameters or pixels/voxels. ~~detector systems~~ are difficult to perform and potentially yield a high level of uncertainty in the final result, subject to assumptions about the underlying geometry and errors in the measurement.

~~validation of Furthermore, improvements to the algorithm of already proven methods like the Minimum Fisher regularisation similar to the previously introduced radially dependent anisotropy and relative gradient smoothing weighting generally need tailoring for individual, characteristic radiation distributions, i.e. varying relative weights for smooth or localised emissivities. Practical evaluating of these algorithms with a selection of common and/or expected two-dimensional phantom radiation profiles is crucial towards successful reconstruction of experimental data. Insights from previous investigations will be used for advantage upon improving the tomography of said phantom images.~~

First, a set of tools will have to be introduced for evaluating the results and their grade properly. One trivial task is to find both the two-dimensional and integrated deviation between phantom and tomogram. A *mean square deviation (MSD)* is introduced as:

$$\vec{m}_{\text{var}} = \frac{\sqrt{(\vec{x} - \vec{x}_{\text{phan}})(\vec{x} - \vec{x}_{\text{phan}})^T}}{\|\vec{x}_{\text{phan}}\|} \cdot \vec{A}_p^T, \quad M_{\text{var}} = \|\vec{m}_{\text{var}}\|. \quad (5.14)$$

The above equation finds the relative, positive definite local deviation between the reconstruction and initial image $\vec{m}_{\text{var}} \in \mathbb{R}^m$, where $\vec{x}_{\text{phan}} \in \mathbb{R}^m$ is the radiation distribution of the phantom and $\vec{x} \in \mathbb{R}^m$ the resulting tomogram - remember that $m = N_\theta \cdot N_r$. The integrated *mean square deviation*, *MSD* is given by M_{var} , while \vec{A}_p is the area of the individual pixels $p^{(i,j)}$ associated with the radiation intensity in that location - for sake of simplicity let us write from here on

$$\vec{x}, \vec{A}_p \leftrightarrow x^{(i,j)} = x^{(i \cdot N_r + j)}, A_p^{(i,j)} = A_p^{(i \cdot N_r + j)}.$$

In order to find $A_p^{(i,j)}$ the *Heron^I formula* is used in equation (5.15) to separate the rectangular pixels into two triangles that fill the initial space and calculating their individual surface area. Let the pixel be:

$$p^{(i,j)} : \square(BCDE)^{(i,j)}.$$

The surface area $A_p^{(i,j)}$ of pixel $p^{(i,j)}$, constructed by the mesh intersection points $\{A, B, C, D\}$ is given by:

ARE

$$\begin{aligned} A_p^{(i,j)} &= A(\Delta(BCD)) + A(\Delta(CDE)), \\ a &= \underline{\overline{LM}}, \quad b = \underline{\overline{MN}}, \quad c = \underline{\overline{NL}}, \quad p = \frac{1}{2}(a+b+c), \\ A(\Delta(LMN)) &= \sqrt{p(p-a)(p-b)(p-c)}. \end{aligned} \quad (5.15)$$

Add a figure ...

The values of $A_p^{(i,j)}$ are calculated once for a parameter set of magnetic field configuration, voxel grid resolution $N_\varphi \times N_\theta \times N_r$ and camera geometry - remember that the two-dimensional representation of the grid like in figure 2.22 is achieved by finding the intersection of the camera LOS fan plane with the voxel mesh. This also makes it very easy to find the total, integrated radiation power of the phantom and tomogram:

$$P_{\text{rad},2D}(\vec{x}) = \vec{x}^T \cdot \vec{A}_p = \pi R_{\text{maj}} \sum_{j=0}^{n_r} \sum_{i=0}^{n_\theta} x^{(i \cdot n_r + j)} A_p^{(i,j)}. \quad (5.16)$$

^IHero of Alexandria (Hērōn hò Alexandreus) † 60 AD; Greek mathematician and engineer from Alexandria, Egypt during the Roman era

5.3. Phantom Radiation Profiles

Remember that R_{maj} is the major plasma radius, i.e. the distance between center of the machine and the magnetic axis at the center of the plasma. Finally, the regularisation *fitness* or *robustness factor* χ^2 - see equation (5.1) -, which measures how well input and output forward integrated profiles are in agreement, is re-introduced as:

calculated signals

$$\chi^2 = \frac{1}{N_{\text{ch}}} \|(\vec{b}_{\text{phan}} - \vec{b}_{\text{tom}}) \vec{\sigma}^{-1}\| . \quad (5.17)$$

standard

Remember that σ is the measurement uncertainty or deviation of each ~~individual~~ channel and N_{ch} the total number of channels. In practice, this is dictated by an error in ~~acquisition~~ *and calibration*, while for a forward phantom integration, an experimentally motivated and randomly distributed percentage between 1–2.5 % of the global maximum is applied. In this case, and for all following phantom reconstructions if not stated otherwise, the error is set to

$$\sigma^{(n)} = 0.025 \cdot \max(\vec{b}) \tilde{p}(n, \mathcal{N}(0, 0.5)) .$$

Here, $\tilde{p}(x, P)$ is a random sample for value x of a probability distribution P and $\mathcal{N}(\mu, \varepsilon)$ the *Gaussian normal distribution* of width ε and mean μ . With $\max(\vec{b})$ the global chord brightness peak, the error of channel n is at most 2.5 % of said value.

Equations 5.14 through 5.17 yield the necessary toolset to initially assess the quality of the phantom image reconstruction using the *Minimum Fisher regularisation tomography*. In the following pages, a comprehensive and diverse as possible set of hypothetical radiation distributions will be presented, alongside their individual tomographic reconstructions and corresponding errors, including both radial and chord brightness profiles from those, respectively. This exercise will be centred around experimentally motivated and more simplified and symmetric phantom images, from where more complex and challenging variations thereof are derived and reconstructed, while also trying to find an ideal - or suitable - set of anisotropy coefficients $\{k_{\text{core}}, k_{\text{edge}}\}$. This method will ultimately provide one with the practical limits of this approach for performing tomography on experimental data, which will be done so conclusively. If not stated otherwise, the employed voxel grid domain is $\{N_\varphi, N_\vartheta, N_r\} = \{30, 20, 150\}$ and in standard magnetic configuration.

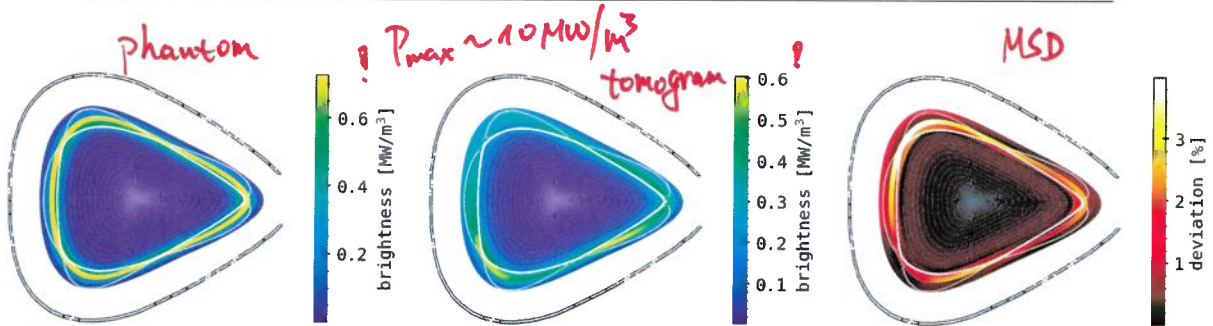


Figure 5.18.: Example of a (left) phantom radiation distribution and (center) its reconstruction using the Minimum Fisher tomography and stand ~~and~~ bolometer camera geometry, including the (right) relative local deviation between the two prior. The phantom image is constructed as a uniform ring along a fixed flux surface with radius r_a and a normal distributed intensity in radial direction with a maximum of 1 MW/m^3 and $\sigma = 0.25 \text{ m}$. The inversion domain is the magnetic standard configuration, as previously described in section 2.3.1. The ~~RDA parameters~~ were chosen as $k_{\text{core}} = 2$ and $k_{\text{edge}} = 0.5$ with no smoothing in-between.

5.3.1. Symmetrical Ring in Scrape-Off Layer

The first phantom radiation profile that is used for forward integration and reconstructed with the MFR algorithm is shown, alongside its tomogram and their respective mean deviation from equation (5.14) in figure 5.18. A bright ring with a radially normal distributed emissivity is constructed around a radius of $r_0 = r_a$ with a maximum of $P_{\text{phan},0} = 1 \text{ MW/m}^3$ and FWHM of $\sigma_r = 0.25r_a$. The latter two values are experimentally motivated and chosen to yield sensible P_{rad} from the chord brightness profiles and two-dimensional integrated powers.

$$P_{\text{phan}} = \frac{P_{\text{phan},0}}{2\pi\sigma^2} e^{-\frac{1}{2}\left(\frac{r-r_0}{\sigma}\right)^2}$$

$$r_a = 0.5 \text{ m} ; P_{\text{phan,max}} = \frac{32}{\pi} \sim 10 \text{ (MW/m}^3)$$

Individual values are and can only be attributed to discrete pixels on the grid. This is also due to the forward integration by $\mathbf{T}\vec{x}_{\text{phan}} = \vec{b}_{\text{ch}}$, where \vec{b}_{ch} is the chord brightness profile - also the measurement data in an experimental environment. The radius of a pixel is given by the radius of its rectangles $p^{(i,j)}$ barycentre. Hence, the actual maximum of the phantom emissivity is approximately 0.75 MW/m^3 since the pixel layer's center does not necessarily align with a particular radius, as given above. All plots also indicate, like

In

why do you choose
 $k_{\text{core}}=2$ and
 $k_{\text{edge}}=0.5$?

5.3. Phantom Radiation Profiles

~~are displayed with white lines.~~

before, a half-transparent schematic of the separatrix and magnetic island structure. The middle plot shows the Minimum Fisher regularisation reconstruction for $k_{\text{core}} = 2$ and $k_{\text{edge}} = 0.5$. In this case, the anisotropy profile is a simple plateau, i.e. a Heaviside¹ step function Θ_{N_T} for $N_T = 14$.

$$\Theta_g(x) = \begin{cases} 1 & , x > g \\ 0 & , \text{else} \end{cases} \quad ? \text{ What is } g$$

This particular set of coefficients was deliberately chosen to mimic a typical configuration that would be used for experimental data tomography, i.e. in order to favor smooth radiation profiles in the core and enable anisotropy beyond the LCFS. Radial location and absolute value of the emissivity in the tomogram are very similar to its counterpart, however the distribution thereof is very asymmetric and focused strongly around the lower middle and inboard side X-point. The reconstructed emissivity is also much smoother and radially spread more than in the phantom along the entire separatrix. Gradients in poloidal direction are increased while they are significantly reduced perpendicular to the LCFS. At the inboard upper magnetic island and around the neighbouring X-points, the tomogram's radiation density is nearly constant between separatrix and domain boundary, while in the phantom no emissions can be found in the very last pixel shell towards the edge. These observations are also very much reflected in the right side MSD plot in figure 5.18 - see equation (5.14). The larger the brightness or value of deviation here, the greater the discrepancy in that particular location of the mesh between phantom and tomogram emissivity distribution. Variations of 1–3 % are largely centred around the pixels closest to the LCFS and magnetic structures. They match best, as described above, at the lower inboard and center, as well as worst around the opposite side X-points of the triangular plane. The average deviation along the separatrix is 2–2.5 %. ?

In figure 5.19, the individual radial and forward integration profiles are shown. The left image presents both radial emissivity distributions, which are derived using

$$p_r = p_{r(j)} = \int_{2\pi} P_{\text{rad}}(r, \vartheta) d\vartheta \hat{=} \frac{1}{2\pi} \sum_{i=0}^{N_\vartheta} x^{(i,j)}, \quad \frac{\sum x \cdot A}{\sum A} \xrightarrow{\text{Pixel area}} \text{Wrong.}$$

¹Oliver Heaviside, FRS * May 18, 1850 † Feb. 3 1925; English self-taught mathematician and physicist, developed technique for solving differential equations, vector calculus independently and rewrote Maxwell's

Note : The grid areas are not equivalent.

To check:
 $d\theta$

Chapter 5. Two-dimensional radiation inversion

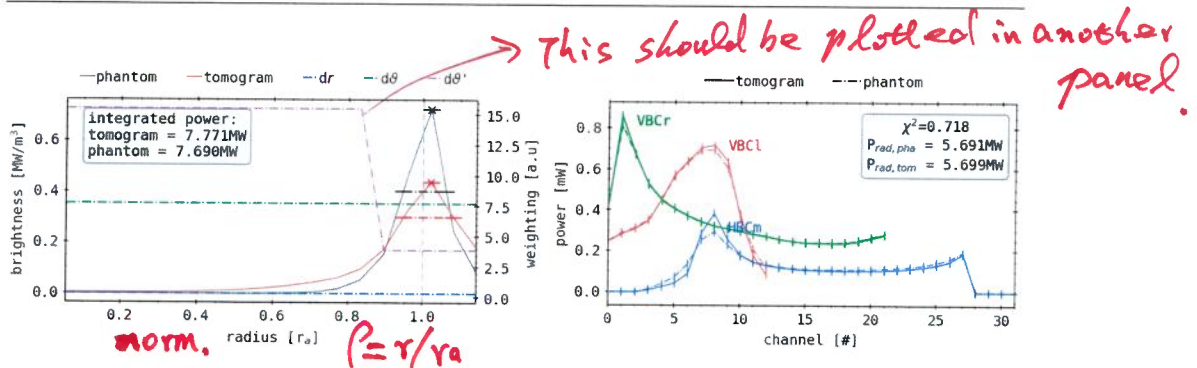


Figure 5.19.: Corresponding analysis for the results shown in figure 5.18. (left) Radial profile comparison between phantom and two-dimensional reconstruction, including the relative radial and poloidal weighting factor profiles dr and $d\theta$. Noted here are also the total integrated radiation powers for both. (right) Forward integrated chord brightness profiles of the individual arrays, using the ~~standard~~ camera geometry and the ~~standard~~ distributions from figure 5.18. The corresponding values for P_{rad} , as well as the fitness factor χ^2 are included.

where one remembers that $x^{(i,j)} = (\bar{x})^{(i,j)}$ is the phantom or tomogram radiation profile - later referred to as $p_r^{(phan)}$ and $p_r^{(tom)}$. Equation (5.18) essentially yields the average of concentric pixel shells between the magnetic axis and domain boundary. For the individual lines, local maxima positions and values are indicated with by a \times -marker and their corresponding peak FWHM by a dash-dotted line at that particular height and location. Included next to p_r in the same plot are also the corresponding radial and poloidal weighting factors of the regularisation functional, i.e. the first order local gradients with $d\theta' = k_{anis} \theta'$ the impact of the anisotropy factor. Two-dimensional integrated powers, calculated using equation (5.16) are noted for both distributions individually. The plot on the right side features both forward integration profiles for all three bolometer cameras in a simplified presentation - results are shown over their discrete channel numbers, rather than their LOS projected radii. This simply results from producing $\vec{b} = T\vec{x}$, hence this plots abscissa is in units of power, i.e. the absolute, total power to the absorber instead of brightness or radiation density. Corresponding errors per detector are indicated as vertical lines as well for the forward integrated profile. Included here as well are both radiation power losses $P_{rad,X}$ as measured by the bolometer cameras and introduced in equation (2.25)

One sentence is missing:

Figure 5.19 shows the results of 1D emissivity profile and the ...

Mistakes in eq.(5.11)

obtained using $\vec{b} = T\vec{x}$,

How is the error determined? 2% is given?

5.3. Phantom Radiation Profiles

, which are calculated based on equation (2.25),

and the corresponding fitness factors χ^2 are indicated.

Looking at the left ~~image~~ panel, a significant discrepancy between sharpness and absolute height of the radial profile peaks at r_a is immediately noticeable. The position of the maximum in both the phantom and tomogram line is slightly outside the separatrix, which is indicated by a grey dotted line. Height and width of the prior profiles peak are 0.73 MW/m^3 and 0.15 m respectively, while they are 0.45 MW/m^3 and 0.17 m for the latter. Conclusively, the $p_r^{(tom)}$ profile maximum extends far more in radial direction, though no emission can be found for either line for $<0.3 \text{ m}$ - the phantoms radial brightness vanishes inside 0.7 m . Integration of the two-dimensional emissivities using equation (5.16) yields 7.771 MW and 7.690 MW for the tomogram and phantom, which is equal to a 1.14% deviation. With a separate abscissa on the right, the regularisation weights are measured in the same plot. The radial gradient dr of 0.4 a.u. and standard poloidal factor $d\vartheta$ of 7.7 a.u. are both constant across the domain, since the underlying grid mesh was designed with constant step sizes. Modified by k_{an} the anisotropy factor, $d\vartheta'$ becomes a step from 15.4 a.u. at 0.85 m to 3.9 a.u. at 0.9 m . Despite the unfavourable weighting and discrepancy in absolute height and position, the radial profiles of tomogram and phantom generally and qualitatively match well, which is underlined by the negligibly small error in integrated power. Similar circumstances are true for the forward integration comparison on the right in figure 5.19. Both sets of camera profiles yield a P_{rad} within 0.4% of each other, while the fitness factor χ^2 is also close to its target value unity. However, besides the nearly identical and certainly congruent within the error bars $VBCl/r$ lines, the $HBCm$ shows noticeable disagreement between the tomogram and phantom. Particularly, if not exclusively, the lower side range of this array, i.e. channel three through ten deviate significantly, where the phantom's profile is again less sharp and lower in absolute height. Furthermore, for both profiles, the lower and upper part are distinctly different in shape and height, which has been extensively explored in the previous section about the underlying camera geometry, though this is still being amplified for the tomogram. The vertical cameras accumulate, with a few exceptions, globally the most radiation with 0.9 mW and 0.7 mW at peak for the left and right array respectively. Only at the peak of the $HBCm$ tomogram forward integral of 0.39 mW , the $VBCr$ plot is surpassed around channel eight, as well as the $VBCl$ towards its minimum at channel twelve. Overall, the characteristic of both two-dimensional radiation distributions

radial
interval
of the grid
center
 dr

$$P=1 (r=r_a)$$

Pay attention on
the unit.

$$P < 0.7$$

also show
unit?

*Why here not?**To Do: tuning the k_{ani} for a best match.*
(in 5.3.2)

is resembled by the structure of the individual and combined profiles, i.e. increased brightness at the separatrix, none outside and secondary emissivities at the core due to the cross domain geometry of the LOS.

This simple phantom and reconstruction for a common set of anisotropy factors show the intricacies and particularities that come with the Minimum Fisher regularisation of such experimentally motivated emissivity profiles. Experience from this exercise is used to familiarize one with the previously introduced set of algorithms and tools, while building a foundation for the following artificial radiation distributions and their tomograms. Especially evaluating and tuning the k_{ani} coefficients towards characteristics of the individual phantoms will be explored further in the following sections.

5.3.2. Anisotropic Scrape-Off Layer Ring Combinations

Based on the profile in figure 5.19, various ~~anisotropic~~ two-dimensional emissivities are constructed in order to examine ~~superimposed or convoluted~~ ~~poloidally symmetric and asymmetric distributions~~ and their reconstructions. Particularly the impact of different k_{ani} parameter sets on the tomograms quality will be of focus here, while this is still being considered from the perspective of experimental data tomographies.

SOL Ring and 0° Core Anisotropy

The first combination phantom is constructed from a bright ring at the SOL like before, i.e. a maximum of 1 MW/m^3 with a normal distributed decay in radial direction of $\sigma_r = 0.25r_a$ width, and an additional, inside the separatrix core structure of 150% intensity of the prior at $0.7r_a$ and poloidal asymmetry towards the inboard lower X-point - for reference, this will be called 0°-orientation in the following exploitations. This superimposed emissivity is derived by convoluting two normal distributions in radial and poloidal direction of different widths, i.e.

$$P_{\text{phan}}(r, \vartheta) = \frac{P_{\text{phan},0}}{2\pi\sigma_r^2} \left(e^{-\frac{1}{2}\left(\frac{r-r_a}{\sigma_r}\right)^2} + \frac{3}{4\pi\sigma_\vartheta^2} e^{-\frac{1}{2}\left(\frac{r-0.7r_a}{\sigma_r} + \frac{\vartheta-\vartheta_0}{\sigma_\vartheta}\right)^2} \right). \quad (5.19)$$

5.3. Phantom Radiation Profiles

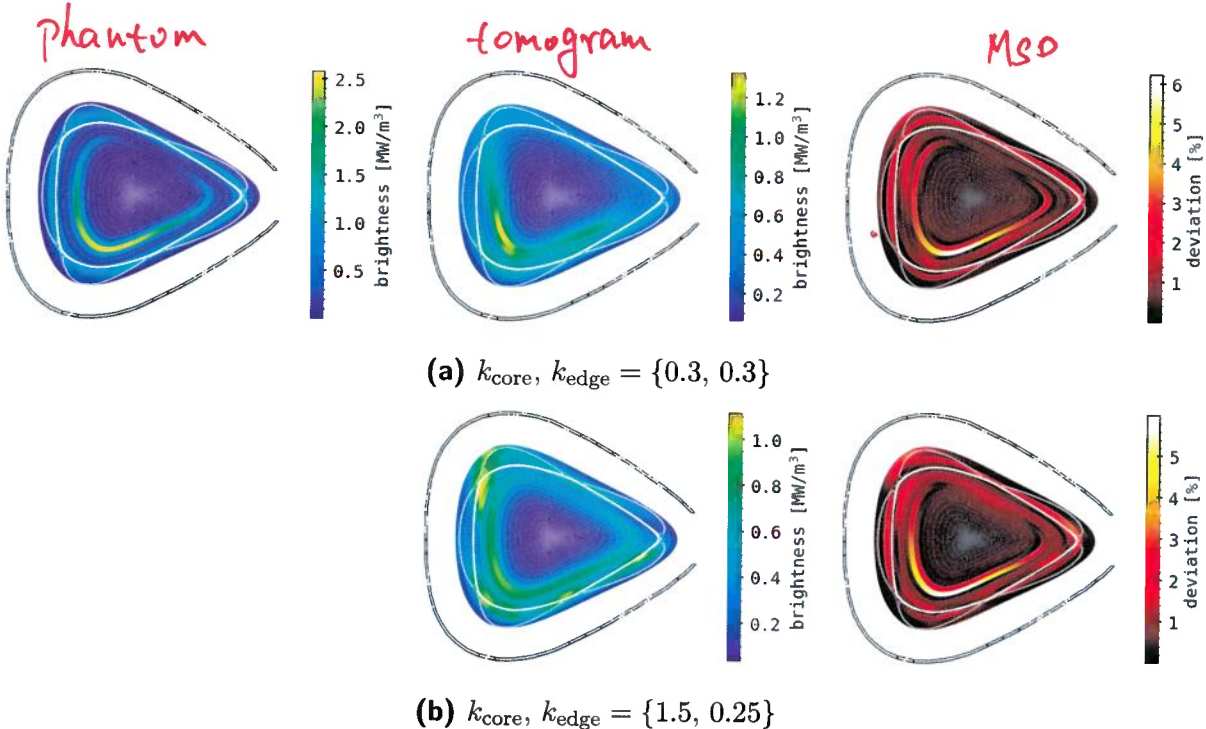


Figure 5.20.: Comparison of different RDA coefficient combinations for the same phantom radiation distribution (left), their reconstruction (center) and relative difference (right) using the Minimum Fisher tomography with standard bolometer camera geometry. The phantom image is constructed using a similarly bright ring around r_a as in figure 5.18, with a maximum intensity of 1 MW/m^3 , as well as an inside structure at $0.7r_a$ with a poloidally asymmetric maximum towards the lower side, close to the aperture of the VBC of 150% intensity of the prior. (a) A parameter combination preferring poloidal asymmetry equally in the core and edge. (b) RDA coefficients amplifying distinguishable structures in the edge and smooth radiation profiles in the core region. All distributions are plotted over the standard magnetic geometry mesh at 108° toroidally, as provided by section 2.3.1.

Here, the width in poloidal direction is $\sigma_\vartheta = 0.785 \text{ rad}$ or $\sim 15^\circ/\pi/4$ and $\vartheta_0 = 0^\circ$, the angle of the anisotropy - this particular orientation is chosen deliberately as a starting point from experience with previous ~~experimental data~~ reconstructions. The resulting phantom radiation distribution can be found in the top left of figure 5.20, accompanied by the reconstruc-

(those are
not experimental
data!)

Chapter 5. Two-dimensional radiation inversion

tions and two-dimensional error profiles for two sets of k_{ani} coefficients. In sum, the maximum emissivity becomes 2.55 MW/m^3 with visually clear separation between the two bright rings. The first set of anisotropy factors, again extrapolated using a Heaviside $\Theta_{14}(n)$ in the radial dimension, reads $k_{\text{core}}, k_{\text{edge}} = \{0.3, 0.3\}$ and the second $\{1., 5, 0.25\}$. *with*

emissivity For the set of images in (a), a parameter combination of $k_{\text{core}} = k_{\text{edge}} = 0.3$ equally supports and enables reconstruction of anisotropic structures in the core and outside the separatrix. The corresponding first reconstruction on the top features significantly lower emissions, about 45% of the input profile at 1.45 MW/m^3 . Structures and focus of the anisotropy are noticeably washed out and spread in both poloidal and radial direction. The maximum intensity inside the separatrix is also shifted clockwise and slightly outward towards the inboard magnetic island. That said, the most prominent difference between the phantom and tomogram is the interference or bleeding of the higher core emissivity with or into the homogenous, outside ring, which produces a global anisotropy in the reconstruction in contrast to the input distribution. Reflected in the MSD profile on the top right particularly is the poloidal shift of the inside asymmetry, since the largest error of 6.1% is found at that location in poloidally counter-clockwise direction. Along the LCFS, with the exception of the lower inboard X-point, a nearly constant deviation of $\sim 2\%$ is indicated. In-between the core and SOL structures, the radial bleeding of emissivities yields significant error values in the lower and inboard area of 2–3%. Despite the anisotropy coefficients setting, no additional asymmetries are produced in the tomogram due to the regularisation weights.

The second set of $k_{\text{ani}} = \{1.5, 0.25\}$ for plot combination (b) favours smooth and symmetrical emissions in the core and anisotropic profiles towards the edge. In fact, the corresponding reconstruction features significant poloidal asymmetries close to and outside the LCFS, particularly at and around the X-points. Most prominently, the global maximum of 1.21 MW/m^3 is found within a poloidally and radially extended anisotropy, reaching from inside the separatrix and upper inboard X-points to the edge of the respective magnetic island and domain boundary. Additional similar characteristics can be found at the original position from the phantom, as well as the respective lower X-points and along the outboard lower magnetic island. All show a significantly higher emissivity of $0.85\text{--}1 \text{ MW/m}^3$ compared to the in-between smoothed and spread out intensity of around 0.7 MW/m^3 . Con-

*Be
Concise.*

*Take a strong shot at!
Three pages (272-274)
for explanation of
figure 5.21.*

figure 5.21. Two sets of images show the results for the respective two k_{ani} parameter combinations from the previous plots in (a) and (b). For anisotropy factors $\{0.3, 0.3\}$, the poloidally average radial tomogram characteristic on the top left is again far smoother and features less pronounced local extremes than its phantom counterpart. Even at the innermost radii, the tomogram still yields non-negligible emissivities of at least 0.075 MW/m^3 and increases up until its first peak, which coincides with the location in the phantom, at $0.7r_a$. With 0.65 MW/m^3 , this maximum is less than half of the corresponding structure in the artificial distribution at 1.325 MW/m^3 , while no FWHM is produced for this shallow peak. The indicated width of the underlying emissivity *heap* between $0.6-1.15 \text{ m}$ is mismatched and of no concern for this comparison. The phantoms core ~~anisotropy~~ features a width of 0.15 m and is followed by a sharp decline to 0.2 MW/m^3 towards the separatrix, after which a second maximum close to 1 MW/m^3 around 1.05 m of the same width follows. In the reconstructed distribution, the intensity along the separatrix produces a second peak at 0.95 m of 0.65 MW/m^3 with a FWHM of around 0.15 m . Beyond, both phantom and tomogram radial profile decline to 0.12 MW/m^3 and 0.3 MW/m^3 , respectively at the boundary. Integration using equation (5.16) yields 20.871 MW and 20.149 MW for the reconstructed and artificial radiation distribution, which results in a deviation $\sim 3.5\%$. Due to the design of this first k_{ani} profile, ~~poloidal and radial regularisation weights $d\vartheta'$ and $d\varphi'$ are both flat across the domain at 2.4 a. u. and 0.35 a. u.~~ - $d\vartheta'$ is, as before, constant with 7.25 a. u., which is of no particular concern here or in any of the following weighted MFR tomographies. Looking at the bottom left image, which presents the same set of results for the corresponding second combination of anisotropy coefficients, similar characteristics can be found in the tomograms radial profile. Except for the modified poloidal regularisation weight and $p_r^{(\text{tom})}$, this plot is congruent to the one above. Emissions in the core are ~~still~~ present in the tomogram towards $r = 0$, though as low as 40 kW/m^3 . Two significantly smaller and less pronounced peaks, though of slightly larger absolute value than the previous, are again found close to their artificial counterparts. Inside the separatrix, the maximum yields 0.65 MW/m^3 at 0.78 m with the same width of 0.15 m . Following a shallow local minimum, the second structure is produced around 0.95 m with the same height and width as the one on the left. Its decay towards the domain boundary is similar and concludes also at 0.3 MW/m^3 . This profiles' integrated power of 21.361 MW corresponds to an $\rightarrow \text{MW unit!}$

* Using (a) - (d) labeling
the panels in the figure.

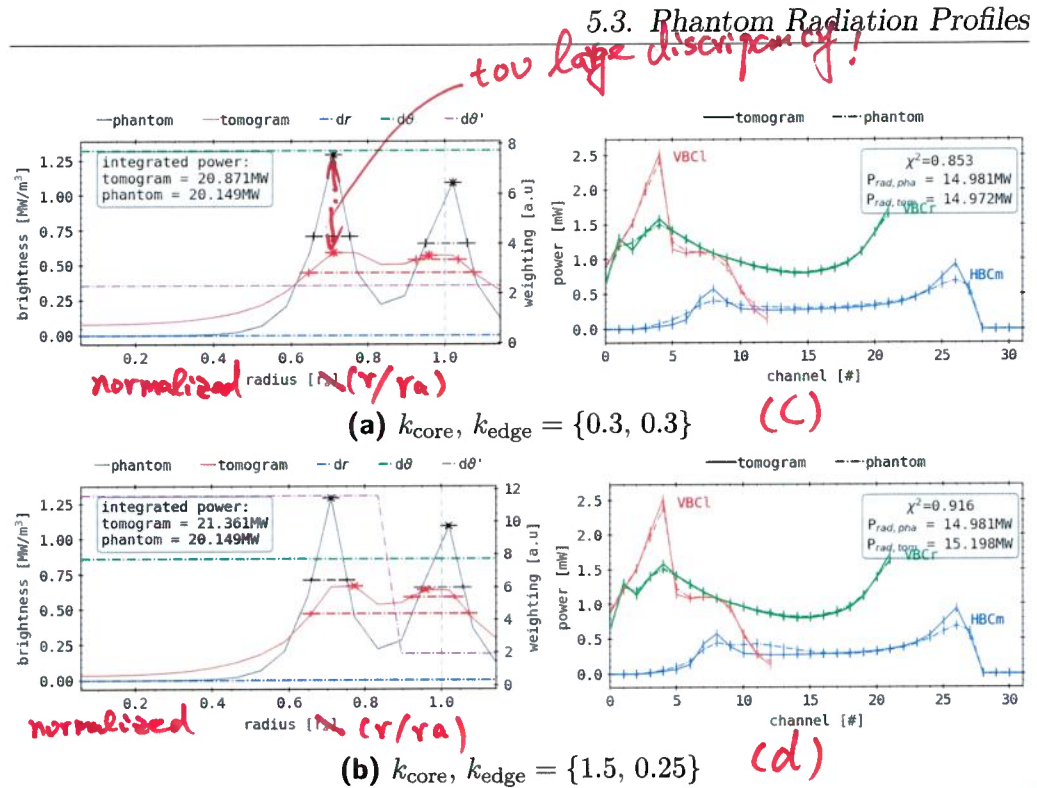


Figure 5.21.: Corresponding analysis for the results shown in figure 5.20.

The results are presented in the same way as in figure 5.19. (a) Parameter combination preferring poloidal asymmetry in the core and edge. (b) Coefficients amplifying distinguishable structures in the edge and smooth profiles in the core region.

It seems that χ^2 sensitivity
not sufficient.

Optimization
of $K_{\text{core}}, K_{\text{edge}}$
is not performed.

sistent with the previous tomogram, the anisotropic structure at the core is also present at that radius, however with no noticeable poloidal shift of its peak at 0.95 MW/m^3 like before and a smoother profile. Coincidentally, the MSD on the bottom right represents those additional asymmetries around the core and LCFS well, though their are partially indicated by local minima due to the superimposed bright ring in the phantom. The maximum error is found in the same location as before, in the core with 5.9 %. Beyond that, the deviation profile is largely similar if not equal to the one above, including the relative error along the separatrix and in-between the inside characteristic.

The corresponding radial, regularisation weight and forward integrated profiles for the two-dimensional distributions in figure 5.20 can be found in

5.3. Phantom Radiation Profiles

error of 5.6 %. A step in $d\psi'$ is result of the different anisotropy parameters, which happens down from 11.6 to 1.95 around 0.875 m between the radial characteristics.

On the right in figure 5.21, the forward integrated brightness profiles for each individual camera and both k_{ani} combinations are shown again in comparison between phantom and tomogram. The top image presents qualitatively, and for the VBC arrays also qualitatively well-matching artificial and reconstructed lines. Latter cameras plots are within their respective confidence interval and similarly larger in absolute terms like before. The VBCr forward integrals feature a smooth parabolic profile around the core, with the maximum of 1.7 mW in detector no. 21 that is the left most in this array, looking along the inside edge of the core, close to this particular anisotropy. On the other side, i.e. within the right-most channels towards the outboard side of the triangular plane, detectors zero through five show smaller local peaks around 1.3 mW towards the edge of the camera. From the perspective of the VBCl, the most radiation is acquired in both distributions by its first right-most five detectors up to 2.6 mW, i.e. those watching the core anisotropy across the separatrix. The bright ring along the LCFS produces a small second local maximum around channel eight following the very sharp drop from the preceding peak. Only the last, outermost absorbers looking outside the magnetic structures yield smaller integrated powers than the HBCm. That said, the horizontal camera also yields two very similar profiles, where in both plots the right half of the array, the LOS watching the lower side and poloidal anisotropy in this phantom reconstruction, respond to higher emissivities with up to 0.9 mW. Forward line integrals through the asymmetry and enclosing ring in combination produce that particularly broader peak. The slightly hollowed out core between channel no. 10-20 is limited by a second lesser local maximum of 0.6 mW around detector eight on the other side, corresponding to the upper part of the brightness along the separatrix. Beyond absorber no. three and 28 towards the edge of the camera array, no radiation is measured. As noted before in the radial and two-dimensional profiles (figure 5.20), the tomogram plots generally present slightly less pronounced local extremes and smoother transitions in-between, e.g. for the VBCl between channel no. 5-12. This set of forward integrals achieves a good quality of $\chi^2 = 0.853$, while the difference between the two respective P_{rad} of 14.981 MW/m³ and 14.972 MW/m³ for the phantom and tomogram is less than 0.01%. For the same artificial distribution profiles, the

NO. 22, 23 ...

, ch1-s,

Erad

{ radiated power P_{rad} in W (or MW)
 { emissivity E_{rad} in W/m³ or MW/m³
 * Pay attention on the parameter unit!

Figure cd)

bottom right image in figure 5.21 shows largely the same results. However, the congruence between the vertical camera plots is significantly improved, which is also reflected by $\chi^2 = 0.916$. In the tomograms HBCm profile, the channels that cover the upper ~~separatrix~~ - no. four through ten - show a minutely sharper peak compared to above, though with a continuously higher power towards the core around 0.4 mW, outside the confidence interval. Furthermore, the error between the extrapolated total radiation powers increases to 1.4% with $P_{\text{rad,tom}} = 15.198 \text{ MW}$.

Looking directly for differences between the two tomographic reconstructions in both two-dimensional and individual profiles, the second anisotropy coefficient set yields a distribution that features significantly more localised structures around and outside the separatrix and a less pronounced asymmetry or smoother emissivity in the core. In addition, or rather because of it, its absolute brightness is also lower, though the corresponding MSD profile shows a lesser total discrepancy between the tomogram and phantom. In the radially averaged profiles, contrary to the previous assessments, the latter finds both stronger local maxima at those respective radii and a higher total brightness outside $0.6r_a$. The bolometer camera forward integrals show only minor if not negligible differences, except for a protruding HBCm profile with higher power from the left maximum towards the center. Cross-correlating the fitness factor, the integral of the two-dimensional brightness distribution and radiation power from the forward calculated detector yield only supports the subjective impression of a qualitatively lesser reconstruction. However, the difference in χ^2 conflicts with that examination, i.e. a larger error between $P_{\text{rad,2D}}$ and P_{rad} seemingly does not contribute to a worse fit of input and output of the MFR.

(no. 10 LOS
goes through
the confined
region)

clarify the
definition of
 $P_{\text{rad,2D}}$

The comparison in figure 5.20 and 5.21, though individually presenting plausible, if not good reconstruction results, highlights a major problem with regularisation tomographies and particularly the anisotropically weighted MFR. The first set of $k_{\text{ani}} = \{0.3, 0.3\}$ is explicitly not well suited or intended to reconstruct this phantom radiation distribution adequately, however its corresponding tomogram subjectively resembles the input image very well. Most certainly, this does not say that this set of anisotropy coefficients yields the qualitatively and quantitatively best reconstruction results. Finding said ideal k_{ani} profile is a very difficult task and involves, including but not limited to, multidimensional algorithmic optimizations and incorporation of *a priori* knowledge and respective constraints. Underlined by the

How to improve the tomogram
quality?

chord-brightness

corresponding, close-to-unity fitness factor χ^2 and the congruence of the forward integrated camera profiles, the first set of results represents an accurate reconstruction. However, the second set of $\{1.5, 0.25\}$ produces a qualitative similarly matching tomogram, radial and individual camera profiles, while finding a subjectively far less adequate two-dimensional radiation distribution. One should note that, purely examining the impact of singular k_{core} and k_{edge} coefficients, the first tomogram does show improved localisation in the core compared to the second, which in fact yields a smoother characteristic there. Also, the significantly lesser edge factor actually amplifies anisotropies in that area. The second reconstructions χ^2 and MSD both indicate a better tomography result. In a scenario of experimental input data, the fitness coefficient is the only measure by which to examine the efficacy of the MFR. This again amplifies the importance of a well-rounded and thoroughly examined set of phantom image reconstructions with a focus on the relationship between quantitative and qualitative matching. Later series of MFR tomographies will focus on this particular aspect and evaluate the influence of and relationship between k_{ani} and χ^2 , $P_{\text{rad/2D}}$ etc.

For the

?

The definition ?

SOL Ring and 90° Core Anisotropy

The second set of phantom radiation distributions in figure 5.22 is derived using the same equation 5.19 as before and the same set of coefficients $P_{\text{phan},0}$ and $\sigma_{r/\vartheta}$, except for the poloidal mean $\vartheta_0 = 90^\circ$, i.e. the previous anisotropy shifted by $\pi/2$ in clockwise direction. All other parameters, including the anisotropy profile k_{ani} are kept constant. In the first reconstruction in the center of (a), compared to the previous tomogram for this set of coefficients, the inside anisotropy is of much brighter contrast and virtually merged with the outside separatrix ring around the inboard topside X-point and upper magnetic island, extending beyond to the domain boundary. The radial width of the core feature is also noticeably increased, while being less peaked and more plateau-shaped in radial direction. Very prominent is also the much stronger radiation at the inner radius $0.7r_a$ from the latter location down towards the opposite side island, where the previous asymmetry was centred around. The absolute height of the emissivity profile at its maximum is comparable to before with 1.18 MW/m^3 , though this intensity is spread much wider in poloidal direction. Towards the inboard lower X-point, the separation in brightness between LCFS and inside radiation increases again,

Do you mean

Fig. 5.22(a)

?

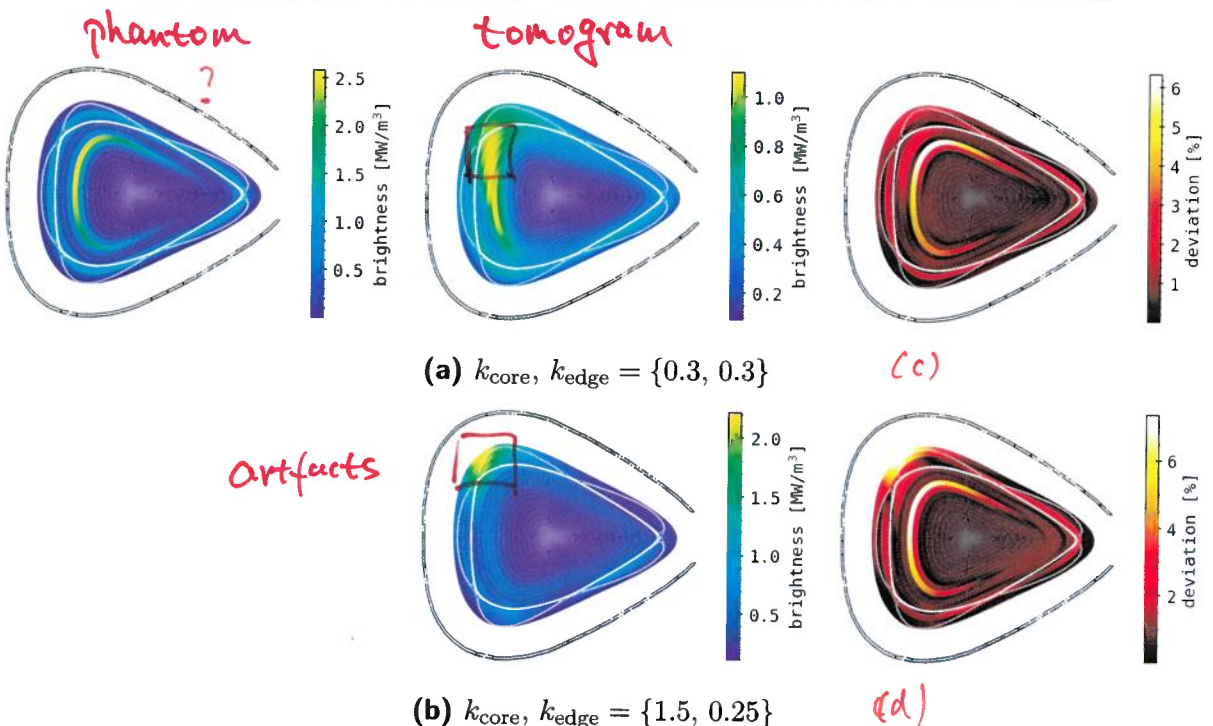


Figure 5.22.: (a), (b) Similarly constructed and reconstructed phantom radiation distribution as in figure 5.20, but the core structure has been rotated in clockwise direction by 90° . The tomographic inversion features the same RDA parameter combinations as before.

✓
show distortions of
the phantom

What is RDA ?

which along the prior yields $0.5\text{--}0.8 \text{ MW/m}^3$ at a significantly higher width of $\sim 0.5r_a$. Closer to the HRCm and top, no inside structure or increased emissivity is visible whatsoever. The corresponding MSD profile on the right therefore produces large errors of a maximum 6.2 % in $0.7r_a$ around the poloidal location of the input core anisotropy. Along this radius, larger deviations of $>4.5\%$ can be found in both directions for $\sim \pi/2$. A smoother and lower error profile of 2–3.5 % at and outside the separatrix correlates with the less sharp tomogram emissivity in that area.

The second set of anisotropy coefficients $\{1.5, 0.25\}$ in figure 5.22:(b) yields a fundamentally different reconstructed radiation profile, which essentially consists only of one bright spot outside the LCFS, at the edge of the inboard upper magnetic island neighbouring X-point towards the edge of the domain. Its brightness and therefore the global maximum emissivity of this

* It is 'norm. radius $P=r/r_a$ ' not radius
 * Using consistent radial location in the text.

5.3. Phantom Radiation Profiles

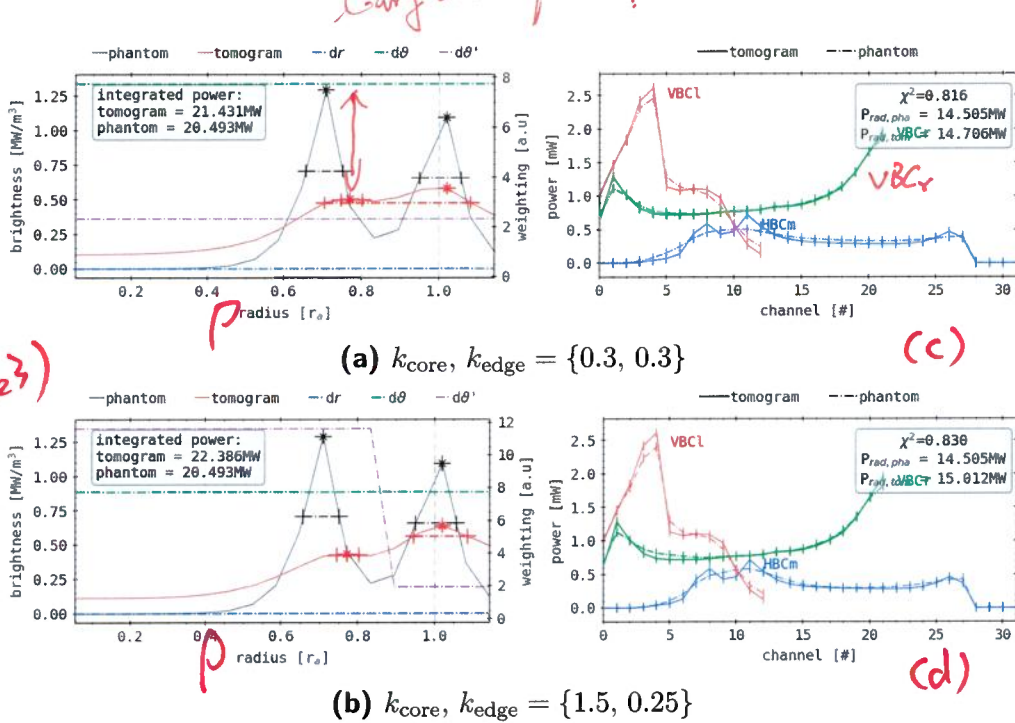


Figure 5.23.: (a), (b) Corresponding analysis for the results shown in figure 5.22, similar to figure 5.21, using the noted below anisotropy parameters for the tomographic inversion. The results are presented in the same way as in figure 5.19.

→ which channels view this 'hot-spot'?

tomogram is 2.2 MW/m^3 . In the core around $0.7r_a$, only a negligible amount of radiation $\leq 0.5 \text{ MW/m}^3$ of very constant and smooth distribution can be found. Slightly elevated emissivities compared to that are shown close to and inside the magnetic island along the separatrix. Correspondingly, the MSD profile on the right presents the largest discrepancies of $\sim 7.4\%$ in the location of the input poloidal anisotropy and reconstructed bright spot close to the edge of the inversion area. Directly comparing this image to the profile above, besides the latter characteristic and absolute values, the only difference is the error gap close to the core asymmetry, which is due to the drastically different localised features. *(not understandable)*

In accordance to the previous reconstruction for the 0° anisotropy, figure 5.23 again features the individual radial (average) profiles, alongside the different regularisation weights with total integrated radiation powers and the

? Core region
is quite smooth

* Using a table to list all your findings in various phantoms will be easier and clearer for ~~understanding~~ understanding

Chapter 5. Two-dimensional radiation inversion

~~change same~~

$$P = 1.02$$

* The

Wrong! You do
not change the
pixel geometry

respective forward integrated detector signals and their conclusive P_{rad} . In (a), following the corresponding results in the last set of images and figure 5.20, expectedly the same $p_{r,\text{phan}}$ is shown. The tomograms' counterpart presents less sharp local maxima that are also slightly shifted with respect to the initial plot. Leading from the center, the emissivity is similar to before at $<0.2 \text{ MW/m}^3$ until $0.5r_a$. The inside, almost unnoticeable peak at $0.76r_a$ is barely above 0.5 MW/m^3 and does not constitute the shape for properly measuring the FWHM, while the successive local minima is nearly at the same level. A conclusive second, largely flat or plateau-like peak around $1.02r_a$ at 0.6 MW/m^3 , with the same width as before, is still significantly below the input profiles maximum in that location. Obviously, the phantoms radial and all weighting parameter profiles are the same as in the first set of plots. The tomogram now yields 21.431 MW , corresponding to 4.4% deviation from the input. One should note here that $P_{\text{rad},2D}$ is ca. 0.3 MW higher than for an anisotropy at 0° indicating that the underlying mesh of pixels is not fully up-down symmetric, since this factor is the only variable in this comparison.

pattern is distorted!

On the right, the phantom forward integrated absorber powers are very similar to the initial results. The vertical cameras show qualitatively the same profiles, with an inboard maximum and peaks around the LCFS, since from their perspective the inside anisotropy isn't shifted much, which is reflected by the fact that the same channels find local and global maxima for both VBC1/r, i.e. in no. 1, 4, 8, 21. Values of said peaks are even equal within a tenth of a milliwatt. From the point of view of the horizontal camera HBCm however, the relative shape of the profile is flipped due to the asymmetry now aligning with the upper X-point. In contrast to before, a much broader and less sharp peak is found around channel no. 10 with 0.5 mW , corresponding to the line integration through outside ring and anisotropy, while there is no maximum in no. 26-28 and the power sharply falls to zero. Forward integration from the tomogram shows again slightly more pronounced characteristics, though being within the respective confidence interval throughout both vertical cameras. For the HBCm, core and lower side coverage, i.e. no. 15 and up, is also in similar agreement with the input. Channels viewing the upper part of the triangular plane present two individual peaks of $0.6-0.75 \text{ mW}$ around detector 9, which presents a small local minimum of 0.45 mW . Beyond, the measured power falls quicker than in the phantoms profile. From equation (2.25), $P_{\text{rad,phan}} = 14.505 \text{ MW}$

*
SMEAR-out
of the peak
happens.

For

5.3. Phantom Radiation Profiles

is 0.4 MW smaller than before and $P_{\text{rad,tom}} = 14.706 \text{ MW}$ therefore presents a 1.4 % error. The subjectively worse match between the forward profiles compared to the initial set of results is supported by a slightly worse fitness factor of 0.816 a. u.

Looking at the image on the left in figure 5.23:(b), again the same $p_{\text{,phantom}}$, regularisation weight profiles and integrated phantom radiation distribution power are shown. Presented results are achieved using the same input artificial emissivity and a different $k_{\text{ani}} = \{1.5, 0.25\}$. The tomograms poloidal average, akin to the one above for the other set of anisotropy coefficients, an increased brightness throughout the core until past $0.5r_a$ starting from 0.12 MW/m^3 can be found. The inside characteristic, which was barely noticeable in the two-dimensional image previously, yields a similarly shallow plateau at $0.75r_a$ of 0.45 MW/m^3 and therefore also significantly smaller than in the first profile for this set of parameters. Like before, there is no local minimum in-between this and the virtually merged into conclusive second, global maximum in $1.05r_a$ of 0.68 MW/m^3 with a width of 0.15 m. Integration of the emissivity distribution produces $P_{\text{rad,2D}} = 22.386 \text{ MW}$ or an 8.5 % larger total power than ~~the~~ the phantom. *with* *or $\Delta P = -0.15$?*

* *calculated*

The forward ~~integrated~~ detector signals on the right are largely very similar to the ones above. However, the vertical camera array results show increased discrepancies to the artificial brightness profiles, which are eventually beyond the confidence interval in locations of certain extrema, while the HBCm plot presents better overall agreement. In sum, a minimally improved fitness of $\chi^2 = 0.83$ ~~a.u.~~ compared to above contrasts a larger error in P_{rad} of 3.4 % by 15.012 MW. With respect to the first set of forward integrals, this is a much worse reconstruction measured by χ^2 and the deviation in extrapolated radiation powers.

The superimposed artificial radiation distribution in figure 5.22 has proven to be, given the same approach and *a priori* knowledge about the characteristics, qualitatively and quantitatively more difficult or *worse to be reconstructed*. On one hand, the two tomograms show very strong differences between each other in terms of absolute value and localised features that are far more pronounced than in figure 5.20. On the other hand, both are subjectively and measurably, as indicated by the MSD profiles, worse inversions from forward integrating the very similar phantom emissivity. Irrespective of the set of k_{ani} , a core anisotropy in this location is shown to be more complicated to reconstruct with this set of cameras and LOS.

significant radiation power towards the inboard upper area and boundary with $\sim 0.6 \text{ MW/m}^3$.

On the right, the MSD prominently shows this extension of the anisotropy towards the tip of the triangular plane, on the inside of the respective upper magnetic island, by an increased error value $\sim 3\%$ where there is close to no radiation in the phantom. Minor deviations $< 2.5\%$ can be found in the corresponding inboard location and beyond the respective two upper magnetic islands. The inconsistency of the separatrix ring intensity in comparison to the artificial distribution is highlighted here as well by alternating increased and decreased discrepancies of 1.5–2.5% along the poloidal direction. The largest error of 5.8% is again located where the input anisotropy is placed and only decreases significantly after a $\pi/2$ sweep in both directions.

Reconstruction and error profile in figure 5.24:(b) for a set of $k_{\text{ani}} = \{1.50, 2.5\}$ present a very similar image with respect to the previous series of plots in figure 5.22:(b), where there is a hyper localised bright spot of greatly larger intensity than the rest of the distribution and respective tomogram for comparison. In this case, the upper inboard magnetic island and part of the separatrix feature a relatively small $0.2 \times 0.2 \text{ m}$ characteristic with a maximum 1.85 MW/m^3 that shows a very sharp decay radially, while extending noticeably in poloidal direction. With respect to this brightness, the rest of the tomogram presents no other significant contributions to the overall radiation power. However, with $< 1 \text{ MW/m}^3$ some of the previously noted structures are found here as well, i.e. the variation in intensity along the LCFS, of which the very bright spot is a part, illuminated domain boundary at the inboard top and the core anisotropy.

The corresponding MSD profile yields a maximum deviation of 6.4% on the inside where the input feature is located in $0.7r_a$, similarly to the plot above. Compared to the latter, this error distribution overall shows noticeable variance 1–2% in the core and in-between the individual features, as was the case for the previous two examples of this particular phantom image. The prominence of the upper outboard magnetic island characteristic in the tomogram is reflected here also, as there is an increased error of $> 4\%$ at and around the separatrix in that location. Coincidentally, the MSD along the inside of the LCFS is reduced accordingly with respect to the prior profile. Figure 5.25 presents the one-dimensional profiles for the set of results shown in figure 5.24 like before. For both sets of images, the respective phantom radiation distribution profiles and plots are kept constant between them,

* Description of the discrepancy can be strongly shortened and combined with other phantoms.

5.3. Phantom Radiation Profiles

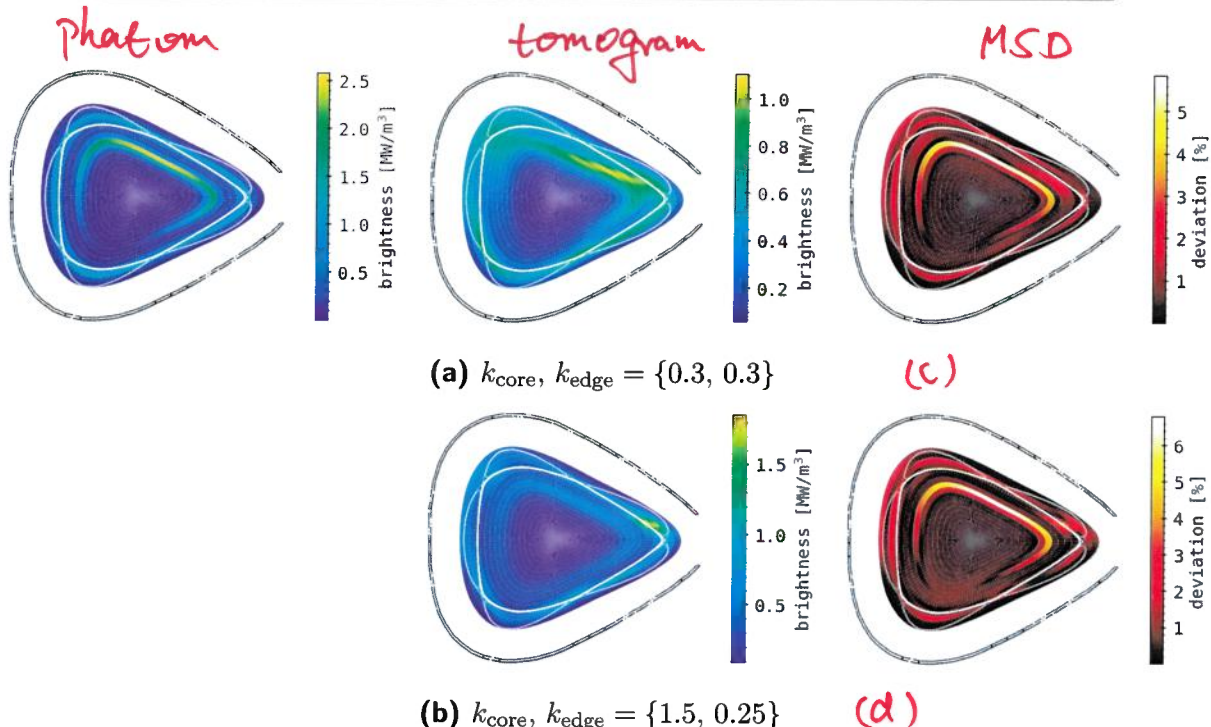


Figure 5.24.: (a), (b) Similarly constructed and reconstructed phantom radiation distribution as in figure 5.20, but the core structure has been rotated in clockwise direction by 180° . The tomographic inversion features the same RDA parameter combinations as before.

profile shows similar results to the corresponding tomogram in figure 5.20, where there is a distinctly brighter core structure at 1.1 MW/m^3 that is broadened towards the LCFS and a less intense ring around 0.7 MW/m^3 along the separatrix. The latter also features small local maxima of up to 0.9 MW/m^3 ~~in X-points and areas where magnetic islands intersect~~. Particular about this plot is the continued increased brightness, almost following a straight line from that localised inside feature to the outboard upper magnetic island. Conversely, the respective SOL intensity is higher here than in the rest of the triangular plane at 1 MW/m^3 . In the opposite direction, along an imaginary extension of that line, the separatrix ring and core anisotropy merge on the inboard side, interfering with the emissivity distribution in the SOL. Inside the LCFS, no brightness can be found adjacent to the examined structure. At the very edge of the tomographic domain, there is still

which X-point
?

~~Due to the shape and location of the inside asymmetry, the much closer and therefore crucial vertical camera detector are not able to adequately resolve the structure, while the line integration from the point-of-view of the HBC yield larger interference.~~ Contribution and impact of said anisotropy are lessened in this case by the increased distance and greater relative sensitivity to the symmetrical bright ring right in front of the pinhole. In fact, the same is true for the VBCI/r here, though with respect to the previous phantom distribution their LOS happen to be nearly perpendicular to the orientation of this core characteristic and hence only few, if not singular absorbers measure its emissivity. Thus, the detailed intensity profile and structure is largely lost, especially the explicit separation from the LCFS ring because of the unfavourable geometry. With respect to the applied anisotropy coefficients, the initial set enables the MFR to assume more of the particular inside brightness due to it providing a lower weight towards smooth, i.e. greater width profile characteristics. Though the spatial gap towards the separatrix is still lost because of the lack of local resolution, the second set essentially does the same while also only producing a ring of constant intensity inside the LCFS. This in turn then forces the algorithm to place $\sim 200\%$ of the above maximum emissivity in this location to in order to satisfy the original condition of $\min(1 - \chi^2) \approx 1$.

make a
shortcut!

The issues described above also serve as an example for one of the intrinsic limits of MFR tomographies with the multicamera bolometer system at W7-X. In addition to the fairly limited count of LOS for this kind of inversion problems - which is also motivation (see section 5.1) for the applied methodology - location and number of points of view of those cameras impose even more challenges to the reconstruction of such arbitrarily complex radiation distributions. This furthermore underlines the importance of phantom

~~image tomographies
for the bolometer~~

search for a proper tool

SOL Ring and 180° Core Anisotropy

The next logical continuation of the previous artificial radiation distributions is an additionally 90° shifted core anisotropy in combination with the ring of constant brightness around the separatrix. Again, this phantom in figure 5.24 is derived using equation 5.19 with $\vartheta_0 = 180^\circ$. All other parameters, including k_{ani} are also constant. In (a), the center image shows the tomographic reconstruction for a set of anisotropy coefficients $\{0.3, 0.3\}$. This

*
In Fig. 5.24
(a)

5.3. Phantom Radiation Profiles

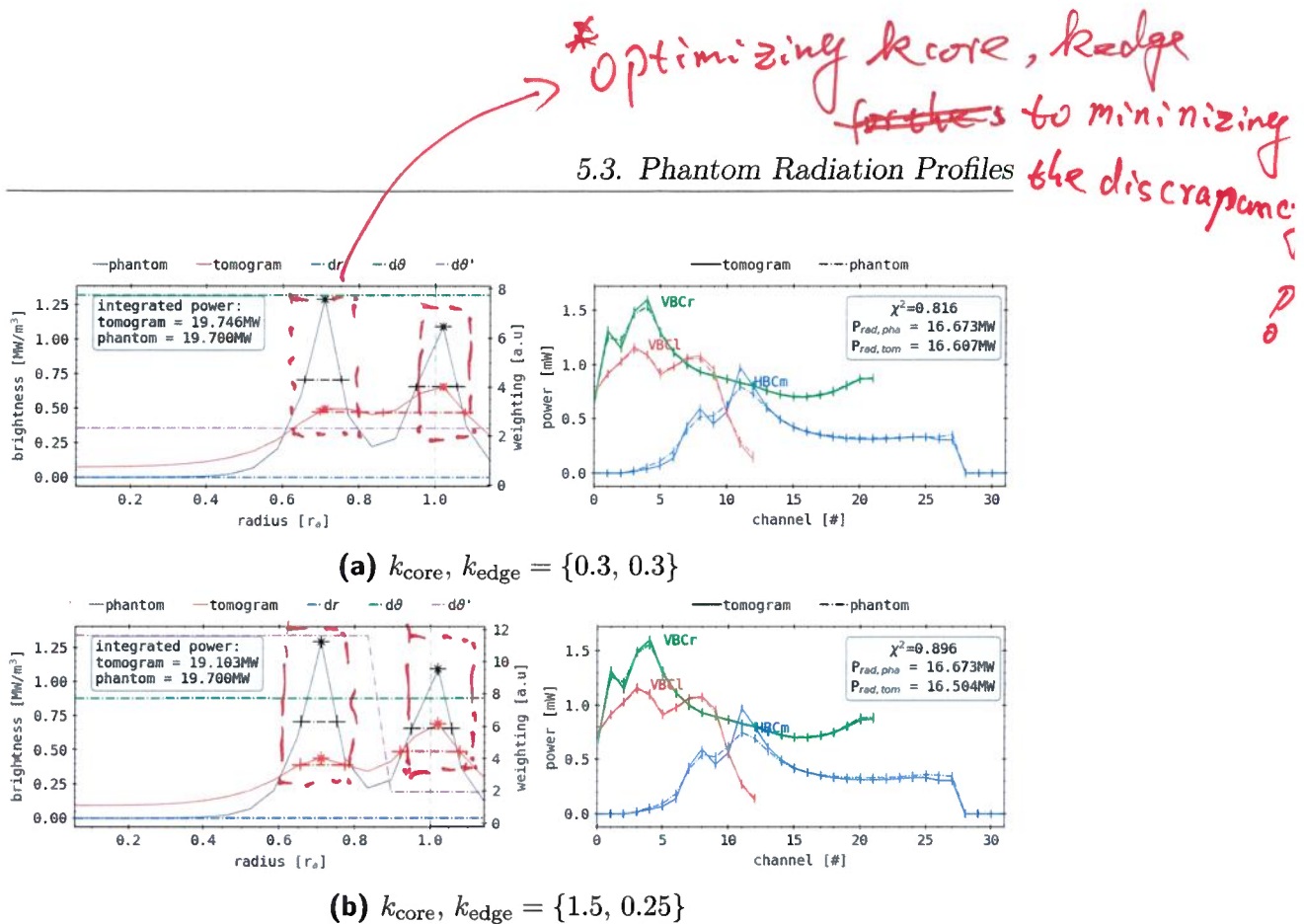


Figure 5.25.: (a), (b) Corresponding analysis for the results shown in figure 5.24, similar to figure 5.21, using the noted below anisotropy parameters for the tomographic inversion. The results are presented in the same way as in figure 5.19.

while the regularisation weights are the same as in the previous displays, i.e. figure 5.21. Also, the poloidally integrated radial profiles are congruent to those in the preceding plots. Two-dimensional integration of the emissivity finds a total power of 19.7 MW and the forward calculated brightness amounts to $P_{\text{rad},\text{phan}} = 16.673$ MW. On one hand, $P_{\text{rad},2D}$ is slightly smaller compared to the initial value by 2.3 %, while on the other the extrapolation from the detector powers is increased by 10.02 %. In (a), for $k_{\text{ani}} = \{0.3, 0.3\}$, the p_{rad} is akin to the one from the prior artificial radiation distribution, though with a slightly decreased intensity of 0.075 MW/m³ across the core and higher peak at 0.65 MW/m³ close to the separatrix in $1.05r_a$. The latter's width of 0.2 m is also larger with respect to the previous phantom, to which this profile's overall shape is still very similar. In total, the integration of the tomograms' emissivity produces $P_{\text{rad},2D} = 19.764$ MW, less than 0.3 %

*Make
a
shortcut!*

deviation from the input profiles absolute power.

On the right, the corresponding phantom and tomogram forward integrated absorber signals are shown, presenting a qualitatively and quantitatively different picture to the two other MFR reconstructions. Like before, in the input profile the HBC finds a large, stepped peak around channel no. ten starting from no. five and growing to 0.5 mW in no. eight and conclusively 0.75 mW in no. twelve, with a subsequent flat plateau across the core and sharp decline after detector no. 27. However, its relative intensity is far greater here due to the reduced power from the vertical camera channels. Those in particular show an entirely new picture, where the VBCr features also two successive local maxima in absorber no. two and four of 1.3–1.6 mW, viewing the outboard magnetic islands and tip of the triangular plane. Towards the center and other side of the cross-section, the profile declines with a closing minor increase to 0.85 mW where previously the maximum was found. This is continued by the VBCr core-side signals of channel null and following, also showing two distinct peaks around 1.1–1.15 mW in detector no. three and eight with a final pronounced drop in signal closest to the edge of the domain.

Forward integrated signals from the tomogram in (a) are overall well within the respective confidence interval for all cameras, except in detector no. eleven of the HBCm where there is a 0.2 mW greater achieved value here. In this location and for all other local extremes of any absorber array, the output results generally yield a more sharp and pronounced shape while transitions in the phantoms profiles are smoother and have smaller gradients. For the vertical cameras, both plots are congruent outside the latter locations. Summation and extrapolation of those results from the tomogram produces a total radiation power of $P_{\text{rad,tom}} = 16.607 \text{ MW}$, which less than 0.5 % of an error to the input distribution. Coincidentally, the fitness of $\chi^2 = 0.816 \text{ a. u.}$ is equal to that of the very first MFR tomography for the same set of anisotropy coefficients.

At the left in figure 5.25:(b), the reconstruction of the same phantom emissivity using $k_{\text{ani}} = \{1.5, 0.25\}$ finds a total power of $P_{\text{rad,2D}} = 19.103 \text{ MW}$, which is 3.3 % lower than in the input profile and latter reconstruction. The radial plot presents a slightly higher core brightness at 0.1 MW/m^3 compared to above, similar to that in figure 5.21:(b). While the inside peak of 0.45 MW/m^3 in the same location is smaller than before, it is noticeably more pronounced with a definite width of 0.1 m and a more distinct, follow-

5.3. Phantom Radiation Profiles

ing minimum. With 0.7 MW/m^3 and 0.15 m FWHM , though in the same radial location, the concluding maximum is higher and sharper than above as well as in the initial tomogram.

Forward integrated signals corresponding to this set of results are in stronger agreement with the respective input data. Exceptions are the global maximum in the HBCm plot in channel no. eleven, where the discrepancy remains constant, and the lower side and core part of the array, which show a minutely larger error. Particularly the vertical cameras match up significantly better than for the k_{ani} profile counterpart. Therefore, the fitness is increased to $\chi^2 = 0.896 \text{ a. u.}$. However, the extrapolated power loss of $P_{\text{rad,tom}} = 16.504 \text{ MW}$ yields a discrepancy of 0.7% and is hence both further away from the actual, i.e. integrated two-dimensional power and value of the artificial emissivity.

The varying k_{ani} MFR tomographies for the phantom radiation distribution in figure 5.24 effectively show similar results and discrepancies with respect to the previous plots. Superimposed and localised, anisotropic emissivities of this kind are again shown to require further analysis in order to achieve comparable or adequate tomograms when compared to figure 5.20. The first reconstruction, like the respective profile in the last set of images, in fact also yields a core anisotropy that is clearly distinguishable from the smoother and less intense bright ring around the LCFS. This is however similarly smeared out and merges with said ring in the location where the second tomogram finds a strong maximum. Finally, again one finds significant amounts of radiation outside the separatrix and magnetic islands towards the upper inboard side of the triangular plane. The balanced weighting coefficients enable the MFR to achieve both an inside asymmetry and brightness outside, however with the aforementioned drawbacks due to $k_{\text{core}}, k_{\text{edge}} < 1$, which prefers localisation above smoothness. In direct contrast and compared to the corresponding plot in the prior set of results, for an anisotropy profile of $k_{\text{ani}} = \{1.5, 0.25\}$, the second reconstruction is found to provide a distinctly worse fitting emissivity and a much more localised power deposition. This can be attributed to the increased distance to the VBC camera and therefore decreased LOS resolution in that particular area. Furthermore, from the perspective of the HBCm, this anisotropy is viewed by only a few, i.e. one to three LOS and hence the sensitivity of the whole system towards such structures is constructed very unfavourably. In combination with the respective coefficient profile, this enables the MFR algorithm to concen-

trate large amounts of power in this region, while also omitting the desired smoothness due to the otherwise even distribution of radiation, however at a much smaller level, in the core and along the separatrix. Taking into account the position of the asymmetry and the structure and geometry of the bolometer camera system, this generally agrees with the findings from the prior phantom reconstructions. Integrated powers from both two-dimensional and detector signal profiles also deviate again by varying amounts within this set of tomographies, and compared to the previous results. The congruence of the phantom radial plots among all artificial distributions though underlines the comparability of corresponding measures and deductions. Lastly, the relationship between $P_{\text{rad},2D}$ and P_{rad} between tomogram and phantom, as well as χ^2 is again inconsistent and thereby inconclusive, however this is in agreement with the last two phantom emissivity tomographies.

The work is repeated.

SOL Ring and 270° Core Anisotropy

The last phantom radiation distribution in this series of poloidally shifted core anisotropy reconstructions is, consequently, the same as before at an angle of $3/2\pi$, i.e. towards the outboard tip and lower side of the triangular plane. In figure 5.26, the artificial emissivity is produced using equation (5.19) with the same set of coefficients as for figure 5.26, except for $\vartheta_0 = 270^\circ$ or another $\pi/2$ shift of the poloidal location of the asymmetries peak in clockwise direction. As usual, all other parameter, including the two sets of k_{ani} are kept constant.

The localised maximum in the phantoms core in figure 5.26 is centred more towards the lower outboard magnetic island. In (a), the MFR finds the highest emissivity of 1.28 MW/m^3 in $0.7r_a$, closest to the lower edge of the latter island with a reduced poloidal expansion and sharper decay compared to the input data. This inside anisotropy is not distinctly separated from the emission that is placed along the separatrix and beyond. Significant radiation of $0.8\text{--}1.1 \text{ MW/m}^3$ can be found towards the opposite located magnetic island at the top and in the X-point on the lower inboard side, as well as the neighbouring X-points to the island closest to the anisotropy. With respect to the other tomograms of this k_{ani} profile, this one features a noticeable gap in the brightness distribution at the inboard top and center. Correspondingly, the MSD profile on the right reflects these characteristics with elevated error values of 2.5–3 %, particularly in and around the sep-

5.3. Phantom Radiation Profiles

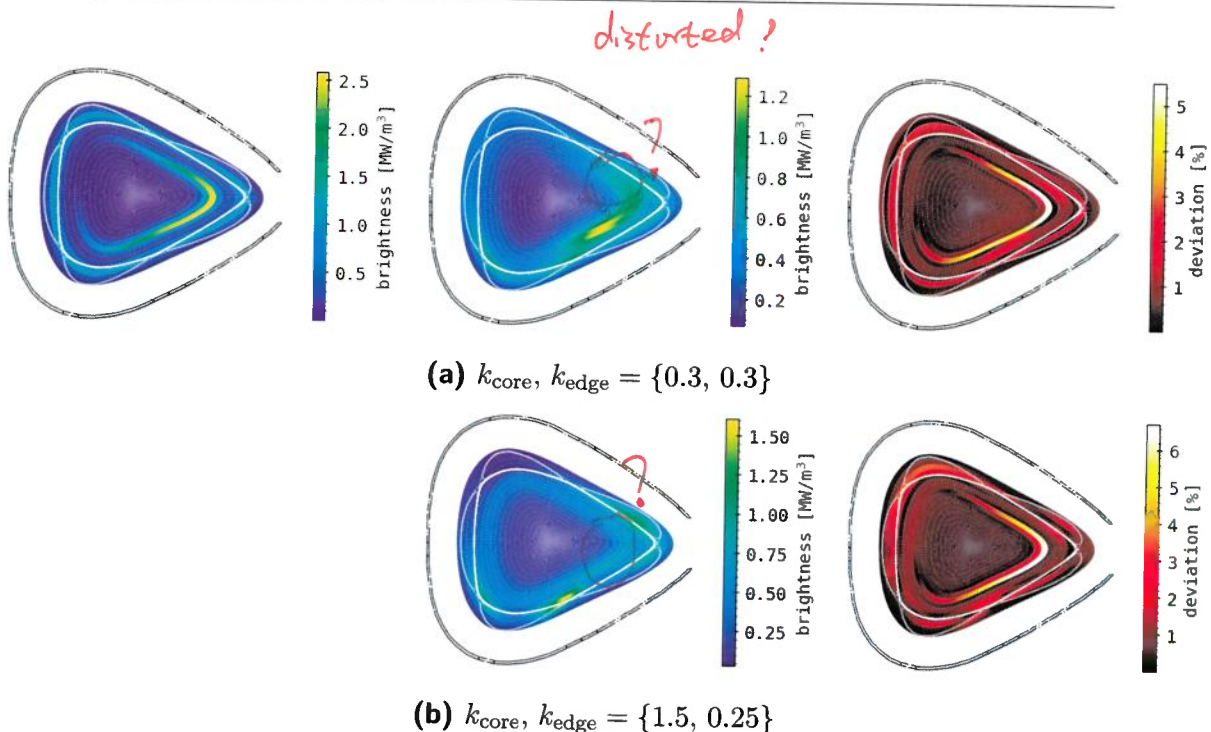


Figure 5.26.: (a), (b) Similarly constructed and reconstructed phantom radiation distribution as in figure 5.20, but the core structure has been rotated in clockwise direction by 270° . The tomographic inversion features the same RDA parameter combinations as before.

aratrix, except for the lower inboard X-point and outboard upper magnetic island. The global maximum is again located in the core where the input anisotropy is placed, i.e. around $\vartheta = 270^\circ$ with 5.5 % and large poloidal FWHM that spreads $\sim \pi/2$. In-between, smaller deviations around 2 % fill the area towards the tip of the triangular plane. Minor errors of 1.5 % are indicated in the radially outermost pixels on the inboard side from the discrepancy between the smeared out tomogram and sharp radial decay of the bright ring in the phantom.

In figure 5.26:(b), the second reconstruction for $k_{\text{ani}} = \{1.5, 0.25\}$ shows three distinctly localised bright spots of $>1 \text{ MW/m}^3$ in the inboard lower X-point, outboard upper magnetic island and lower central X-point with increasing intensity, wherein the latter is also the global maximum of 1.6 MW/m^3 . The prior all have a similar shape of increased poloidal elongation and sharp

radial decay in both directions. Between the individual structures, outside the LCFS at the tip of the triangular bolometer plane and especially towards and around the location of the input emissivity, i.e. $0.7r_a$, a smooth and nearly constant brightness of $\sim 0.6 \text{ MW/m}^3$. The outboard side of the emissivity is slightly, almost unnoticeably brighter than the left by a few kW/m^3 . Remaining areas in the tomogram are without emission.

On the right, the corresponding MSD profile shows the impact of the local maxima through strongly varying error values along the separatrix and in magnetic islands in the range of 1.5–3.5 %, particularly around the outboard side and aperture of the HBCm. The symmetrical bright ring around the core in the phantom, which is missing in the tomogram, is represented here by deviations $>3.5\%$ in $\sim 1.05r_a$. In the same location and with a similar shape and distribution as before, the global maximum is significantly larger at 6.35 %. In-between the two features of the input profile, the discrepancy is noticeably smaller here at $\leq 2\%$.

The final set of line plots in this series of phantom radiation profiles, which corresponds to the previous combination of tomograms and MSD distributions in figure 5.26, can be found in figure 5.27. Regularisation weights, as well as phantom profiles are the same as before, while the latter are, obviously, also constant between the two rows (a) and (b). Integration of the artificial, two-dimensional distribution yields $P_{\text{rad},2D} = 19.357 \text{ MW}$ and extrapolation from the similarly congruent within this comparison forward measurement results finds $P_{\text{rad}} = 17.150 \text{ MW}$. Again, both are distinctly different to the previous values of radiation power, i.e. the latter is $>1 \text{ MW}$ or 14.5 % larger and the prior $\sim 0.85 \text{ MW}$ or 4 % smaller than for the initial phantom image. With respect to the last artificial distribution, this is also true, though to a lesser extent.

In (a), a slightly increased core brightness of 0.12 MW/m^3 is followed by an equally positioned and peaked inside local maximum of 0.52 MW/m^3 with a width of 0.1 m. A minor valley and, this time located on the inside of the separatrix, second maximum at $0.95r_a$ of 0.56 MW/m^3 and similar width conclude this radial tomogram profile at 0.3 MW/m^3 at the boundary. Integration of the corresponding two-dimensional image finds a radiation power of 19.517 MW or $<1\%$ more than in its phantom.

On the right, the phantoms forward integrated detector signals yield significantly higher powers at a maximum 2.5 mW in channel no. four of the VBCr, ca. 1 mW more than before. The relative intensity of the remaining

5.3. Phantom Radiation Profiles

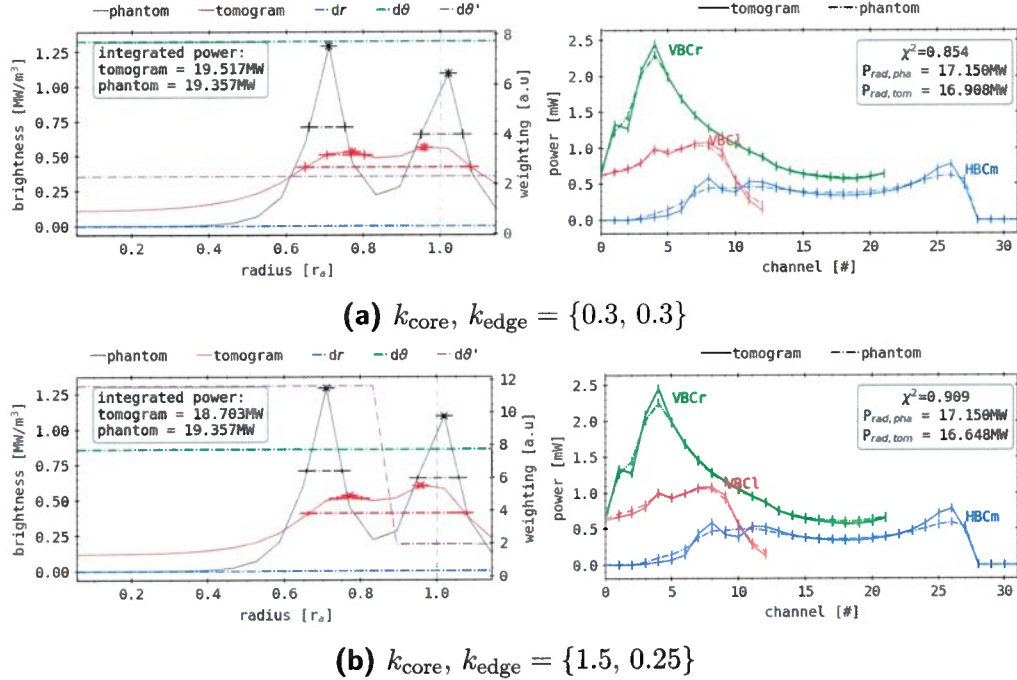


Figure 5.27.: (a), (b) Corresponding analysis for the results shown in figure 5.26, similar to figure 5.21, using the noted below anisotropy parameters for the tomographic inversion. The results are presented in the same way as in figure 5.19.

measurements is therefore decreased, though their total values do not differ as much. Left and right vertical camera arrays provide a respectively strong maximum towards the outboard side through VBCr detectors no. three to seven, a parabolic decay and comparatively weak core of <0.75 mW and a smoother second peak on the inboard side around 1 mW in absorber no. six to nine of the VBCl. The horizontal camera finds its maximum and the connected sharp decay on the lower side or between channel no. 24 and 28 at around 0.6 mW. Core and minor opposite side peak in this array are within 0.15 mW, while the upper part drop is smooth beyond detector no. 3. This weighting coefficient combinations tomogram profile is, again, generally within the respective error bars and therefore confidence interval, except for in locations of phantom plot extremes. In the VBCr plot, the outboard edge of the structure features an additional minor peak at 1.35 mW in channel

no. one. Coincidentally, the VBCl also shows a second, small bump in detector no. 4 within the profile of this arrays' measured local extremum. The horizontal cameras lower side maximum is larger here at 0.85 mW, whereas the other half of the array shows the already previously seen, connected two peaks and minima around 0.5 mW between absorber no. six and 13. In summary, this produces a fitness of $\chi^2 = 0.854$ a. u., which is the highest value among all $k_{\text{ani}} = \{0.3, 0.3\}$ reconstructions.

In (b), the radial profile is very similar to that on the top and akin to that in the first set of images corresponding to this weighting coefficient combination in figure 5.21. Core and inside peak portion of this plot show the same values and shapes with negligible variations in the absolute height of the local maximum. Localised towards the separatrix around $0.95r_a$ is the second peak at a slightly increased 0.63 MW/m^3 and of same width. Integration of the two-dimensional distribution yields $P_{\text{rad},2D} = 18.703 \text{ MW}$, significantly less than from the phantom at $>0.5 \text{ MW}$ or 3.4 %, particularly when compared to the above results.

Lastly, the forward integral detector signals on the right show comparable congruence to the phantoms results like before. Overall shape and absolute values are largely consistent to before and change only minutely. In parts, the local extremes are less pronounced, i.e. smaller or closer to the cameras phantom profile, as in the HBCm separatrix viewing absorbers no. six through twelve. However, some indicate larger discrepancies, like on the other side of the array between channel no. 23 and 27, or VBCr no. two and five. The range viewing the plasma core shows similar or better agreement between the input and output forward integrated data. Extrapolation of the respective signals finds $P_{\text{rad}} = 16.648 \text{ MW}$, now also smaller by 3 % than its correspondent from the artificial profiles. This ultimately produces a fitness of $\chi^2 = 0.909$ a. u., which is the overall and within the results of this particular set of k_{ani} second-highest matching quality, closely behind the first phantom reconstruction, where the core anisotropy was closest to the VBC detector arrays.

With respect to the two-dimensional results in figure 5.26, the shown tomograms are more akin in their reconstructive quality of the input radiation distributions to the initial set of images for $\vartheta_0 = 0^\circ$ than the two remaining MFR tomographies. Hence, not only is the perceived fitness of both tomograms greater than for the last reconstruction, but all measurements are in agreement with this evaluation. Still, though pointed out before already, the

290

*Shorten this part.
Keep ~~one~~ one example.*

*# 56 Page for ~~each~~ early phantom with
similar non-satisfactory result!
~~6 Page X 5 = 30 Pages~~*

5.3. Phantom Radiation Profiles

development of χ^2 etc. and the subjectively worse match between phantom and tomogram for $k_{\text{ani}} = \{1.5, 0.25\}$ do not align here as well. Beyond that, both anisotropy coefficient profiles again yield, quantitatively, entirely different radiation distributions, while the first combination produces a more adequate result compared to the latter. Comparing with the other artificial radiation distribution tomographies, one can also find similar levels of diffusion of emissivity across the triangular plane on both images here. However, localisation and structural quality of maximum intensity regions are, at least in the case of figure 5.26:(a), significantly improved. Analogue trends to before of increased edge anisotropy and decreased, smoother emissivity in the core can also be found in this second reconstruction. Similar patterns, with respect to their relation within the benchmark of this type of phantom, can be noticed in the linear profiles and forward integrated detector signals in figure 5.27. Though the ratio of both total radiation power extrapolations within this set of tomographies is congruent, the evolution of χ^2 and MSD profile or maximum is not, which previously was also the case. Additionally, the presented MFR have provided yet another noticeably different sample of measurements, i.e. P_{rad} etc. for a (nearly) constant artificial input distribution. In conclusion, the sensitivity of the multicamera system towards this orientation of core asymmetries is akin to that of the first one. Local resolution and LOS coverage are improved in this area, near to the pinhole of the HBCm, as they also are closer to the VBC cameras aperture.

In summary, this exploration of superimposed, anisotropic phantom radiation images has provided significant insight into the efficacy and performance of the established ~~RDA~~ MFR tomography algorithm. Of particular interest and relevance to later examinations of more complex artificial distributions is the gained experience about local sensitivity and its entanglement with the employed k_{ani} profiles. Especially important towards the tomography of experimental measurement data is the knowledge that explicitly opposite to the multiple camera apertures located structures or characteristics in the input distribution are more difficult to reconstruct and potentially yield quantitatively and qualitatively drastically different results for varying weighting coefficients. From the presented images and numbers it can be deduced that the congruence between ~~input radiation profile~~ and tomogram is primarily dependent on the distance of the emissivity and hence the local resolution and LOS coverage in that location. Fitness factor χ^2 ,
of the LOS

RDA =

phantom

Chapter 5. Two-dimensional radiation inversion

determined by a

P_{rad, 2D}

as well as a comparison between the integrated, two-dimensional radiation power and P_{rad} from the individual detector signals are not necessarily indicative of a good reconstruction, even across multiple k_{ani} combinations for the same set of input data. All the tomographies have in common that the pronunciation and absolute brightness, i.e. the sharpness of the particular localised features, of the artificial distribution is not entirely reproduced and the level of radiation is significantly reduced overall, though depending on the configuration relative trends are preserved to some extent. The selection of anisotropy parameters and their profile shape have also shown that, given the stark contrast in tomogram structures across the phantom variations, for $k_{\text{core}} > 1 > k_{\text{edge}}$ explicit anisotropic characteristics are lost and translated into the SOL. Here they are, for the given set of input profiles, mostly found in areas of increased LOS density - e.g. X-points and magnetic islands share areas of larger ϵ . This simultaneously also enforces smoother emissivity or less poloidal gradients in the core. Furthermore, at $1 > k_{\text{core}} = k_{\text{edge}}$, the inversion from LOS data of said properties is enabled in their original localisation, though with varying detail and width. Features of ~~larger connection lengths~~ or smooth and symmetrical emissions are not reproduced using such coefficients. Besides the two first tomographies in figure 5.20, i.e. for both k_{ani} profiles, the strong separation in the phantom between outside ring and core anisotropy is lost in the reconstruction. In case of (a), the radial width of both is increased and hence they partially merge in locations of higher intensity, while anywhere else it is decreased. With (b), except for the aforementioned localised peaks, core and SOL emissivity are largely the same and, if any, only show small minor gaps around the separatrix. This again supports the assumption of, on the one hand, unfavourable radiation distributions with respect to their structure corresponding to the bolometer camera system and, on the other, the need for specific, tailored regularisation weights for individual input data.

Employing the so far gained experience from the previous phantom emissivity tomographies, one will now continue to explore the weighting method and anisotropy coefficient space using established artificial input profiles, before extending the latter data space with more variations of complex, experimentally motivated structures. *phantom to*

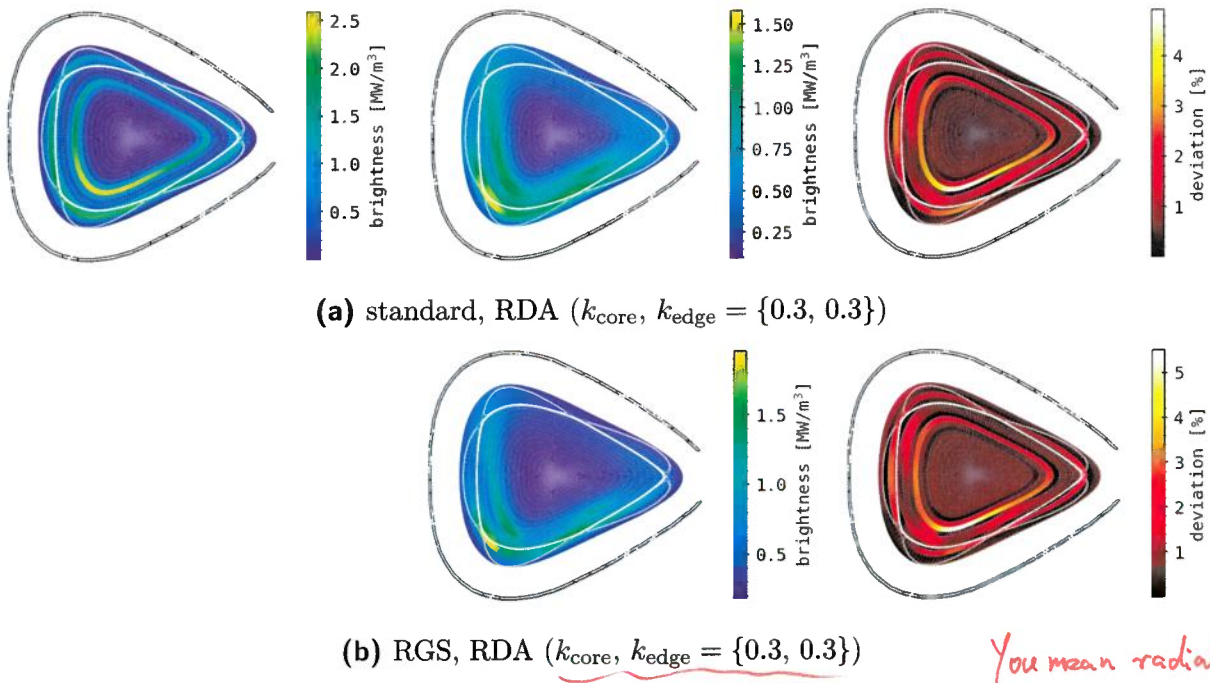


Figure 5.28.: Comparison between different reconstruction weighting methods, RDA and RGS, on the same phantom radiation distribution, using the same weighing coefficients and tomography parameters as well as camera geometries. The phantom image is constructed similarly to figure 5.20, while the outside ring at r_a is also adjusted to be poloidally asymmetric, with its maximum at the same position as the inner structure. (a) Standard Minimum Fisher information reconstruction with RDA. (b) Relative gradient smoothing, using the same RDA tomography parameters.

You mean radially dependent anisotropy!

but it's constant !!

RDA vs. RGS

Before moving on, the first phantom radiation distribution will be revisited to examine the differences between *radially dependent anisotropy* and *relative gradient smoothing* (RGS) regularisation methods when applied in a similar way. Both have been introduced in section 5.1.1 and section 5.1.2, while the prior has been employed extensively during the previous section. In order to adequately compare these results with one another, the same k_{ani} coefficients will be used with the RGS. One should keep in mind that this approach builds upon the RDA weighting of a given set of parameters.

shown in Figure 5.20

! You can start this section directly after showing Fig. 5.22 . Page 275(lower Part) → Page 292 are not necessary. 293

In figure 5.28, the input phantom, resulting tomograms and MSD profiles for the two methods are shown. The artificial radiation distribution is based on the first superposition in figure 5.20, with a bright ring at r_a and a core anisotropy in $0.7r_a$, however with the change of similarly asymmetric intensity profiles in poloidal direction. The inside profile has a maximum of 2.5 MW/m^3 , while the one on the outside only 50% of that. Both of the structures feature the same orientation around $\vartheta_0 = 0^\circ$ - same definition as before -, a poloidal and radial width of $\sigma_r = 0.25r_a$ and $\sigma_\vartheta = \pi/4$, which gives

$$P_{\text{phan}}(r, \vartheta) = \frac{P_{\text{phan},0}}{(2\pi\sigma_r\sigma_\vartheta)^2} \left(\frac{1}{2} e^{-\frac{1}{2}\left(\frac{r-r_a}{\sigma_r}\right)^2} + e^{-\frac{1}{2}\left(\frac{r-0.7r_a}{\sigma_r}\right)^2} \right) e^{-\frac{1}{2}\left(\frac{\vartheta-\vartheta_0}{\sigma_\vartheta}\right)^2}.$$

The resulting phantom image is, as expected, largely an extension of the initially proposed core asymmetry at a higher intensity. For a constant k_{ani} profile of $\{0.3, 0.3\}$, the MFR tomography using just the RDA in (a) adequately reconstructs the two individual, radially separated emissivities, though with a significantly increased width in both polar directions. Immediately noticeable is the switched prominence of the two, where the outside is now the brighter structure with a maximum of 1.6 MW/m^3 and the inside is reduced to 1.25 MW/m^3 . An additional, much smaller secondary maximum can be found along the separatrix in the lower, central X-point of $\sim 1.35 \text{ MW/m}^3$. The greatly decreased separation between those extremes is lost towards the inboard top side and tip of the triangular plane, as well as opposite of the input anisotropy, where the relative intensity is also much more reduced compared to the phantom.

Its corresponding MSD profile therefore measures discrepancies $> 1.5\%$ along the separatrix all around the cross-section, in-between the position of the core and SOL structure. Also, the maximum error of 4.9% is found at $0.7r_a$ towards 0° orientation due to the inversion of relative amplitude. All around at the LCFS and magnetic islands, the outside asymmetry produces variations of $1.8\text{--}3.2\%$, with particularly larger values in the location of the secondary maximum and in the inboard lower and central island. Minor error values can be noted at the very edge of the domain and inside the core feature $< 1.5\%$.

At the bottom in figure 5.28(b), a RGS weighted MFR reconstruction for the same RDA k_{ani} coefficients finds a similar, however quantitatively distinctly different radiation distribution where local extremes are distributed

?

5.3. Phantom Radiation Profiles

the same locally, though with significantly higher individual brightness. The global maximum at the lower inboard X-point is now at 1.95 MW/m^3 with a greatly reduced radial FWHM, while the inside anisotropy is mostly consistent with the above descriptions for a higher maximum intensity around 1.5 MW/m^3 . At the lower central X-point, the relative prominence of the previously found localisation is slightly reduced here at 1.6 MW/m^3 . The overall brightness in and around the remaining separatrix area and SOL is decreased due to the higher focus on the aforementioned extremes.

The respective MSD profile on the right hence shows smaller error values in the lower inboard location, though it finds higher discrepancies in the core of up to 5.5 % around $0.7r_a$ where the input inside asymmetry is located. Due to the otherwise strong qualitative congruence between the two tomograms, the second deviation plot is adequately described by the first one above.

Like before, figure 5.29 shows the corresponding one-dimensional radial and weighting, as well as forward integrated detector signal profiles of the above phantom and tomogram radiation images. All weighting coefficient profiles are at their usual level and are flat like before for $k_{\text{ani}} = \{0.3, 0.3\}$. Looking at the artificial distributions radial average plot, two similarly shaped peaks with a valley at 0.4 MW/m^3 can be found in $0.7r_a$ and $1.05r_a$, in descending order of 1.8 MW/m^3 and 1.45 MW/m^3 . Their FWHM differs minutely with $0.2r_a$ and $0.13r_a$ from inside to out. The inner core is dark up until $0.4r_a$, while at the edge of the domain one still measures 0.3 MW/m^3 . Integration of the two-dimensional emissivity distribution produces $P_{\text{rad},2D} = 26.921 \text{ MW}$ - significantly more than from any of the similar previous superpositions.

The detector signals on the right for the phantom radiation profile are also much higher compared to before. Both vertical cameras measure $>2 \text{ mW}$ and the global maximum in channel no. four of the VBCl finds 3.05 mW , corresponding on the lower inboard side with the brighter core anisotropy. A neighbouring peak around absorber no. eight is produced by the SOL asymmetry, followed by a decay to 0.2 mW in detector no. twelve at the edge of the array. The VBCr camera shows a smooth, parabolic core emissivity down to 1 mW and a conclusive, comparable to the inside peak in the left camera structure at 2.2 mW in channel no. four. Before decreasing to 1 mW at the edge in no. null, a small feature in absorber no. one interrupts this trend at 1.9 mW . The horizontal camera measures a maximum 0.9 mW in detector no. 26 on the lower side of the array and only 0.4 mW opposite in channel no. ten, with a shallow local minimum in the core at a similar intens-

Chapter 5. Two-dimensional radiation inversion

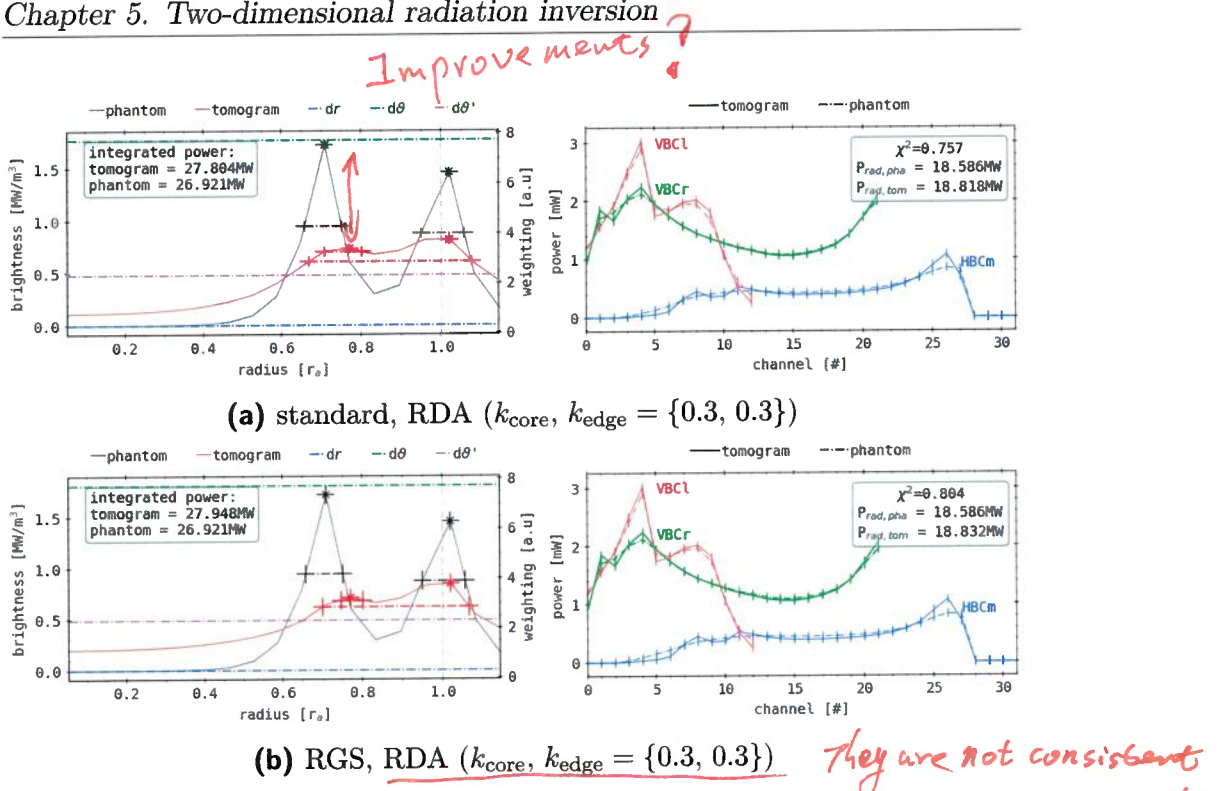


Figure 5.29.: (a), (b) Corresponding analysis for the results shown in figure 5.28, using the noted below anisotropy parameters for the corresponding tomographic reconstruction methods. The results are presented in the same way as in figure 5.19.

ity. While on the lower, right side of the camera the measured brightness drops sharply, on left towards the top a smooth decay until absorber no. two is found. Integration of the measurements yields a total camera observed radiation power of $P_{\text{rad,phan}} = 18.586\text{ MW}$, which is also higher than for any of the previous phantom images, yet not in a corresponding level to the elevated $P_{\text{rad,2D}}$.

In figure 5.29:(a), the resulting tomograms poloidally averaged radial profile shows brightness inside the core of $>0.12\text{ MW/m}^3$, increasing in a shallow parabola up until the first localisation in $0.72r_a$ of 0.8 MW/m^3 with a small FWHM of $0.15r_a$. After a minor valley, the second, global maximum of 0.8 MW/m^3 in $1.05r_a$ is more pronounced, though of similar width and shape, which is succeeded towards the edge by a steady decay to 0.4 MW/m^3 . Integrating the two-dimensional radiation distribution of the tomogram finds

5.3. Phantom Radiation Profiles

a total power of 27.804 MW, about 3.3 % larger than found in the phantom. Similarly, extrapolation of the forward calculated detector signals yields $P_{\text{rad}} = 18.818 \text{ MW}$, which is also 1.2 % larger than from the corresponding phantoms profiles. The prior are, overall, in positions of local extremes more pronounced and feature larger gradients. However, except for channel no. 26 of the HBCm, they remain within the individual error bars and therefore confidence interval. Around the latter, the horizontal camera produces a sharp peak for this distribution, while two smaller, separated structures are found around detector no. ten that are slightly above and their in-between minima below the phantoms lines. These generally only deviate $\pm 0.05\text{--}0.1 \text{ MW/m}^3$ from the respective phantom forward signals. Similar features appear in the tomograms profile of the VBCr between detector no. one and four. The respective fitness factor is calculated as $\chi^2 = 0.757 \text{ a. u.}$.

The results of the relative gradient smoothing method in figure 5.26:(b) show a comparable image in their radial profile p_r , showing a brightness of $>0.2 \text{ MW/m}^3$ in the core which increases similarly towards the first peak in $0.75r_a$ of 0.75 MW/m^3 . This localisation is particularly narrow at a FWHM of $0.075r_a$. A following local minimum is barely noticeable and blends seamlessly into the outside global maximum in $1.02r_a$ of 0.9 MW/m^3 with a $0.2r_a$ width. Summation of the respective two-dimensional distribution produces $P_{\text{rad},2D} = 27.948 \text{ MW/m}^3$, which is 3.8 % higher than in the phantom or 0.5 % than for the previous reconstruction. Correspondingly, the forward integrated absorber signals also show sharper local extremes and additional, smaller peaks in the same, aforementioned locations. They also remain, besides channel no. 26 of the HBCm, within the confidence interval of the individual phantom profile results and only show deviations in the range of $\pm 0.05\text{--}0.1 \text{ MW/m}^3$. Those minute differences are also expressed in the changes in $P_{\text{rad}} = 18.832 \text{ MW/m}^3$, which is 1.3 % larger than for the artificial forward results. Although the fitness is noticeably increased to $\chi^2 = 0.804 \text{ a. u.}$, a 6.2 % improvement compared to the application of just an RDA weighting. Comparing the application of standalone RDA and combined RGS and RDA regularisation weighting optimisations with the MFR tomography for the same phantom radiation profile and set of $k_{\text{ani}} = \{0.3, 0.3\}$ has produced only minor or almost negligible differences in the one-dimensional evaluations of radial and forward calculated profiles, or even integrated values of P_{rad} and $P_{\text{rad},2D}$. Deviations among those characteristic between the two sets of results are, on the one hand within the respective confidence intervals

of said profiles, and on the other of an order of magnitude that was previously observed by altering k_{ani} coefficients for a constant artificial radiation image. Like before, the cumulative trend of the changes from (a):RDA to (b):RGS+RDA is inconclusive at best due to the contradicting evidence presented by the singular power values, as well as the radial and camera profile and corresponding fitness factors. While the priors matching regresses, the latters congruence and quality improves noticeably. Therefore, judging just from the circumstances presented in figure 5.29, a combined RGS regularisation and RDA weighting tomography approach does not yield a significant advantage over just a standard MFR with RDA that would justify unrestricted utilisation instead of the latter. However, the two-dimensional distributions in figure 5.28 show a different picture which, subjectively, does favour the RDS+RDA with respect to the development and composition of the characteristic features of the phantom. Although the corresponding MSD profile does yield higher error values for the latter, strong separation between the core and SOL structures, as well as short, poloidal decay lengths are far more prominent here. Furthermore, the conclusive total brightness and its maximum also match the input data better, though one should keep in mind that none of the reconstructions is able to adequately invert the more intense anisotropy in the core and instead shift its feature to the separatrix. A possible drawback from this favoured stronger localisation of emissivity in the tomogram is the loss of less intense structures in close radial or poloidal proximity to said extremes and smoother profiles of larger connection lengths, i.e. the remainder of the bright rings opposite of the asymmetry.

This concludes the comparison between standard RDA weighting and combined RGS+RDA MFR tomography. A more elaborate and detailed exploration of said topic with more examples will not be performed here, nor be of subject to this work. Zhang et al.[106, 168] have already done such an extensive analysis. The above examinations only serve to further verify the standalone radially dependent anisotropy regularisation, which has been done so.



5.3. Phantom Radiation Profiles

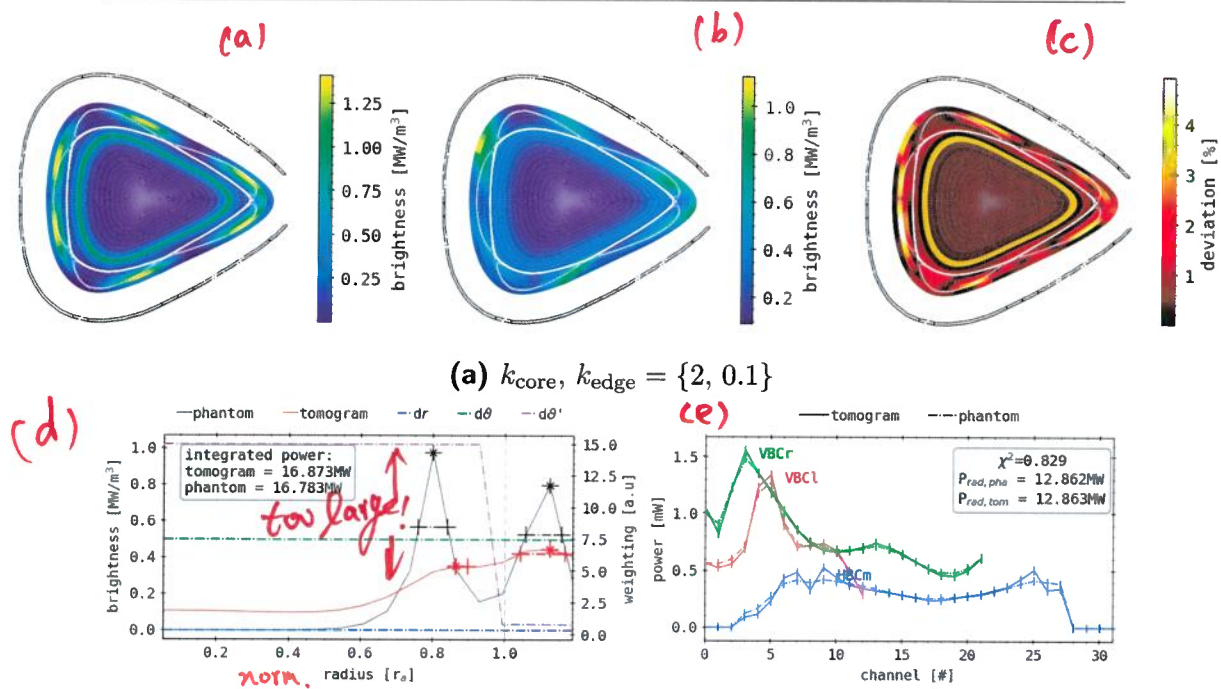


Figure 5.30.: Phantom radiation distribution reconstruction, mimicking a bright plasma core with six intensity maxima around the five islands of the magnetic standard configuration. The RDA coefficients that have been used support the accurate reconstruction of the designed profiles in the tomographic algorithm. (a, top) Phantom, tomogram and relative deviance, similar to figure 5.18. (down) Radial (left) and chordal (right) profile analysis, similar to figure 5.19.

5.3.3. Experimentally Motivated Anisotropic Phantoms

In the following paragraphs we will explore more complex, experimentally motivated and therefore particularly challenging to reconstruct phantom radiation profiles. The focus here will be specifically localised anisotropic distributions that also feature additional extremes in positions and number of the magnetic island and intersecting X-point structure. With the knowledge and experience gained from the previous analysis, this should prepare for and build the foundation necessary to adequately and confidently reconstructive actual experimental data later on. **photons 5.3.0**

The first of this set of artificial emissivity profiles in figure 5.19 is a superposition of a symmetrical bright ring in the core at $0.7r_a$, like before, and a

r~

suggestions:

- Prod for total radiated power
- Prod for local emissivity

Chapter 5. Two-dimensional radiation inversion

distribution of six singular, localised structures around the triangular plane in the SOL, close to the magnetic islands in $1.1r_a$. This outside anisotropy is constructed up-down symmetrically, i.e. the discrete representation of the emissivity yields $P_{\text{rad}}^{(i,j)} = P_{\text{rad}}^{(i,n_\vartheta-j)}$, where n_ϑ is the number of poloidal bins and i and j the radial and poloidal indices for pixel $p^{(i,j)}$. One should note that this is trivial for n_ϑ even, however for an odd number of bins we construct the emissivity so that in pixel $p^{(i,m)}$ for $m = (n_\vartheta - 1)/2 + 1$ the absolute value is the average of the neighbouring cells, so essentially $P_{\text{rad}}^{(i,m)} = P_{\text{rad}}^{(i,m-1)}$. Using

$$m = \begin{cases} (n_\vartheta - 1)/2 + 1 & \text{for } n_\vartheta \text{ odd;} \\ n_\vartheta/2 & \text{for } n_\vartheta \text{ even} \end{cases},$$
$$\text{owidetilde}P_r^{(i,j)}(P, r_0, \sigma) = \frac{P}{2\pi\sigma^2} \exp\left(-\frac{1}{2}\left(\frac{r^{(i)} - r_0}{\sigma}\right)^2\right),$$

the up-down split phantom emissivity can therefore be written in two parts as

$$\begin{aligned} j \leq m : \quad P_{\text{phan}}^{(i,j)} &= \tilde{P}_r^{(i,j)}(\hat{P}, 0.7r_a, \sigma_r) + \frac{3}{2}\tilde{P}_r^{(i,j)}(\hat{P}, 1.1r_a, \sigma_r) \times \\ &\quad \frac{1}{2\pi\sigma_\vartheta^2} \exp\left(-\frac{1}{2}\left(\frac{1 + \sin(\vartheta^{(j)}\delta_\vartheta + \vartheta_0)}{2}\right)^2\right). \\ j > m : \quad P_{\text{phan}}^{(i,j)} &= P_{\text{phan}}^{(i,m-j)} \end{aligned} \tag{5.20}$$

Here, the radial width is designed as before, i.e. $\sigma_r = 0.25r_a$ while the poloidal dimension of the SOL anisotropy is set to $\sigma_\vartheta = 0.2617 \text{ rad}$ or $\pi/12$. The amplitude of the phantom is set to $P = 1 \text{ MW/m}^3$, which directly corresponds to the brightness of the core structure. Hence, outside the separatrix, the individual island-like spots have a maximum of 150% of the prior intensity. Due to the already mentioned difficulties of mapping continuous emissivity distributions to such relatively large and coarse, discrete pixel grid, the actual global maximum brightness in the phantom yields 1.41 MW/m^3 . Two new parameters δ_ϑ and ϑ_0 are introduced, which will also be featured in the following artificial distributions, as the *poloidal frequency of the anisotropies*, i.e. the spatial periodicity of the structures (in the SOL) and an angular offset. Here, for $j \leq m$ or $\vartheta^{(j)} \leq \pi$ - the definition of the poloidal

The averaged pixel

With up-down symmetry.

bin number and dimension is changed from before to have its origin towards the center of the HBCm pinhole - one can find three distinguishable bright spots outside the LCFS. This is equal to $\sigma_\vartheta = 0.9549 \text{ rad}^{-1}$, while the first local maximum is rotated about one fourth of this period away from $\vartheta = 0$ and therefore $\vartheta_0 \neq 0$. On the opposite, inboard side at $j = m$ or $\vartheta^{(j)} = \pi$, a small minimum separates the two structures that are mirrored around a hypothetical, horizontal median through the HBCm aperture and magnetic axis. Both are aligned along the outside edge of the corresponding island and spread into the neighbouring X-points. The same is true for the two remaining sets of up-down symmetric bright spots with respect to their closest magnetic island.

A first reconstruction of the above ~~artificial~~ radiation distribution for $k_{\text{ani}} = \{2, 0.1\}$ can be found in the center of figure 5.30 as per usual. The anisotropic weighting profile is again given by Θ_{N_T} for $N_T = 17$, a simple step from k_{core} to k_{edge} (see section 5.3.1), and is designed to emphasize smooth structures of large angular width in the core for $r < r_a$ and anisotropic brightness profiles with smaller poloidal expansion. Immediately standing out is the now distinct asymmetry around the core between the individual mirrored, artificial peaks. Particularly the top inboard bright spot is far more intense with its global maximum of 1.15 MW/m^3 , while also being shifted closer to the corresponding X-point around $1.25r_a$, very close to the domain boundary. The respective lower structure is significantly weaker in its brightness with $\sim 0.6 \text{ MW/m}^3$ and is reconstructed even closer to the lower separatrix intersection than the upper. Neighboring to those, towards the pinhole of the HBCm, the up-down discrepancy is reversed so that the lower structure shows 0.9 MW/m^3 and the upper just around 0.6 MW/m^3 . However, their individual positions here are generally in very good agreement with their input counterparts, though with a lesser poloidal width and slightly increased radial expansion. In-between the previous two sets, no noticeable emissivity can be found in and outside the LCFS. On the outboard side, closest to the horizontal camera aperture, the upper bright spot is reconstructed similarly in agreement with the phantom at a reduced intensity of 0.9 MW/m^3 and larger radial expansion. Its mirrored feature on the lower side though is shifted towards the HBCm and domain boundary with a smaller brightness of 0.8 MW/m^3 and extends poloidally into the corresponding magnetic island. In the core, a very weak, smooth emissivity distribution can be noticed with just 0.45 MW/m^3 that extends from $0.65r_a - 0.95r_a$ and has a very small

Shorten it!
The top tomogra
show clear differ
Structure ...

gap along the separatrix to the enclosing bright features.

The MSD profile on the right shows complex structures around the LCFS and within the magnetic islands of 3–4.9 % that are distinctly pronounced and largely coincide with the individual localisations of the respective bright spots in the SOL. Furthermore, minor variability is found in-between said features with <2.5 %. Particularly the reconstructed, at the domain boundary localised emissivity yields additional variance of 3–3.5 % in that location. Towards the LCFS, the radially wide and blurred tomographic inversion of the core ring produces errors of $\leq 1.8 \%$ at the separatrix and a constant 3.5 % at $0.7r_a$, the location in the input profile.

The bottom two images in figure 5.30 present the radial and camera forward integrated chordal brightness profiles, including the regularisation weights across the radius as per usual. In the plot on the left, the phantom yields two pronounced, sharp maxima in $0.8r_a$ and $1.12r_a$ of 1.0 MW/m^3 and 0.8 MW/m^3 in the poloidally averaged radial profile, respectively. In-between the prior global maximum and outside peak with individual FWHM of $0.15r_a$ and $0.2r_a$, there is a distinct local minimum of 0.15 MW/m^3 in $0.92r_a$. No significant emissivity is found in the core until $0.55r_a$. The reconstructed radiation profile produces $\sim 0.1 \text{ MW/m}^3$ until $0.6r_a$, after which a small plateau with a shallow slope follows to 0.35 MW/m^3 up to $0.9r_a$. A conclusive peak in $1.15r_a$ at 0.45 MW/m^3 with a width of $0.1r_a$ extends until the domain boundary. The corresponding radial and poloidal regularisation weight profiles dr and $d\vartheta$ are as before, while the step in the modified anisotropic $d\vartheta'$ is now located in $0.975r_a$, right in-between the input profile extremes, from 15 a. u. down to 0.75 a. u. Integration of the two-dimensional phantom and tomogram images yield $P_{\text{rad},2D} = 16.783 \text{ MW}$ and 16.873 MW respectively, which corresponds to a 0.5 % deviation.

shorten the text!

On the right, the forward integrated ~~camera~~ *chord-brightness* profiles are shown. Extrapolation using said pseudo-measurements finds very strong agreement between the two with $P_{\text{rad}} = 12.862 \text{ MW}$ and 12.863 MW from the phantom and tomogram. However, the fitness factor $\chi^2 = 0.829$ a. u., when compared to the previous phantom image tomographies and their evaluation, is not particularly high yet within the range of adequate reconstructions. Forward integration of the artificial radiation profile shows a generally smooth line for the HBCm, where the core is slightly hollowed between channel no. 12 and 23 down to 0.25 mW. From absorber no. two to seven, i.e. from the upper side of the triangular plane, the perceived brightness increases steadily

5.3. Phantom Radiation Profiles

to 0.37 mW, while on the other side between detector no. 24 and 27 the power is nearly constant around 0.4 mW, after which a sharp decline to zero follows. The left vertical camera finds a very dominant peak in channel no. four and five of 1.2–1.25 mW that similarly drops quickly on both sides. Towards the core and detector no. zero, the profile increases minutely again, whereas towards the SOL and edge a small plateau between no. seven and ten around 0.8 mW is concluded by decay to 0.3 mW. Finally, the VBCr plot shows the global maximum in absorber no. four with 1.55 mW with linear declines on both sides. At the outboard side, from a small valley of 0.8 mW in detector no. one a step up to 1 mW concludes the right-hand sight of the camera fan. Towards the core and VBCl, the drop turns into a slight positive slope in absorber no. nine and minor peak of 0.7 mW in no. 13. A subsequent smaller decay to a secondary minimum of 0.45 mW in no. 19 is terminated by a small increment.

Overall, the tomograms forward calculated profiles are very similar in shape and character, while remaining within the indicated error bar confidence interval. However, in locations of extremes in the vertical camera plots it is more pronounced and exceeds or falls below the latter range by ≤ 0.1 mW. In the HBCm profile, additional features can be found on both sides of the core between channel no. five and ten, as well as no. 24 and 27. Towards the upper part of the SOL and separatrix, two small peaks in no. seven and nine of up to 0.5 mW, ca. 0.15 mW over the phantom baseline are separated by a lower minimum. On the other side, just one local maximum in no. 25 at 0.5 mW is followed by a sharper drop.

The performed and examined reconstruction in figure 5.30 using $k_{\text{ani}} = \{2, 0.1\}$ is able to find the specifically designed poloidal anisotropies with a sharp outline and close to their original position in the input phantom, while also reproducing a smooth, less bright structure in the core. However, this does not come without the introduction of a significant asymmetry in the island-like localisations around the separatrix, particularly where the LOS density and sensitivity is increased - this pattern has already been discussed before -, i.e. in front the HBCm and VBCl pinhole and the largest intersection of their LOS cones. Respective to the radial profile and its discrepancy with the artificial input, a strong radial broadening of the inside emissivity is highlighted here, though the SOL features yield only slightly higher radiation power on average. The outstanding congruence between the individual integrated and extrapolated power values $P_{\text{rad/2D}}$ underlines the

overall quality of the tomogram, which is supported by the good agreement of the forward calculated camera measurements and their corresponding fitness factor χ^2 . The latter describes an adequate reconstruction, however of no exceptional grade if estimated by solely with value. Again, like for all previous phantom MFR tomographies, a large variance in the singular power numbers when integrating from two- or one-dimensional profiles is found. The difference between the *actual* total power from the phantom and tomographic radiation profile and the absorber signals is greatly increased relatively and in absolute terms when compared to reconstructions of similar fitness, i.e. figure 5.27, though equally reduced or improved next to figure 5.29 and alike.

This MFR of a more complex, experimentally motivated phantom brightness profile using the same tools and gained knowledge from previous tomographies as a first attempt has proven successful. Given the *best-guess* anisotropic weighting profile and parameter combination, the achieved results adequately present both quantitative and qualitative features of the artificial input image. This is another important step towards the reconstruction of actual experimental data. Furthermore, in the following segment varying sets of k_{ani} for the same phantom and MFR method will be explored to solidify and expand the experience for this set of tools towards such data.

why?
See the differences
in Fig. 5.30
between phantom and tomogram
and also the 1D radiation profile.

~~smoothing~~

Anisotropic Weighting Parameter Variation

✓ OK

In figure 5.31, the same artificial emissivity distribution as in figure 5.30 is reconstructed using three drastically different, yet characteristically similar k_{ani} profiles. The goal is, in principle, to evaluate the impact of varying weighting factor ratios and orders of magnitude for such a given phantom that features anisotropic as well as smooth and uniform structures. A starting point is the already established benchmark for a set of $k_{\text{core}} = 2 \text{ a. u.}$ and $k_{\text{edge}} = 0.1 \text{ a. u.}$ from before. Hence, this parameter set is extended by (a) $k_{\text{ani}} = \{2, 0.3\}$, (b) $\{20, 0.3\}$ and (c) $\{2, 0.6\}$. For all of these, the regularisation weights configuration is the same as before, i.e. RDA method with a shape of Θ_{N_T} for $N_T = 17$. Furthermore, though in contrast, an extended examination is not performed here and the presentation of one-dimensional profiles as well as singular power values or fitness factors omitted. The focus is, after having already proven the generally applicability of this approach, to classify the new parametric weights with regards to their capability to

5.3. Phantom Radiation Profiles

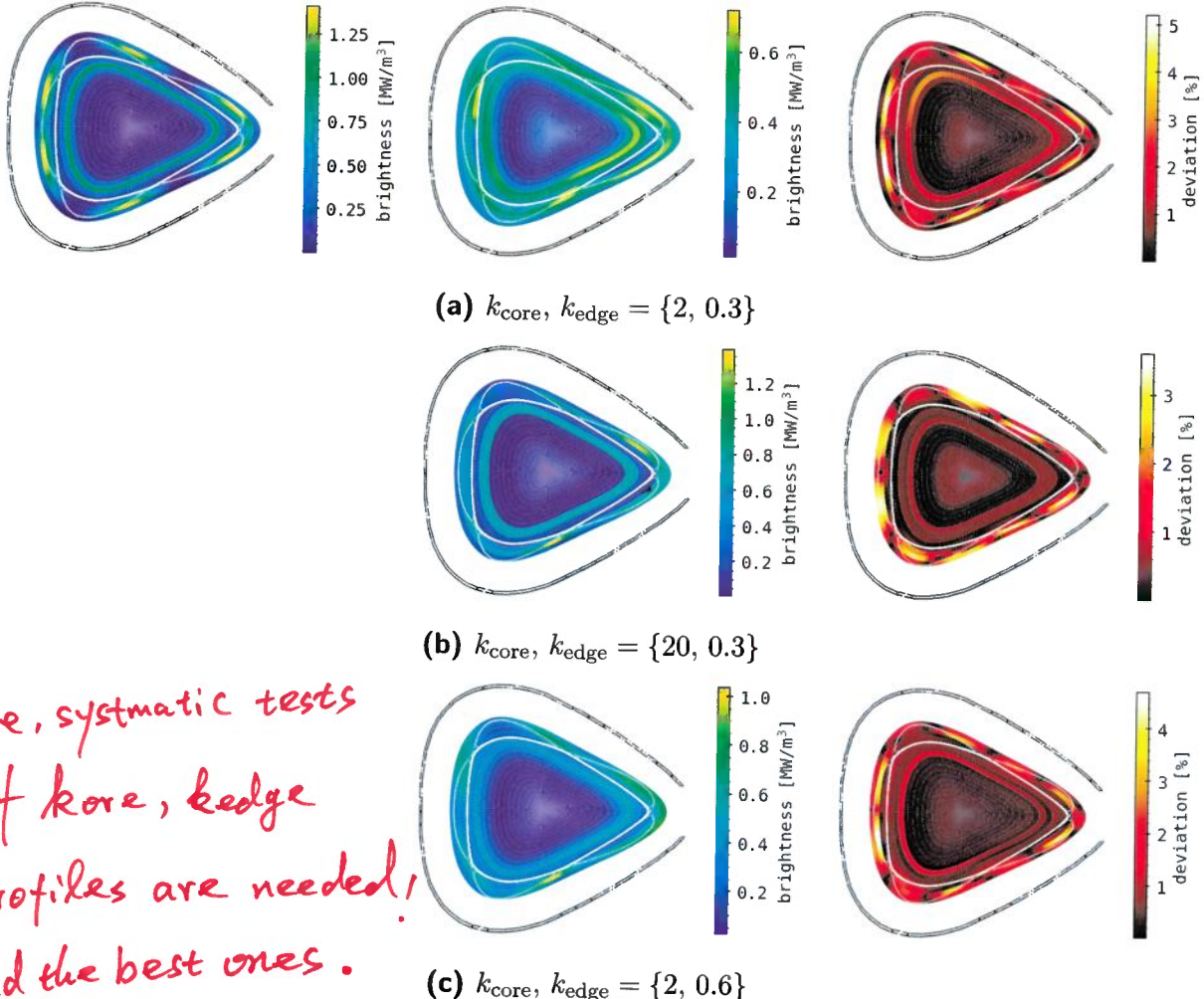


Figure 5.31.: MFR tomography like in figure 5.30 where the RDA coefficients have been varied and are noted below. **(a, top)** Phantom, tomo-gram and relative deviance, similar to figure 5.18. **(b, c)** Only the reconstruction and its respective error to the phantom image like above.

qualitatively reproduce the characteristic features in the artificial profile. In the top row of figure 5.31, the input emissivity distribution and corresponding reconstruction and MSD profile for the anisotropy coefficient set (a) are shown. This combination emphasizes comparatively three times larger

~~connection lengths in the SOL than the prior benchmark.~~ One can easily establish that the maximum brightness is significantly decreased here with 0.75 MW/m^3 . This intensity however can be found in multiple places around the core: at the outer edge of the upper and lower outboard magnetic island, in the lower midplane X-point and inside the middle inboard island, towards the upper neighbouring separatrix intersection. In the SOL, the space in-between those localisation is relatively bright also at $>0.35 \text{ MW/m}^3$ and establishes a smooth and almost continuous ring that partially expands until the domain boundary. Particularly the first mentioned bright spot is accompanied by an elevated emissivity of $\sim 0.6 \text{ MW/m}^3$ inside the island structure. Inside the LCFS, a weakly detached from the outside, similarly wider and nearly symmetrical hollow ring can be found outwards from $0.7r_a$. It is also of about the same intensity as the SOL profile, while its local maximum closer to the HBCm pinhole is around 0.61 MW/m^3 . A corresponding MSD distribution on the right yields error values of up to 5.2 % in the locations of the input bright spots in the SOL. Along the island chain an average discrepancy of about 2.5 % is noted, though the input core ring at $0.7r_a$ leads to an also separated ring of increased variation of 2–3.4 %, where the profile is inverted to that in the tomogram.

The second row in figure 5.31 for parameter set **(b)** $k_{\text{ani}} = \{20, 0.3\}$ shows its respective MFR tomogram and MSD error distribution. This weighting combination again prefers longer connection length characteristics in the SOL and now amplifies emission from the core compared to the benchmark and prior reconstruction. Evolution of the ratio between k_{core} and k_{edge} from 20:1 to 6.67:1 to 66.67:1 underlines the change in focus of the regularisation coefficients towards concentration of radiation in the edge and then inside the LCFS. Hence, the tomogram finds its global maximum of 1.4 MW/m^3 in only two, more concentrated localisations at the inside of the upper outboard and edge of the inboard lower magnetic island towards the X-point. Minor variations can be found along the otherwise nearly continuous emissivity along the $1.1r_a$ radius with an intensity of $0.9\text{--}0.95 \text{ MW/m}^3$. At the tip of the triangular plane, the brightness expands outward until the domain boundary. A void gap separates the SOL from the sharply differentiated core profile at $0.7r_a$ with a smooth emissivity of 0.8 MW/m^3 . Correspondingly, the maximum error value is reduced to the overall higher radiation power in the tomogram at the respective radii. Coincidentally, outside the separatrix, the missing phantom characteristics are represented by 3.2–3.6 %

5.3. Phantom Radiation Profiles

deviation in and around their individual location. Like for the above image, the area in-between also shows elevated levels of discrepancy $\sim 1.6\%$. Inside the LCFS, only minor errors $\leq 1\%$ can be found around $0.7r_a$. At the very center for $< 0.3r_a$, negligible variance of $< 0.6\%$ encapsulate the magnetic axis.

Finally, the last line of plots in figure 5.31 presents the reconstruction and MSD for $k_{\text{ani}} = \{2, 0.6\}$, which now yields a core to SOL ratio of 3.33:1. The focus now is changed again to smoother, longer connection length characteristics in the SOL and less emphasis on a radiation majority in the core, which is underlined by the singular maximum outside the separatrix and secondary minor localisations. Sharply separated at the lower midplane X-point from the rest of the edge profile, an emissivity of 1.05 MW/m^3 contrasts the otherwise comparatively even and less intense, larger structures around the LCFS. Closer to the HBCm pinhole and opposite the global maximum, the brightness is slightly elevated around 0.85 MW/m^3 . Minor, almost negligible variations of 0.7 MW/m^3 also show on the inboard side near the respective X-points. They can be noticed at and close to the separatrix intersections around the triangular plane. The area in-between the prior features and ring at the core in $\sim 0.7r_a$ are at 0.55 MW/m^3 , while the latter is widened and fully symmetric. The final, corresponding MSD next to this tomogram yields increased error values of $3.5\text{--}4.6\%$ in locations of the phantoms input SOL characteristics and particularly the inboard lower magnetic island, where the global maximum of 4.7% is found. Due to the smoother and widened emissivity in the area surrounding those and beyond the separatrix, similar structures of $\sim 1.6\%$ deviation appear in the profile here. In $0.7r_a$, a distinct ring of increased discrepancy with a minor asymmetry closer to the inboard side of $1.8\text{--}2\%$.

Of the examined MFR tomographies in figure 5.31:(a)-(c), none exceeds the subjective quality that has been achieved in figure 5.30 by $k_{\text{ani}} = \{2, 0.1\}$. Irrespective of the quantitative agreement between artificial and reconstructed radiation distribution, the latter yields a significantly better distinction of SOL localisation, with furthermore largely reduced erroneous emissivity in-between and a continuous profile at the target location inside the LCFS at the same time. However, certain aspects of the input phantom are highlighted more in the other tomograms, i.e. a clearly separated and relatively brighter, symmetrical ring in the core for $k_{\text{core}} = 20 \text{ a. u.}$ or individual, more focused spots on the outside. Though the opposite effect presents when the

$k_{\text{core}} : k_{\text{edge}}$ ratio is shifted away from the previous sets trend, as is shown by the images in the top. Increasing the SOL regularisation weight further yields a lessened maximum intensity and stronger characteristic smoothness in that area, while the separation from the core and its relative brightness is hence more pronounced in the bottom. In conclusion, the tomographic inversion for such a - in the case of experimental data potentially - complex radiation distribution of varying symmetric and anisotropic profiles inside and outside the separatrix is benefited by a set of k_{ani} coefficients with a ratio of 10:1 and higher but no larger than 50:1 depending on the individual focus. Judging from the given tomograms and their RDA weights, an initial, educated guess for a set that adequately suits the reconstruction of smooth emissivities in the core and short connection length features in the SOL can therefore be constructed using $k_{\text{core}} = 2-10 \text{ a. u.}$ and $k_{\text{edge}} = 10^{-2}-0.5 \text{ a. u.}$ for similar profile shapes to section 5.1.1. Trivially, the opposite case is also true for equally inverted profiles.

Artificial Camera Supported MFR Tomography

Remaining still with the superimposed *island-like* phantom radiation distribution from figure 5.30, given the complexity of the image and the challenges its inversion poses, additional tomograms are produced using an extended set of cameras and therefore LOS that incorporate the previously introduced artificial *MIRh* from section 5.2.3. Exploration of said emissivity reconstruction using the vertical mirror array *VBCm* is omitted for the sake of simplicity - due to the position of the new camera and discrepancies in previous tomograms the latter is also expected to be less beneficial in those circumstances.

LOS distribution
of ARTf
is not shown.

Results for a MFR tomography using the supplementary set of fifteen artificial detectors on the inboard side, covering the entire triangular plane are shown in figure 5.32. Regularisation weights and anisotropic coefficient profile $k_{\text{ani}} = \{2, 0.1\}$ are kept the same as in the first case. The new arrays forward calculated signals in (b) are indicated with *ARTf* (pseudonym for *ARTificial*). In (a), the tomogram shows a maximum brightness of 0.94 MW/m^3 around the SOL close to the upper inboard side X-point, at the outside edge of the upper outboard magnetic island and in the lower central X-point. Less bright localisations with $0.65-0.9 \text{ MW/m}^3$ in the remaining positions of the input characteristics can be found in the reconstruction. The